CHALMERS

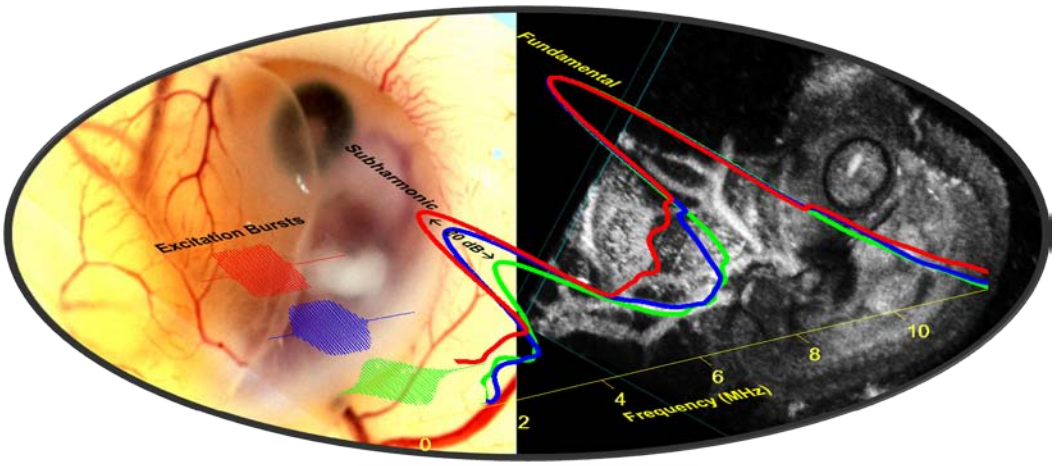

Ultrasound Contrast Agent Detection

Enhanced Subharmonic Imaging Using Self-Demodulation

VERYA DAEICHIN

Department of Signal and System
Division of Biomedical Engineering
CHALMERS UNIVERSITY OF TECHNOLOGY
Göteborg, Sweden, 2011
Report No. EX095/2011

Master of Science Thesis

Ultrasound Contrast Agent Detection Enhanced Subharmonic Imaging Using Self-Demodulation

Verya Daeichin

Department of Signal & Systems
Chalmers University of Technology
2011

Thesis Supervisor:

Prof. Nico de Jong
Biomedical Engineering
Thorax Center
Erasmus MC
Rotterdam, The Netherlands

&

Dr. John G. Bosch
Biomedical Engineering
Thorax Center
Erasmus MC
Rotterdam, The Netherlands

Examiner:

Prof. Yngve Hamnerius
Chalmers University of Technology
Department of Signals and Systems
SE-412 96 Goteborg Sweden

Ultrasound Contrast Agent Detection
Enhanced Subharmonic Imaging Using Self-Demodulation
Verya Daeichin

Abstract

Ultrasound imaging systems are popular imaging tools due to the various features they have. Ultrasound waves used for medical applications have frequencies typically in the MHz range. These ultrasound waves propagate through the human body and are partially reflected from the different tissues. Part of these reflected waves return to the ultrasound system, which receives and processes them into an image. In this way, the size and structure of the tissue can be visualized in echo images, as these images may also reveal possible pathologies or lesions in the tissue. Normally blood is a poor ultrasound scatterer and it remains dark in an echo image. The addition of gas bubbles to the blood pool can greatly increase backscattered ultrasound, and resulted in an enhanced contrast between the surrounding tissue the blood. A gas bubble is unstable due to the surface tension between the gas core and the surrounding liquid. The addition of a coating reduces this surface tension and inhibits the diffusion of the gas. The contrast agent microbubbles owe their function to the high compressibility of the gas core in comparison with surrounding liquid and tissue. This results in a high backscattering of ultrasound. Moreover, the microbubbles can act as resonant systems with resonant frequencies within the same range as medical ultrasound frequencies. Such a resonating microbubble can behave nonlinearly. Microbubbles coating can be conjugated with antibodies and peptides which can be specifically targeted to molecules expressed on endothelial cells lining blood vessels. Targeted imaging with microbubbles may resolve the molecular expression within the vulnerable atherosclerotic plaques. Optimal imaging requires understanding the interaction between targeted microbubbles and high-frequency ultrasound. The Subharmonic (SH) emission from ultrasound contrast agent (UCA) is of interest since this is produced only by the UCA and is free of artifacts produced in harmonic imaging modes. The use of self-demodulation (S-D) signal as a means of microbubble excitation at the SH frequency was studied. The S-D wave is a low-frequency signal produced by nonlinear propagation of an ultrasound wave in the medium and it can be approximated by the second time derivative of the squared envelope of the transmit pulse. Such an stimulation effect was investigated in a single element experiment and the result were compared to the numerical simulation. This study suggests the SH imaging is feasible with low cycle-number transmit burst and low acoustic pressure by optimizing the shape of the transmit pulse. Such a new nonlinear imaging method was implemented in a high frequency pre-clinical ultrasound system and a practical approach for detecting the microbubbles at high frequencies was presented. The results of this thesis will help optimize the parameters for targeted imaging using the nonlinear behavior of the microbubbles.

Keywords: Self demodulation, Subharmonic response, Contrast agent, High frequency ultrasound, nonlinear imaging.

Acknowledgments

Foremost, I would like to thank my parents for their perfect, continues support. Guiding me through the life without trying to change anything inside me is the most beautiful gift I have been given from you.
To Sara: thanks for being very patient and accepting me with the hard time I had during making this work.
To Guillaume, Telli, Ilya and Zeynettin: your contribution has been inestimable.
I would like to thank my supervisors Nico de Joung and Hans Bosch for the very generous support they have lent my endeavors. I would also like to express the deepest gratitude to Antonius van der Steen, who gave me this opportunity to work on this project.
I am grateful to my examiner Yngve Hamnerius for his wonderful guide for this thesis work to be accomplished successfully.
Finally I whole heartedly thank all the members of the biomedical engineering department at Erasmus MC as well as people at Chalmers university of technology for their pleasant company and supports.

Contents

Abbreviations

IVUS intravascular ultrasound

2D and **3D** two and three-dimensional

KZK Khokhlov-Zabolotskaya-Kaznetsov

S-D self-demodulation

UCA ultrasound contrast agent

F fundamental

SH subharmonic

CTR contrast to tissue ratio

UH ultraharmonic

Peer-reviewed paper

1. V. Daeichin, T. Faez, G. Renaud, J.G. Bosch, A.F.W. van der Steen and N. de Jong. Effect of self-demodulation on the Subharmonic response of contrast agent microbubbles. Phys. Med. Biol. In preparation.

Conferences

1. V. Daeichin, T. Faez, G. Renaud, J.G. Bosch, A.F.W. van der Steen and N. de Jong. Subharmonic response enhancement of ultrasound contrast agents using self demodulation. IEEE Ultrason Symp 2011. Oral Presentation.

2. V. Daeichin, T. Faez, G. Renaud, J.G. Bosch, A.F.W. van der Steen and N. de Jong. Stimulating the subharmonic response of ultrasound contrast agents using self demodulation. Leeds microbubble Symposium. Oral Presentation.

3. V. Daeichin, T. Faez, G. Renaud, J.G. Bosch, A.F.W. van der Steen and N. de Jong. Self-demodulation effect on subharmonic response of ultrasound contrast agent. SPIE Medical Imaging Sypmo 2012. Oral Presentatio

1 Introduction

Starting with the question ‘what is clinical ultrasound?’ can be answered in a many different ways. Even though the answers to the people in the field might seem very simple and obvious there are lots of difficulties in explaining details and real physical phenomenon behind the technology. The history of acoustics goes back to thousands of years ago. Such a phenomenon and even the technology has always used by other creatures before being transformed into manmade technology. On the other hand such a long and established history may mislead the scientists, engineers and technology translators consider the field as a solved problem because the basic mathematics have been done more than a century ago. As a result of such a not fully correct description of acoustic, ultrasound in the clinical field is well known for unpredictability, difficulty in scale-up, and a reputation as a ‘black art’ (Mason T J *et al.*, 1992). The consideration of ultrasound safety, especially in the clinical application, must indeed include the involvement of specialists in fields such as clinicians other than acoustic physics. It is crucial to increase the understanding of the complexities in the field, in order to use a predictable and understandable science rather than an unpredictable ‘black art’. Ultrasound in the biomedical world is by necessity a multidisciplinary activity, since successful utilization of the technology needs knowledge of experts in different fields such as chemistry, fluid dynamics, acoustics, transducer, and electronic technology. All these kind of specifications make the field to be very fruitful for discoveries, however it is in turn difficult for correctly understanding, scale-up and exploitation in details.

The application of ultrasound in our today world can be classified into two groups: detection and material processing. These terms in the biomedical world can be translated to the equivalent terms: diagnosis and therapy. In the diagnostic part using ultrasound for scanning of the foetus or other organs is commonplace (Duck F A *et al.*, 1998, Szabo T L, 2004). The most common ultrasound function in diagnostic perhaps is external foetal scanning using ultrasound systems working in frequency range of 3–10MHz. The safety of these applications is regularly and professionally reviewed (Barnett Stanley B *et al.*, 2000), although this subject comes into sight in the popular press very often. Applications of diagnostic ultrasound has not been limited to only foetal scanning and nowadays lots of other anatomical sites are benefiting from ultrasonic scanning for diagnostic purposes. Lots of improvement and innovations have been done on different part of this field. Different probes are developed in a more specialized way for monitoring specific organs or anatomical structure and the exploitation of higher frequencies up to 50 MHz to gain a micrometer size resolution. Ultrasound has not only being used for imaging methods but also other non-imaging diagnostic techniques have been developed for applications such as monitoring bone health and osteoporosis through measurement of sound speed and attenuation (Langton C M *et al.*, 1984, Hosokawa A *et al.*, 1997, Strelitzki *et al.*, 1998, Hughes *et al.*, 1999, Hughes *et al.*, 2003, Njeh *et al.*, 1999, Lin *et al.*, 2001, Lee *et al.*, 2003, Wear, 2005). Using the ultrasound technologies for therapeutic applications in biomedical field vary from lithotripsy (for destructing the kidney stones) (Sass *et al.*, 1991, Chaussy *et al.*, 2002) to surgery (Bailey *et al.*, 2001), physiotherapy and

Sonochemistry (the enhancement of local drug delivery and chemical reactions with the help of ultrasound) characterizes some of the topics facing the use of ultrasound.

1.1. Clinical ultrasound as an imaging modality

Up to now the most common way of using ultrasound for imaging purposes, is the pulse-echo method which is in principal very similar to the methods used in sonar and radars systems. An acoustic wave is transmitted in the medium and the backscattered signals from objects in the medium are processed to provide an image from the medium (Figure 1.1).

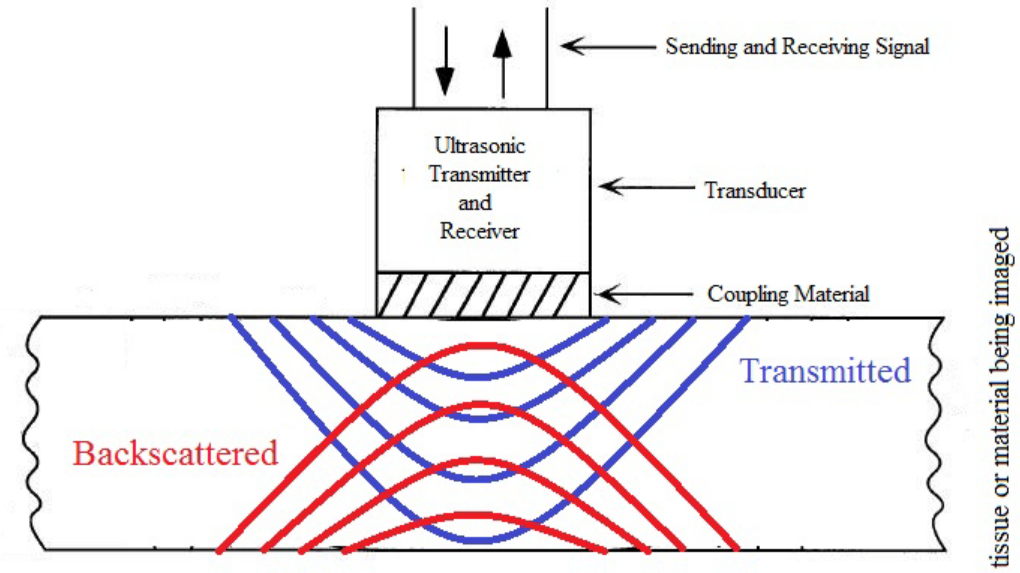

Figure 1.1. Schematic of pulse-echo technique used for ultrasound imaging.

An ultrasound image then is the visible corresponding part of an object which is invisible for human naked eyes. In an ultrasound system the transducer is used both to generate the sound wave and to listen to the echo coming from the tissue. In Figure 1.2 you can see different types of transducers commonly used in clinics. Table 1.1 provides a short description for each of these transducers (CardioVascular Sales, 2011).

Table 1.1. Commonly used ultrasound probes for medical applications (CardioVascular Sales, 2011)

Transducer	Description
AcuNav 8F	Intra-cardiac probe (2-10 MHz)
Aux CW	Transthoracic probe (2 MHz)
V5MS	Shielded TEE Transesophageal probe (3-7 MHz)
V7M	TEE Transesophageal probe (5-10 MHz)
10V4c	Vector linear probe (4-10 MHz)
4V1C	Adult cardiac linear array probe (1-4 MHz)
4C1	Curved linear OB/abdominal probe (1-4 MHz)
6C2	Curved linear OB/abdominal probe (2-6 MHz)
9L4	Linear probe (4-9 MHz)
15L8W	Linear array ultrasound probe (8-15 MHz)
4C1	Curved linear OB/abdominal probe (1-4 MHz)
6L3	Linear array vascular probe (3-6 MHz)
8L5T	T-shaped inter-operative probe (5-8 MHz)
4C1	Curved linear OB/abdominal probe (1-4 MHz)
6C2	Curved linear OB/abdominal probe (2-6 MHz)

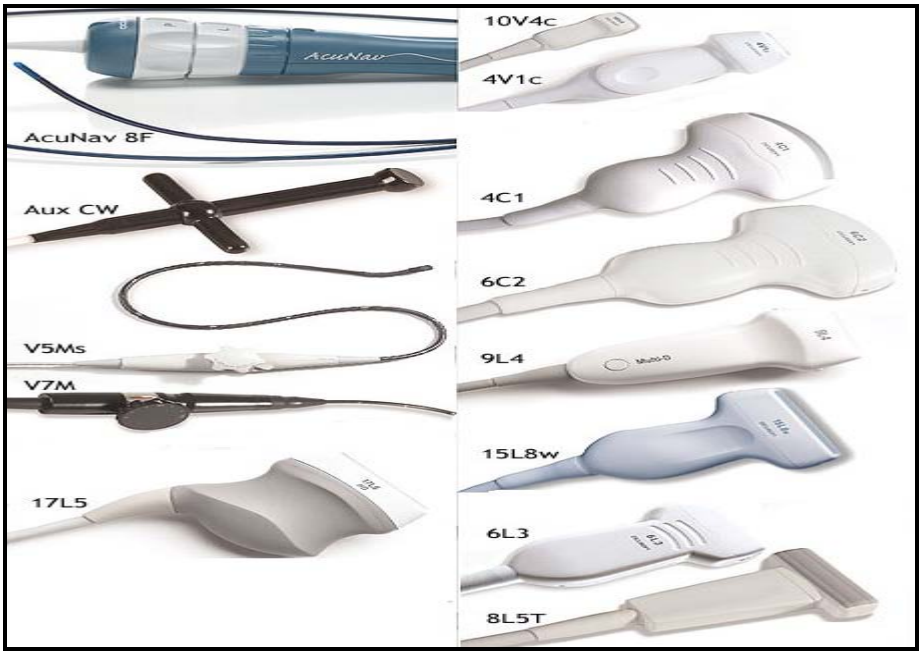

Figure 1.2. Different kinds of transducer used in biomedical field (CardioVascular Sales, 2011)

The received echo by the transducer is processed by the ultrasound system then presented as visible dots which will form the anatomical images on the screen of the system. In such a way, the intensity of each dot in the image shows the strength of the echo from corresponding anatomical point. This method is called gray scale imaging. The exact position of the dots corresponds to the real anatomical structure can be estimated by knowing the direction of the echo pulse as well as the time needed for the wave to reach the target and the echo to come back to the transducer. By knowing the speed of sound in the medium the depth of the structure can be determined in the image. Ultrasound systems use the arrival times of the echoes from the targets in different distances to locate them properly in depth. When one pulse of ultrasound is transmitted into the medium, a series of dots with different intensities are displayed. This line of echo information is called one scan line. Obviously not all of the ultrasound energy is scattered back from the different objects in the medium. There is some of the energy passing through the interfaces and being reflected from the deeper objects. If this process is repeated in different locations, a cross sectional view on the objects in the medium is made. This way of displaying the ultrasound echoes as a an image is called linear image, referring to the linear array transducers used to make such an image. There are also other ways of making the ultrasound images such as sector image and intravascular ultrasound image (IVUS). In sector images the starting point of each line is the same but the angle of each transmitted pulse is slightly changed. In IVUS a small transducer is send into the vessels and the images are made by rotating such a transducer and doing the pull back at the same time which results in having circular image with a view from the center of the vessel. Figure 1.3 shows examples of clinical cross-sectional gray-scale ultrasound images for three different technologies.

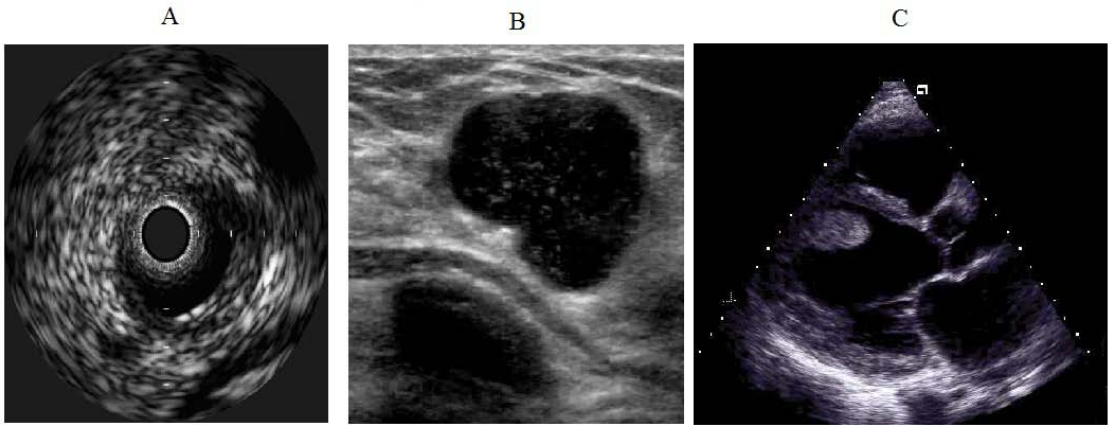

Figure 1.3. Clinical cross-sectional gray-scale ultrasound images for A: IVUS B: Linear image and C: Sector image.

These kind of ultrasound images are called B-mode images. They are all made by sending the ultrasound pulses through the imaged cross-section and converting the echo into the intensity values. The intensity shows the strength of the echo in each point in the image. That is the reason they are called B-scan or B-mode where B is coming from brightness.

Ultrasound technology is not limited to only image the static anatomical structure but also its ability to make the images very fast (up to few thousands images per second) makes it possible to monitor the movements of the different organs.

Other very popular ability of ultrasound systems is Doppler. Echoes produced by moving objects will modify the original frequency of the transmitted pulse. This effect is called Doppler effect. Knowing the physics of this phenomena an ultrasound system can detect the speed of the moving objects.

The introduction of real-time two-dimensional (2-D) imaging which can be called a 3-D where the third dimension is time, different anatomical structures in the body could be monitored in real time noninvasively.

Nevertheless, this is not the end of the way and there are still lots of new applications and technological innovations, being developed. Real time 3-D imaging is an example which offers volumetric information, rather than cross-sectional images. Additionally, using ultrasound contrast agent (UCA) opened a new world for ultrasound applications at the molecular levels. The UCA which is mostly gas bubble in very small size (few micrometers) can be injected into the blood flow to enhance the contrast between the blood and the tissue around. Perfusion imaging of, for example, the myocardium or tumors, is also another common application of using the UCA. These small gas bubbles can also bind to a specific targets in the body to provide meaningful physiological and pathological information using ultrasound. In section 1.7 we will discuss them more in details.

1.2. Linearised Plane Wave Equation

Acoustic waves can propagate through a medium differently. Longitudinal plane wave, shear wave; and torsional wave are the most common ones. However the longitudinal compressional waves are the most familiar types of acoustic wave especially in medical ultrasound. The characteristic of this kind of wave is that particles of the medium through which the wave is propagating, swing in the direction of the wave propagation. A short description of the mathematical derivation of this kind of wave taken from (Shung, 2006) is presented here.

Imagine an elastic cube such as in figure 1.4 the pure force in the z direction can be written using the Newton's second law as:

$$\frac{\partial K_{zz}}{\partial z}+\frac{\partial K_{zy}}{\partial y}+\frac{\partial K_{zx}}{\partial x}=\rho\frac{\partial^2 W}{\partial t^2} \qquad 1.1$$

Which ρ is the mass density of the cube, W is the displacement in the z direction and t is time. The left hand side of the equation shows the final force applied to the cube in the z

direction and the right hand side shows the mass of the cube multiplied by the produced acceleration.

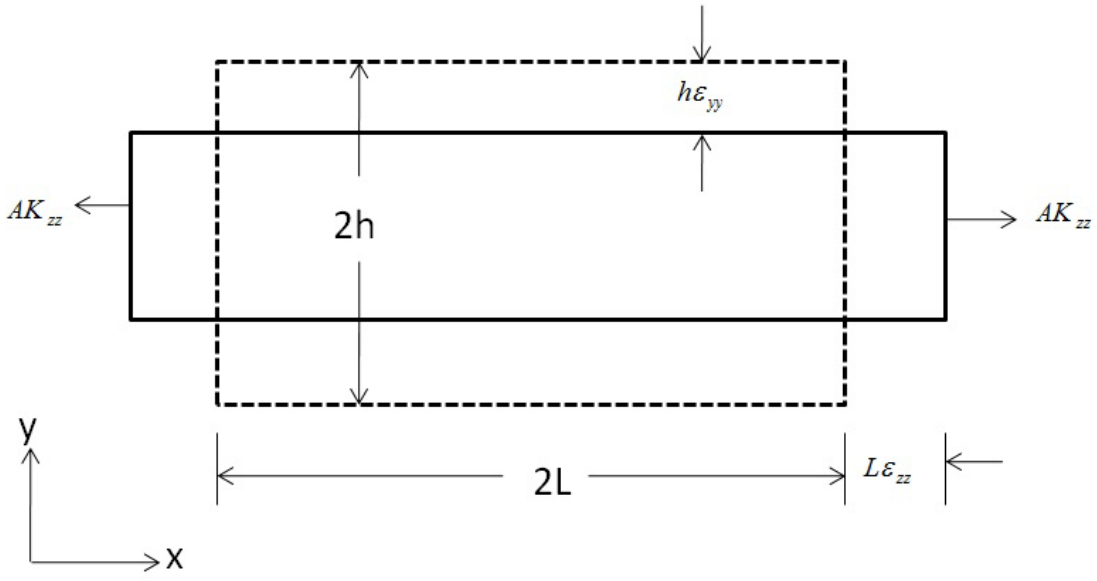

Figure 1.4. Cross-section view of a cube under tension. *2L* , *A* and *2h* are length, cross-sectional width and height of the cube respectively.

When we talk about compressional waves shear stresses can be neglected which means K_{zy} and K_{zx} are zero. Now the equation 1.1 can be rewritten as:

$$\frac{\partial K_{zz}}{\partial z} = \rho \frac{\partial^2 W}{\partial t^2} \qquad 1.2$$

For small displacement the longitudinal stress, K_{zz} can be written as:

$$K_{zz} = (\upsilon + 2\mu)\frac{\partial W}{\partial z} = (\upsilon + 2\mu)\varepsilon_{zz} \qquad 1.3$$

Where υ and μ are Lame constants. The Lame constants depend on the material and its temperature. They are related to the modulus of elasticity (Young's modulus) and Poisson's ratio *v*. Substituting equation 1.3 in 1.2 results in:

$$\frac{\partial^2 W}{\partial z^2} = \frac{\rho}{\upsilon + 2\mu} \frac{\partial^2 W}{\partial t^2} \qquad 1.4$$

Knowing that the speed of sound, *c* is:

$$c = \sqrt{\frac{(\upsilon + 2\mu)}{\rho}} \qquad 1.5$$

We can write the final wave equation as:

$$\frac{\partial^2 W}{\partial z^2} = \frac{1}{c^2} \frac{\partial^2 W}{\partial t^2} \qquad 1.6$$

The general answers of this equation are *f(z + ct)* and *f(z - ct)* where minus sign indicates the wave propagating in the *z* direction and plus sign shows the wave going the opposite direction.

1.3. Nonlinear propagation

The absorption of the ultrasound wave is proportional to the frequency. The higher the frequency the larger the absorption of the acoustic wave will be. Increasing in the amplitude of the pressures used in medical ultrasound systems are unavoidable in order to have higher SNR and larger penetration depth. The ultrasound wave with such a transmit pressure propagates nonlinearly through the medium and the linear representation of the wave equation will not be valid anymore. For the finite amplitude waves (e.g. ultrasound propagating in gases and liquids) the linearised plane wave equation is not covering all the observed phenomenon. Therefore a nonlinear model as well as the important assumptions for having an acceptable linear model will be described in this section.

According to the characterization of the propagation of an acoustic wave in a fluid (gases and liquids) three fundamental statements can be made: Conservation of mass, conservation of momentum and finally an equation which relates the pressure gradient to a longitudinal wave. Considering a one dimensional-wave these three statements can be explained by following equations respectively (Hamilton *et al.*, 1998):

$$\frac{\partial \rho}{\partial t} + \nabla.(\rho v) = 0 \qquad 1.7$$

Where v is the particle velocity. This conservation of mass equation states that the change of the mass per unit volume is equal to the flux across the surface of the volume.

Considering the Euler's equation for an inviscid fluid the equation for conservation of momentum can be written as:

$$v\frac{\partial v}{\partial x}+\frac{\partial v}{\partial t}=-\frac{1}{\rho}\frac{\partial p}{\partial x} \qquad 1.8$$

Which p is the sum of all the steady and unsteady acoustic pressures; and the last equation is:

$$c^2=\frac{\partial p(\rho,S)}{\partial \rho} \qquad 1.9$$

Which relates the speed of sound c, to the equation of state for the medium $p = p(\rho, S)$ where S is the entropy of the system.

Combining all these three equations gives us the formulation of the propagation of acoustic longitudinal wave in a fluid. When the pressure amplitude of the acoustic wave is small, having the approximation that $\rho^{-1} \approx \rho_0^{-1}$ (ρ_0 is the equilibrium density), the speed of sound can be represented by phase speed in the linear limit c_0. In the other world to determine the density, pressure and velocity in this linear limit, the propagation of sound assumed to be adiabatic (evaluated at constant entropy, S). Now we can rewrite the equation 1.9 as following:

$$c_0{}^2\frac{\partial \rho}{\partial t}=\frac{\partial p}{\partial t} \quad , \qquad c_0{}^2\frac{\partial \rho}{\partial x}=\frac{\partial p}{\partial x} \qquad 1.10$$

In linear acoustic an assumption is made that $|v(\partial v/\partial x)| \langle\langle |\partial v/\partial t|$ when calculating $(\partial p/\partial x)/\rho_0$ using the Euler's equation in 1.8. Assume that $P = g(t \pm x/c_0)$ and $v = f(t \pm x/c_0)/(\rho_0 c_0)$ are the linear solutions for the acoustic pressure and velocity. Since neglect of the nonlinear term in 1.8 implies that $\partial v/\partial t = -\rho_0^{-1}\partial p/\partial x$, then recalling 1.10 the second ratio can be reduced to

$$\frac{1}{\rho}\frac{\partial \rho}{\partial x}\Big/\frac{\partial v}{\partial x} = \frac{v}{\rho_0 {c_0}^2}\frac{\partial p}{\partial x}\Big/(\pm f'/\rho_0 {c_0}^2)$$

$$= \pm\frac{v}{c_0} \qquad 1.11$$

The linear assumption will be valid when the acoustic Mach Number $(v/c_0)\,f$ is small and the nonlinear term is negligible. As a consequence of finite Mach Number the linear wave equation (1.6) no longer holds. In such a regime the initially transmitted sinusoidal wave for instance will be distorted during the propagation through the medium and it will not remain perfectly sinusoidal. Distortion of the original wave happens because part of the wave which is compressed moves faster than the refraction component as the wave propagates in the medium (equation 1.11). Such distortion in the spectrum of energy shows itself as the 'pumping' of energy from the fundamental frequency up to higher frequencies where the absorption is greater and also lower frequency where attenuation is smaller. The medium ability to absorb the acoustic wave plays an important role in such a distortion: The higher the absorption the faster the attenuation of the transmitted wave will be, which means a lower *mach number* and in turn a lower nonlinear distortion. More mathematical expressions of these nonlinearities will be give when the wave models are introduced in section 1.4.

1.4. Model equation

In the most applications in the biomedical field intense directional sound beams are used more than plane waves. At such high acoustic intensities, and for propagation in the real situations such as in tissues, a suitable model of directional acoustic radiation must consider different parameters such as diffraction, thermo-viscous attenuation and nonlinearity. It is very critical to realize the approximations and assumptions on which the mathematical equations are based, in order to wisely indentify the limitations and area of applicability associated with model equations of nonlinear acoustics. In this chapter the more commonly used model for nonlinear propagation of acoustic wave in homogeneous fluids, KZK (Khokhlov-Zabolotskaya-Kuznetsov) equation, is briefly described. Then such a equation model is used to mathematically express the S-D signal.

1.4.1. KZK Equation

The KZK equation accounts for the combined effects of diffraction, absorption, and nonlinearity in the directional sound beam. Let's assume *z* to be the direction of the propagation for the acoustic wave, and let *(x,y)* be the coordinates perpendicular to the *z*. For the source producing the acoustic wave several assumption are made: The surface of the transducer is defined in the plan *z = 0*, It has a radius *a*, the acoustic signals are transmitted at frequencies which satisfy the relation *ka>>1* where *k* is the wave number.

According to the liner theory for directional acoustic beams there are two different regions so called near field and far field regions. The border of these two different regions is defined as Rayleigh distance (*1/2ka^2*), measured from the surface of the transducer along the axis of propagation. The planar wavefront is considered to be responsible for the near field and the wavefront that are spherical characterize the far field (Hamilton et al., 1998). We are not going into details of derivation of KZK here and those who are interested can look at the book nonlinear acoustic by Hamilton (Hamilton et al., 1998). Having these assumptions the most widely used equation model, KZK equation, for a directional acoustic beam accounting diffraction, absorption and nonlinearity can be written as:

$$\frac{\partial^2 p}{\partial z \partial \tau} = \frac{c}{2}\nabla_{\perp}^{\ 2} p + \frac{\delta}{2c^3}\frac{\partial^3 p}{\partial \tau^3} + \frac{\beta}{2\rho_0 c^3}\frac{\partial^2 p^2}{\partial \tau^2} \qquad 1.12$$

where p is the sound pressure, z is coordinate along the axis of the beam, $\nabla_{\perp}^{\ 2} = \partial^2/\partial x^2 + \partial^2/\partial y^2$ is a Laplacian function in x and y directions which are perpendicular to the direction of the propagation z, $\tau = t - z/c_0$ is the retarded time, and c_0 is the speed of sound in the medium. The first part on the right hand side of the equation stands for diffraction term, the second part accounts for thermo-viscous absorption where δ is the diffusivity of sound and finally the third term accounts for quadratic nonlinearity of the fluid where β determines the nonlinearity of the medium and ρ_0 is the ambient density of the medium. This equation was introduced for the first time by Zabolotskat and Khokhlov (Zabolotskaya E A *et al.*, 1969) without considering the thermo-viscous term and some years later this term was included by Kuznetsov (Kuznetsov V P, 1971). Also in 1980 a later derivation was provided by (Tjotta *et al.*, 1980).

1.4.2. Self demodulation

As it was mentioned when an acoustic wave is propagating through the medium it will be distorted due to the nonlinear propagation. As a result of this distortion leaking of energy to not only higher harmonics but also lower frequencies takes place. This low-frequency signal produced due to nonlinear propagation of the ultrasound burst in the medium is called the S-D wave. The term S-D was used for the first time by Berktay in the 1960s (Berktay, 1965). He could derive a mathematical explanation for the S-D signal under some assumptions: First of all the propagation should not reach the shock regime; the envelope of the carrier wave should varies slowly compare to the center frequency of the transmitted burst; and the absorption length for the center frequency should not go beyond the Rayleigh distance at that frequency. In that way the S-D waveform predicted by Berktay is proportional to the second time derivative of the square envelope of the

transmitted acoustic pulse. This theory was confirmed experimentally for the first time by Moffett et al(Moffett *et al.*, 1971)

Let's look briefly at the mathematical derivation of the S-D signal. Here we assume a piston source for transmitting the directional acoustic beam which has the following transient condition:

$$p(r,0,t) = p_0 f(t) H(a-r), \qquad f(t) = E(t)\sin[\omega_0 t + \phi(t)] \tag{1.13}$$

Where $r^2 = x^2 + y^2$ and *x* and *y* are the directions perpendicular to the direction of the propagation, and the amplitude modulation *E(t)* and phase modulation $\phi(t)$ are changing slowly in respect to the carrier wave $\sin(\omega_0 t)$. The instantaneous angular frequency of the carrier wave is $\Omega(t) = \omega_0 + d\varphi/dt$. If the attenuation coefficient of the medium at the frequency of the carrier wave is large enough, an asymptotic solution can be driven for the axial waveform under the approximation that the exponential attenuation acts locally according to the instantaneous angular frequency ($\Omega(t)$) as below (Averkiou *et al.*, 1993):

$$f(t) = e^{-\alpha(t)z} E(t)\sin[\omega_0 t + \varphi(t)] \tag{1.14}$$

where $\alpha(t) = [\Omega(t)/\omega_0]^2$ accounts for the time dependant attenuation coefficient in thermo viscous fluid. As it was explained earlier the secondary pressure is determined by the square of the primary pressure p_1, therefore it contains high frequency term coming from $E^2(t)\cos[2\omega_0 t + 2\varphi(t)]$ and low frequency term as coming from $E^2(t)$. The high frequency components are not of interest since it is highly attenuated due to the frequency dependant attenuation of the medium and it will be absorbed much quicker than the wave with the low frequency. Ignoring the high frequency term and remembering that the absorption of the nonlinearly generated low frequency components is a weak effect (since $E(t)$ and $\phi(t)$ are changing slowly in time) as well as ignoring the thermo-viscous attenuation term in equation 1.12 ($set \delta = 0$), the secondary pressure, p_2 can be approximated as follow:

$$\frac{\partial p}{\partial z} - \frac{c_0}{2}\int_{-\infty}^{\tau} (\nabla_\perp^2 p_2)\, d\tau = \frac{\beta}{2 p_0 c_0^3}\frac{\partial p^2}{\partial \tau} \tag{1.15}$$

An axial Green function solution for p_2 can be written in time domain as follow (Hamilton et al., 1998):

$$G_{\omega}(0,z|r',z') = \frac{j\omega}{2\pi c_0(z-z')}\exp[-\frac{j\omega r'^2}{2c_0(z-z')}] \qquad 1.16$$

Remembering the time convention $e^{j\omega\tau}$, from Fourier transform theory one can replace the first factor of $j\omega$ in equation 1.16 with the derivation $\partial/\partial\tau$, and the argument of the exponential term with the time delay $-r'^2/2c_0(z-z')$. According to the definition of the Green function and using the Fourier transform, the axial solution for p_2 produced by an arbitrary $p_1(r,z,\tau)$ is:

$$p_2(0,z,\tau) = \frac{\beta}{2\rho_0 c_0^4}\frac{\partial^2}{\partial\tau^2}\int_0^z\int_0^\infty p_1^2\left[r',z',\tau-\frac{r'^2}{2c_0(z-z')}\right]\frac{r'dr'dz'}{z-z'} \qquad 1.17$$

Under some assumptions such as taking z to be large enough that the phase term $r'^2/2c_0(z-z')$ can be ignored, substituting $dz'/(z-z')$ by dz'/z, expanding the upper integration limit on z' to ∞, substituting the secondary pressure term into equation 1.17 , and finally calculating the integrations results in:

$$p_2(0,z,\tau) \approx \frac{\beta p_0^2 a^2}{16\rho_0 c_0^4 z}\frac{d^2}{d\tau^2}\frac{E^2(\tau)}{\alpha(\tau)} \qquad 1.18$$

In order to get the final complete solution $p = p_1 + p_2$ for the axial direction, we should include the thermo-viscous attenuation term in the equation. For that we can start with the linear axial solution of equation 1.12 having a source of equation 1.13 for arbitrary *f(t)* (Froysa *et al.*, 1993):

$$p_1(0,z,\tau) = p_0\left[f(\tau) - f(\tau - a^2/2c_0 z)\right] * D(z,\tau) \qquad 1.19$$

where $D(z,\tau) = (c_0^3/2\pi\delta z)^{1/2}\exp(-c_0^3\tau^2/2\delta z)$ is a thermo-viscous dissipation function (Hamilton et al., 1998) and the "*" means convolution with respect to τ. Assuming that the secondary pressure p_2 is present within relatively compact volume directly in front of the transducer, the following solution for the final axial waveform can be obtained(Averkiou et al., 1993):

$$p(0,z,\tau) = p_0\left[f(\tau) - f(\tau - a^2/2c_0 z) + \frac{\beta p_0^2 a^2}{16\rho_0 c_0^4 z}\frac{d^2}{d\tau^2}\frac{E^2(\tau)}{\alpha(\tau)} \right] * D(z,\tau) \qquad 1.20$$

According to the equation 1.20 the dominant source near the transducer is the primary source while moving away from the transducer surface, associates with more contribution to the secondary source.

One of the very nice examples showing the building up of the S-D signal due to the propagation in a nonlinear medium both theoretically and experimentally is the work done by (Averkiou et al., 1993) (figure 1.5). The acoustic source for that study was a piston transducer of radius *a=6.4 mm* and the center frequency of the carrier wave was *3.5 MHz*. The tone burst propagates through glycerin. The theory is given by equation 1.20 with $E(t) = \exp[-(\omega_0 t/25\pi)^{10}]$, $\phi(t) = 0$, *and* $z_0/(\rho_0 c_0^3/\beta\rho_0\omega_0) = 1.16$.

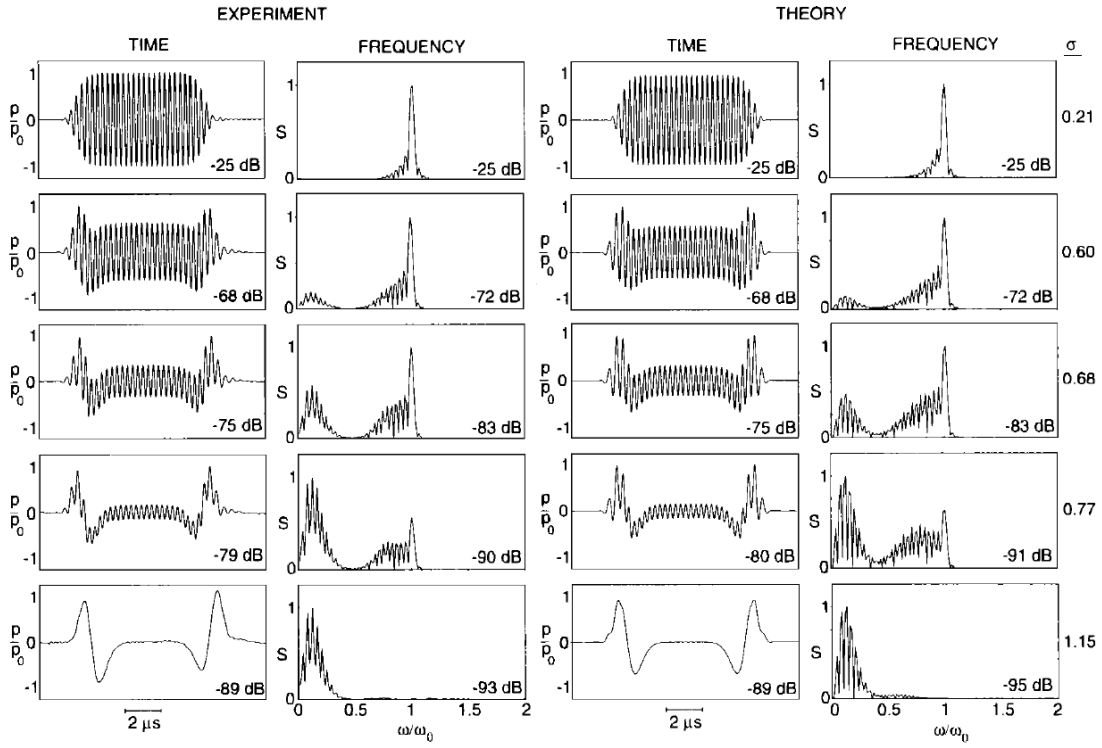

Figure 1.5. Comparison of experiment and theory for the axial propagation of a *3.5MHz* pulse and corresponding frequency spectra illustrates S-D of a pulsed sound beam in glycerin (Averkiou et al., 1993). Decibels indicate level relative to the corresponding source level.

Look how quick the carrier frequency in the tone burst is attenuating and disappearing in comparison with the low frequency, the S-D signal. At $z/z_0 = 1.15$, virtually all that remains from the original tone burst is only the secondary pressure predicted by equation 1.18.

The very important message to keep in mind about the S-D signal is that it is a low frequency physical acoustic wave which is characterized by the envelope of the high frequency carrier pulse, therefore the frequency content of the S-D can be tuned by tuning the shape and the envelope of the transmitted burst.

1.5. Scattering of sound

Imagine a compressional acoustic wave propagating through a medium and facing an object with different acoustical properties on its way. Because of the different acoustical features such as compressibility the change in volume of the object as a reaction to the changing pressure will be different than the surrounding medium. This causes some part of the original wave energy to be scattered.

Let us assume an object with a radius *R* sitting on the way of a linearised longitudinal compression wave expressed by equation 1.6 and an observer at distance r which is larger than the object size, *R* but smaller than the wavelength, λ ($\lambda << r << R$). The right hand side of the equation 1.6 can be ignored because $\partial^2 W/\partial z^2 \propto r^{-2}$ in compare to the left side which is $\partial^2 W/\partial t^2 \propto \lambda^{-2}$ resulting in $\partial^2 W/\partial z^2 = 0$ (Laplace's equation only in *z* direction). Expanding this equation to all directions and defining a velocity potential $v = \nabla\phi$ results in well known Laplace's equation as follow (Leighton, 1994):

$$\Delta\phi = 0 \qquad 1.21$$

Solutions of this equation are harmonic functions. Assuming an incompressible fluid ($\nabla . v = 0$) the velocity potential goes down as the distance increases and so does the gradients. According to this physical phenomenon solutions are on the order of r^{-n} for *n=1, 2,* and may look like:

$$\phi = -\frac{a}{r} + A.\nabla(\frac{1}{r}) + B(\frac{1}{r^2})... \qquad 1.22$$

Therefore the velocity potential is described by the functions such as a, *A, B* … independent of *r* and defined by the boundary conditions. Assume that the volume of the object can change by pressure changes when the sound wave hits the object. Since the fluid is suppose to be incompressible, only changes in the volume $V' = \partial V/\partial t$ will be responsible for the flow rate of the mass m' across a surface. Keeping only the first order approximation for the solution of the Laplace's equation we can write:

$$m' = \oint \rho v dS = 4\pi\rho R^2 \nabla\phi \qquad 1.23$$

And the general solution for a distance large enough compare to the wavelength is a spherical wave:

$$\phi = -\frac{V'(t - r/c)}{4\pi r} \qquad 1.24$$

Recalling the equations for velocity $v = \nabla\phi$ and pressure $p = -\rho\partial\phi/\partial t$ they can be calculated for the scattered wave as below

$$v = \frac{V''(t - r/c)}{4\pi rc}\frac{\vec{r}}{r} \qquad 1.25$$

$$p_s = \frac{\rho V''(t - r/c)}{4\pi rc} \qquad 1.26$$

Where p_s indicates the scattered pressure by the object in the sound field. Now if we assume the object scattering the acoustic energy is spherical as it is for the microbubbles, the scattering pressure can be rewrite as follow:

$$p_{sc} = \frac{\rho R''(t)^3}{4r} = \frac{\rho R(t)}{r}(2R'(t)^2 + R(t)R''(t)) \qquad 1.27$$

It might be useful to go a bit further and define another variable, the scattering cross-section σ, which is defined as a ratio of the intensity scattered by the object to the transmitted energy flux density. Since the intensity of is proportional to the square of the pressure, the scattering cross-section can be written as follow:

$$\sigma = 4\pi r^2 \frac{\overline{P}_{sc}^2}{\overline{P}_{inc}^2} = \frac{\rho^2 \overline{R}^2(t)}{4\pi \overline{P}_{inc}^2}[2\overline{R'}(t)^2 + \overline{R}(t)\overline{R''}(t)]^2 \qquad 1.28$$

in the other word the scattering cross-section shows the amount of power scattered by a spherical object such as a microbubbles.

1.6. Ultrasound contrast agent

Ultrasound contrast agent (UCA) is used to enhance the backscatter signal in clinical ultrasound. They are mainly injected into the blood stream to increase the contrast between blood and anatomical structure such as vessel walls and heart chamber. UCA can be very helpful in applications such as imaging the vasculature structure, clarifying the myocardial border and organ perfusion etc(Quaia, 2007, Dolan *et al.*, 2009). Perhaps the first usage of gas bubbles as a contrast agent for ultrasound was in 1968, when Gramiak et al reported "a cloud of echoes between the undulating margins of the aortic root" after they injected agitated saline in the aortic root (Gramiak *et al.*, 1968). It seemed that the small gas bubbles in the blood pool greatly increased backscattered ultrasound, and resulted in an enhancement of the contrast in the ultrasound images. There were some problems with the very first generation of this contrast agent such as instability and big size of the gas bubbles (Goldberg B B *et al.*, 2001). It was found experimentally that the stability of such gas bubbles can be improved by mixing the patient's blood to the saline (Blomley *et al.*, 2007). The prolongation of the lifetime of the bubbles was due to the surfactant from the blood which formed a coating around the gas core. Not so long time after and in the end of 1980s sufficient stable microbubbles were entered into the medical market.

Instability of a gas bubble is due to the surface tension between the solution around the bubbles and its gas core. When the surface tension is high the bubble tends to decrease in size and the gas escapes into the surrounding liquid. The coating around the gas core reduces this surface tension and therefore slows down the diffusion of the gas.

A new generation of contrast agents consist of small gas bubbles (0.5-10 micron diameter) typically stabilized by an albumin (e.g. Optison, GE Healthcare, Chalfont St Giles, UK), a polymer (e.g. Sonazoid, GE Healthcare, Chalfont St Giles, UK) or have a phospholipids coating (e.g. SonoVue, Bracco, Milan, Italy and Definity, Lantheus Medical Imaging, North Billerica, MA, USA) to reduce dissolution and prevent coalescence. Moreover, these gases are with high molecular weight such as perfluorocarbon, which are also less solvable and have a slower diffusion rate in liquid compared to air (Goldberg B B et al., 2001). A summary of currently available contrast agents is given in Table 1.1 (Emmer, 2009).

Table 1.2. Commercially avalable UCA for clinical applications(Emmer, 2009).

Name	Manufacturer	Gas core	Coating	Year
Echovist	Bayer Schering Pharma AG	Air	Galactose	1991
Albunex	Molecular Biosystems	Air	Human albumin	1994
Levovist	Bayer Schering Pharma AG	Air	Galactose Trace palmitin	1996
Optison	GE Healthcare AS	C3F8	Human albumin	1997
Definity	Lantheus Medical Imaging	C3F8	Phospholipids	2001
SonoVue	Bracco	SF6	Phospholipids	2001
Imagent	Alliance Pharmaceutical Corp	C6F14	Phospholipids	2002
Sonazoid	Amersham Health	C4F10	Lipids	2006

UCA is generally injected intravenous in order to allow the first passage through the pulmonary circulation before going through the systemic circulation which can change the population of the microbubbles. Because of the small size of the microbubbles, they are able to pass through the small capillaries but it seems ones which have sizes more than *5 μm* are removed by the lungs providing a safety standpoint in order to prevent small blood vessel obscuration by the large microbubbles (Bouakaz *et al.*, 2007, Lindner *et al.*, 2002). As it was mentioned before, the gas cores of UCA are mainly from low solubility gases which results in a longer existence in the circulation (several minutes). After rupture of the microbubble the released gas is mainly taken by the lungs and the coating by macrophages(Yanagisawa *et al.*, 2007). Normally the volume of the whole gas taken by the lungs in a clinical application is less than a *1 ml* while in a single breath about *500 ml* will be exhaled. The microbubbles which are used now days as UCA are safe and have high merits compare to other agents used in different image modalities (Blomley et al., 2007, Cosgrove, 2006, Kaul, 2008, Feinstein, 2006, Dolan et al., 2009).

1.6.1. Dynamic of microbubbles interacting with ultrasound waves

Generally speaking, since gas core of the microbubble has higher compressibility than surrounding liquid and tissue, they highly scatter the incident ultrasound wave. Moreover, the microbubbles have also the resonance behavior within the range of medical ultrasound frequencies. When a microbubble resonates, its scattering cross-section becomes in the order of thousands times bigger than when it is not (Pace *et al.*, 1997). If

the amplitude of the incident ultrasound is low, then vibration behavior of microbubble in the ultrasound pressure field can be explained by the harmonic oscillators theory (Leighton, 1994). The stiffness of the microbubbles (oscillator) can be described by the compressibility of the gas core. The oscillations are dampened mainly due to the liquid viscosity and the coating of the microbubbles and other effects such as the radiation of ultrasound and thermal effects. The complete impact of the coating on the microbubble behavior is not fully understood but it has been shown that coating can increase the resonant frequency and lower and broader the resonant peak of the microbubbles (Khismatullin, 2004, van der Meer *et al.*, 2007). A more detailed explanation for this phenomena fallows.

1.6.2. Modified Rayleigh-Plesset equation

Assuming that the fluid is incompressible and remembering that the source of the mass flux, m', is the changes in the volume, V', one can write the following equations for a spherical scatterer with a radius R:

$$m' = \rho V' = \rho 4\pi R^2 R' \qquad 1.29$$

According to the conservation of mass law this mass flux is the same for any bound surfaces such as another spherical boundary with radius r which contains the scatterer *(r>R) (Leighton, 1994)*:

$$m' = \rho V' = \rho 4\pi r^2 r' \qquad 1.30$$

Comparing equations 1.29 and 1.30 results in:

$$r^2 r' = R^2 R' \qquad 1.31$$

This equation is only true under the assumption of incompressible fluid. Close to the border of the microbubble with the surrounding fluid, the spherical symmetry is no longer valid and the fluid molecules will experience a net cohesive force away from the bubble in the radial direction. In order to reduce the increased potential energy in the fluid molecules close to the boundary, the surface area of the cavity tends toward a sphere shape which has the minimum surface area compare to any other geometry. Imagine p_i as the internal pressure in the microbubble and p_L as the pressure at the fluid boundary the outwards overpressure p_σ in the microbubble can be calculated by force of water molecules at the surface as follow (Leighton, 1994):

$$p_i - p_L = p_\sigma = \frac{2\sigma}{R} \qquad 1.32$$

Where σ is the surface tension which has a unit of Newton per meter. Another parameter also coming from the cohesive forces in a fluid around the scatterer is viscosity. Due to viscosity, the vibration of the microbubble results in irreversible diffusion in the momentum. This can be expressed by the stress tensor σ_{ij} which has the pressure as its normal component and a shear component proportional to the orthogonal velocity:

$$\sigma_{ij} = -p\delta_{ij} + \mu\left(\frac{\partial v_i}{\partial x_j} + \frac{\partial v_j}{\partial x_i}\right) \qquad 1.33$$

Which δ_{ij} is the unit tensor (it is one if $i=j$ and zero otherwise), μ is the shear viscosity and p is the pressure inside the microbubble. Looking only at the radial component of the stress tensor gives (Landau LD *et al.*, 1987, Leighton, 1994):

$$\sigma_{rr} = p_r = -p_i + 2\mu\frac{\partial v}{\partial r} \qquad 1.34$$

From equation 1.31 knowing $r' = v$ and having in mind that $p_r = -p_L$ at $r = R$ we can write:

$$p - p_L = 4\mu\frac{R'}{R} \qquad 1.35$$

Looking at the boundary condition, viscosity and surface tension result in a bigger pressure inside the microbubble compare to the pressure in the liquid at the boundary:

$$p_L = p_i - \left(\frac{2\sigma}{R} + \frac{4\mu R'}{R}\right) \qquad 1.36$$

Since the relation of variation of the microbubble volume to its internal pressure is more of an interest the following steps can be derived:

Assuming the compression of the gas to be polytropic process:

$$p_i = p_{i,0}(\frac{V_0}{V})^{\kappa} = p_{i,0}(\frac{R_0}{R})^{3\kappa} \quad 1.37$$

Where R_0 is the equilibrium radius, $p_{i,0}$ is equilibrium pressure inside the bubble and κ is the exponent of the polytropic process. Accepting such a process means that the thermal contribution to the energy dissipation of the bubble is ignored (Plesset M *et al.*, 1977). From equation 1.32 the internal equilibrium pressure can readily be written as:

$$p_{i,0} = p_0 + \frac{2\sigma}{R_0} \quad 1.38$$

Which p_0 indicates the ambient pressure. According to the equation for a polytropic process the pressure in the liquid at the boundary can be expressed as:

$$p_L = (p_0 + \frac{2\sigma}{R_0})(\frac{R_0}{R})^{3\kappa} - \frac{2\sigma}{R} - \frac{4\mu R'}{R} \quad 1.39$$

The difference in the pressure in the bulk liquid p_∞ compare to the pressure at the boundary p_L results in a force which is balanced by the energy coming from the change in the kinetic energy corresponding to bubble vibration. This force can be calculated as follow considering that $F = -\nabla W = -\partial W / \partial R$ (Leighton, 1994):

$$(p_L - p_\infty)4\pi R^2 = \frac{d}{dR}[\frac{1}{2}\rho \int_R^\infty r'^2 4\pi r^2 dr] \quad 1.40$$

Recalling the equation 1.31 and rearranging we get:

$$\frac{(p_L - p_\infty)}{\rho} = RR'' + \frac{3}{2}R'^2 \quad 1.41$$

The Rayleigh-Plesset equation can be obtain by considering the $p_\infty = p_0 + p(t)$ and equation 1.39:

$$RR'' + \frac{3}{2}R'^2 = \frac{1}{\rho}[(p_0 + \frac{2\sigma}{R_0})(\frac{R_0}{R})^{3\kappa} - \frac{2\sigma}{R} - \frac{4\mu R'}{R} - p_0 - p(t)] \quad 1.42$$

Having this equation makes it possible to determine the radius of the bubble as a function of time for a given applied acoustic pressure. Looking deeper in the Rayleigh-Plesset equation one can see that not all the parameters are involved and there are some approximation for simplifications. For example the damping of the sound energy because of the sound radiated by the bubble is not accounted. Here we will introduce a new equation without going through the derivation which contains this damping (Neppiras E, 1980, Lofstedt *et al.*, 1993):

$$RR'' + \frac{3}{2}R'^2 = \frac{1}{\rho}[(p_0 + \frac{2\sigma}{R_0})(\frac{R_0}{R})^{3\kappa}(1 - \frac{3\kappa R'}{c}) - \frac{2\sigma}{R} - \frac{4\mu R'}{R} - p_0 - p(t)] \quad 1.43$$

Some of the assumptions made for this equation are: The radius of the bubble is much smaller than the wavelength of the applied acoustic signal; the spherical shape of the bubble is preserved; the density of the gas inside of the bubble is much less than the medium around; and the timescale of the gas core diffusion is much longer than the time considered here (Plesset M et al., 1977).

1.6.3. Resonance behavior of gas core microbubbles

Assuming the oscillation of the bubble to be small, resonance structure can be seen in equation 1.43. If the radial oscillation of the bubble is expressed by $R(t) = R_0(1 + x(t))$ where $x(t) << 1$ the excursion of the bubble can be estimated to be linear. Substituting the assumed $R(t)$ into equation 1.43 and only taking the first order terms, we can get:

$$x'' + \frac{4\mu}{\rho R_0^2}x' + (\frac{3\kappa\rho_0}{\rho R_0^2} + \frac{2\sigma(3\kappa - 1)}{\rho R_0^3})x = -\frac{1}{\rho R_0^2}(p(t)) \quad 1.44$$

which can nicely match to a format of an harmonic oscillator with force and damping factors $x'' + 2\beta x' + \omega_0^2 x = -\alpha p(t)$. Now we can conclude:

$$\omega_0^2 = (\frac{3\kappa\rho_0}{\rho R_0^2} + \frac{2\sigma(3\kappa - 1)}{\rho R_0^3}) \quad 1.45$$

$$\delta_{vis} = \frac{2\beta_{vis}}{\sqrt{\omega_0^2 - \beta_{tot}^2}} = \frac{2\beta_{vis}}{\omega_0\sqrt{1-\frac{\delta_{tot}^2}{2}}} = \frac{4\mu}{\omega_{res}\rho R_0^2} \qquad 1.46$$

where ω_0 is the eigenfrequency and $\omega_{res} = \omega_0\sqrt{1-\frac{\delta_{tot}^2}{2}}$ is the frequency in which the radial oscillation of the bubble is maximum in amplitude. It is also known as resonance frequency. The δ_{vis} is a constant defining the viscose dimensionless damping at resonance (Leighton, 1994). Looking closer at the resonance frequency shows that if the damping is small the eigenfrequency is the same as the resonance frequency. The δ_{tot} is the summation of all the three damping which are thermal, acoustic and viscous damping.

1.6.4. The addition of a coating

According to equation 1.32 the internal pressure within the bubble exceeds the fluid pressure, in order to balance the outwards overpressure p_σ in the microbubble at the fluid boundary. Such an unbalancing in the forces will push the gas molecule within the bubble to migrate into the surrounding fluid resulting in the volume reduction of the bubble and therefore dissolving. The rate of this dissolution is proportional to the pressure within the bubble which in turn has a inverse relation to the radius of the bubble. It has been shown that the lifetime of micron size bubbles in air saturated water are less than a second (Neppiras E, 1980). This time is very short to use them as ultrasound contrast agent in the human body. The minimum time which takes for the microbubbles to pass from the site of injection to the end organ is about 12 seconds (Goldberg B B et al., 2001). Therefore, stabilizing the gas bubbles is needed to prolong the lifetime as well as resistance against the pressure changes in the heart.

Methods which are mostly used for stabilizing the microbubbles for clinical applications are based on adding materials such as albumin, polymers and phospholipids at the gas-liquid interface, and using the gases which are less soluble such as hexafluoride and perfluorobutane. If elastic solid materials such as albumin and polymers are used for the shell, the stability of microbubbles is caused by supporting a strain to counter the effect of a surface tension. The enhanced stability of microbubbles with surfactants shells such as phospholipids is because of the reduction in the surface tension at the interface of bubble shell and liquid. On the other hand the higher chemical potential of a gas core will increase the diffusion rate of the gas through the surface layer of the microbubble into the suspending medium. If the molecules of the shell are bundled tightly, the gas core cannot easily escape into the aqueous medium, which means enhancement in microbubbles stability. For a summary of different microbubbles and the materials used look at table 1.2.

1.6.5. Subharmonic behavior

Exciting a microbubble near its resonance frequency with a suitable pressure can result in radially asymmetric oscillation which in turn leads to leaking of energy into the higher harmonics of the driving frequency such as second third and higher integer harmonics (Leighton, 1994). On the other hand, microbubbles driven by a certain fraction of their resonance frequencies (f_0) can produce oscillations with frequency fractions identical to the driving frequency (f_0/n, $n= 2, 3,...$), called subharmonic, as well as other integer multiples, termed as ultraharmonic (Parlitz *et al.*, 1990). For example if a microbubble is stimulated by a acoustic pulse with a frequency twice its resonance frequency and above a certain pressure threshold, the bubble will emit a pressure component which has a frequency of half the transmitted frequency (resonance frequency of the bubble), this is called subharmonic emission.

The pressure needed to produce this subharmonic emission from microbubbles is minimum for $n = 2$. As the incident pressure increases the other higher order subharmonic and ultraharmonic maybe provoked (depending on the shell properties and damping) (Parlitz et al., 1990).

The exact explanation for subharmonic response of microbubbles and the threshold behavior is not very well understood. Generally, the asymmetry in stiffness between different phases of the microbubble oscillation is a know source of this behavior (Thompson JMT *et al.*, 2002). It also has been shown that the microbubbles which show the compression only and expansion only behavior have a lower threshold for emitting subharmonic responses (Marmottant *et al.*, 2005, Goertz DE *et al.*, 2007).

There are more sophisticated models which are capable of predicting subharmonic behavior which will be discussed briefly in following section.

1.7. Modeling Ultrasound contrast agent

In the scientific research world models play a very important role in the investigations and discovery of new phenomenon. A very essential part of the studies in any fields are done on the models rather than real experiments. With the help of models a system or a phenomena can be studied in details with a great control to investigate all the different features and fact involved. With models it is possible to have a quantitative reasoning to examinations of the world and hope to see sides which may have been out of scope of others (Silvert W, 2000). Such a cognitive ability of models has been greatly appreciated in the history of science. It has been proposed by some researchers that models bring up a new way of reasoning, so-called ‘model based reasoning’ (Frigg R P, 2006).

Two very important functions can be defined for models in general. First one is that they can be a representation of a selected part of the reality mimicked by them. Those models are normally called phenomenological or data models. Secondly, a theory can be characterized by a model in the way that it explains the laws and axioms behind that theory (Frigg R P, 2006).

A model of a microbubble as a UCA can be a good example for what we said about models. The coated microbubble as a monolayer of lipids separating a gas core from the liquid around, is represented as a phenomenological model. Such a model usually refers only to part of the event in question, therefore even two models of the same phenomenon may differ because of the conceptual or aesthetic dissimilarities by the decision makers during the modeling procedure (Frigg R P, 2006). Within such a phenomenological models group, there is also the data model which is a corrected, rectified, regimented, and in many cases idealized version of the raw data obtained from immediate observations (Frigg R P, 2006). Basically, first step is to eliminate errors (e.g. discarding data points caused by faulty observation) and then presenting the clean data in a efficient way (e.g. drawing a curve through a dataset). Data models are very important and fundamental for confirming theories since it is the model and not the often complex and chaotic raw data that we match up to a theoretical prediction.

The microbubble can also be typified by a theoretical model. Such a concept in modern logic means that a model is a formation in which all sentences of a theory come true, where a theory is defined as a set of sentences in a formal language. This kind of structure is a 'model' since it represents what the theory explains (Frigg R P, 2006).

In section *1.6* we explained the basics of a gas bubble and its reactions to ultrasound by discussing modified Rayleigh-Plesset equation as well as the effect of coating. In the following sections we will try to have an overview of publications considering a variety of coated-bubble models. Of course not all the existing models are mentioned here but we try to introduce references for the most frequently cited models and briefly explain two of the most commonly used models, the De Jong and Marmattant models. For each of these two models some important concepts are covered such as the equation of motion for the bubble wall, the constitutive law for the coating material, the source for the coating parameter values, and the main implications of the model. For having the deeper knowledge for each of the models references are mentioned in which you can find the model descriptions.

1.7.1. The De Jong model(1994)

Based on the theoretical explanation of an encapsulated microbubble vibration De Jong et al. developed a model for UCA in 1994 (de Jong N *et al.*, 1994). The main part of the model is based on the Rayleigh-Plesset equation written by (Eatock *et al.*, 1985), explained in section *1-6*. De Jong model extends the equation of motion for an air-filled, albumin-coated microbubble Albunex (Molecular Biosystems Inc., San Diego, USA). In Rayleigh-Plesset equation, the viscosity of liquid medium around the microbubble is not a separate term and it is considered as part of a total damping term. In other words all the three different sources of damping, liquid viscosity, thermal and radiation, are derived assuming linear conditions and put together in one damping term (Medwin H, 1977). In the de Jong model the effect of the coating is implemented in two parameters, the shell elasticity S_p and the shell friction S_f, then these terms are included in the Rayleigh-Plesset equation. The value for these parameters are established under linear conditions for Albunex contrast agents by comparing the value of calculated acoustic transmission

and scattering to those acquired in measurements (de Jong *et al.*, 1993). The result is the equation for the bubble wall motion as follow:

$$RR'' + \frac{3}{2}R'^2 = \frac{1}{\rho}[(p_0 + \frac{2\sigma}{R_0} - p_v)(\frac{R_0}{R})^{3\kappa} + p_v - \frac{2\sigma}{R} - 2S_p(\frac{1}{R_0} - \frac{1}{R}) - \mu_t \omega \rho_l RR' - p_0 - p(t)] \quad (1.47)$$

where the new parameters p_v is the vapour pressure, ω is the frequency of oscillation, μ_t is the total damping term which contains $\mu_{rad}, \mu_{vis}, \mu_{th}, \mu_{fr}$ where $\mu_{rad}, \mu_{vis}, \mu_{th}$ are radiation, liquid viscosity and thermal damping terms respectively, and $\mu_{fr} = 4\pi R^3 \rho_l \omega$.

1.7.2. The Marmottant model

The main objective of the model introduced by Marmottant in 2005 is to formulate microbubbles with phospholipids coating oscillating at large amplitudes (Marmottant et al., 2005). Using Langmuir-Blodgett balances for measuring the surface tension of flat monolayer, an effective surface tension which depends on the concentration of molecules on surface is described in this model. In this way the bubble dynamics can be driven by an ad hoc law for the surface tension (Emmer, 2009).

In small part of the radial oscillation regime the lipid coating is considered to be a viscoelastic solid. In such a regime, the model is basically similar to the first approach by the De Jong model (de Jong N et al., 1994). Outside of this regime in one side is the ruptured regime were the bubble is considered to break apart and in the other side is the buckling regime where the bubble tends to buckle. In the buckling area, the radius of the bubble is smaller than a defined $R_{buckling}$, and the elastic term as well as the surface tension almost disappear. In the rupture regime the surface tension goes over $\sigma_{break-up}$, which means the bubble radius R exceeds $R_{rupture}$. In this regime the lipid coating breaks apart resulting in the surface tension to become equal to that of free bubbles and the elastic term to become zero. While the elasticity of the coating depends on the bubble radius, the viscosity remains unchanged (Emmer, 2009). In this model the modified Rayleigh-Plesset equation is used. The contrast agents used for the study is SonoVue and BR14 (Bracco, Switzerland) and for the modeling the gas core assumed to be an ideal adiabatic gas. Having all this in mind gives the motion equation as follow:

$$RR'' + \frac{3}{2}R'^2 = \frac{1}{\rho}[(p_0 + \frac{2\sigma(R_0)}{R_0})(\frac{R_0}{R})^{3\kappa}(1 - \frac{3\kappa}{c}R') - p_0 - \frac{2\sigma(R)}{R} - \frac{4\mu_l R'}{R} - \frac{4\kappa_S R'}{R^2} - p_{ac}(t)] \quad (1.48)$$

As we can see from the equation, it is the same as the equation for an uncoated bubble except for the effective surface tension $\sigma(R)$ and the shell viscosity terms. As we explained earlier the surface tension is expressed in three different regimes according to the bubble radius:

$$\sigma(R) = \begin{cases} 0 & if \quad R \le R_{buckling} \\ \chi\left(\frac{R^2}{R_{buckling}^2} - 1\right) & if \quad R_{buckling} \le R \le R_{break-up} \\ \sigma_{water} & if \quad rupture(R \ge R_{ruptured}) \end{cases} \tag{1.49}$$

Where χ is shell elasticity, κ_s is shell viscosity and they are together with buckling radius, $R_{buckling}$. The ruptured surface tension, $\sigma_{break-up}$, is determined by comparing the modeling results with optical observation of vibrating microbubbles.

One of the very important features of this model is that it can predict nicely the nonlinear behavior of the contrast agent such as asymmetrical oscillation which results in subharmonic emission for instance (Overvelde M *et al.*, 2008).

1.7.3. Other models

Since the first model for contrast agent developed by De Jong in 2004, a great variety of coated bubble models have been suggested by now. The basis of the Rayleigh-Plesset equation in all the models has stayed unchanged. By developing new contrast agent with new shell properties also new models were proposed considering the release of new experimental data. The first coated bubble models applied the Kelvin-Voigt constitutive equation, which predicts a linear relationship between stress and strain (Emmer, 2009). Most of the first generation of coated contrast agents had an albumin shell (e.g. Albunex and Quantison) supposed to be relatively stiff and elastic. The main positive point of the Kelvin-Voigt law is that the shell parameter is modeled from a physical basis using two terms, the elasticity and the viscosity of the coating.

Other models than De Jong and Marmottant et al models using the Kelvin-Voigt constitutive equation are Church (Church, 1995); Hoff (Hoff *et al.*, 2000); and Khismatullin (Khismatullin *et al.*, 2002) models.

Morgan (Morgan *et al.*, 2000), Marmottant (Marmottant et al., 2005), and Tsiglifis (Tsiglifis *et al.*, 2008) consider slightly compressibility for the surrounding liquid while the other models assume Newtonian liquid which are uncompressible except for model by Khismatullin, who proposed that the effect of the liquid is outweighed by the effect of the shell properties by studding the comprisable liquid.

The first models that did not used the Kelvin-Voigt constitutive equation were the Morgan model and Chatterjee model (Chatterjee *et al.*, 2003). Chatterjee studied a different type of microbubble, called Optison, thinking that the albumin shell is very thin

and consist of only a few molecules so they applied a Newtonian interfacial rheological model whereby only viscous interfacial stresses are taken into account. MP1950 was another different kind of microbubbles investigated in Morgan model. The coating of this contrast agent is a flexible monolayer of phospholipid molecules. Both investigations however resulted in formations whereby the physical basis can be discussed. To progress in this physical basis, Sarkar extended the model by Chatterjee by adding an elasticity parameter (Sarkar K *et al.*, 2005).

For further improvement in predicting the lipid coated contrast agents, Doinikov and Dayton developed their model in 2007 based on the linear Maxwell constitutive law (Doinikov *et al.*, 2007). In this way instead of using two terms for describing coating as in the Kelvin-Voigt equation, six parameters were used. However, this model is limited only to the small amplitude oscillations.

To overcome the limitation of predicting only the small amplitude oscillation different models started to be developed from 2004 that contain constitutive equations valid for large deformations of the coating. One of the first models in this group is the model by Allen (Allen *et al.*, 2004). They considered polymer spheres with a neo-Hookean elastic response. The coating with such a material can have a specific elasticity, but without a viscosity. The next model specifically developed for large oscillation was the model by Marmottant et al. (2005) as we described it before.

More recent model considering a dynamic elasticity term for the coating was introduced by Tsiglifis in 2008 (Tsiglifis et al., 2008). In this model the elasticity of the microbubble shell is related to the radius by a constitutive law. In this way the shell elasticity can either ‘soften’ or ‘harden’, which also needs adding an empirical term. However the shell viscosity stays fixed.

In the same year a model was developed by Stride (2008), which is not especially designed for large oscillation, but it considers two dynamic shell properties: viscosity and elasticy which are both dependent on the instantaneous radius of the contrast agent. These dynamic coating parameters follow from a description of interfacial tension for insoluble films and not from a constitutive law (Stride, 2008).

1.8. High frequency ultrasound

High-frequency ultrasound (10 to 40 MHz) has a lot of applications in small-animal, preclinical studies and intravascular imaging. The main advantage of using such a high-frequency ultrasound is improved resolution. There are two kinds of resolutions evolved in ultrasound images. One is the lateral resolution (transverse to the direction of beam propagation) directly related to the transmitting frequency. The other one is the axial resolution dependent on the pulse length which is in turn proportional to the frequency and number of cycles. There is often a misunderstanding about the focused transducer that focusing a transducer improves the lateral resolution. This is not true because the lateral resolution is diffraction limited and, hence, solely a function of the aperture of the

transducer and the frequency of the wave. However, the axial resolution, is related to the beam width and it can be improved by focusing. It is perhaps necessary to remind the reader that the resolution of any imaging modalities is effectively limited only by the degree to which the point-spread function is known, and the level of noise (den Dekker *et al.*, 1997). Therefore, a focused transducer, with higher focal gain (The ratio of the pressure at the focus to the pressure at the surface of the transducer) have effectively a better resolution because of their higher signal to noise. High-frequency ultrasound can provide information on different levels such as the morphology, and the perfusion of tissue. Besides clinical applications of high frequency ultrasound systems, the UCA may be used with them as well (Goertz DE *et al.*, 2001), however the response of the microbubble is not completely understood in high frequencies, owing to the nontrivial frequency-dependence of the properties of microbubbles.

1.9. Targeted Imaging

Many applications in biology, such as stemcell treatments (Strauer *et al.*, 2003) and anti-angiogenic therapies (Ferrara *et al.*, 2005), are theoretically simple, but in practice formidable and intractable problems are involved. Binary nature of almost all of the biology experiments on one side and the stream of conflicting data from micro-arrays on the other side are the compounding problems in the field (Tinker *et al.*, 2006). A powerful tool, capable of adding texture to primitive, binary biology experiments and organizing the confusing micro-array printouts, can be targeted imaging. This technology is imaging disease process at the molecular levels. However, a promising perception provided by the heterogeneous difficulty of biology is the concept of using methods such as targeted imaging to advance diagnosis and classify patient risk by correlating progression-free and overall survivals (Ratain *et al.*, 2007). The more promising side of utilizing targeted imaging is to discover the heterogeneity and difficulties of disease procedures in order to get a more sophisticated control of such complex phenomenon. Here we will briefly mention a potential application of microbubbles and high frequency ultrasound as a targeted imaging system. Microbubbles coating can be conjugated with antibodies and peptides which can be specifically targeted to molecules expressed on endothelial cells lining blood vessels (Klibanov, 2007, Bloch SH *et al.*, 2004, Leong-Poi H, 2009) (figure1.6). The microbubble accumulation due to the targeting process can be detected with ultrasonic techniques. This accumulation of targeted microbubbles is expected to show the underlying expression of the molecule, controlled for blood volume, shear rate, geometry, etc., of the blood vessel. One of the very primary problems in applying the targeted microbubbles to a environment such as human body is to create a sufficiently fast and strong binding. This biding mechanism can be copied from similar situation in nature when white blood cells bind to cell receptors responding to infection and foreign organisms. For the readers interested in the details of the chemistry and conjugation methods paper by (Klibanov, 2005) and the references in that paper could be very useful. Next problem is to detect these attached microbubbles and discriminate them from the free moving UCA.

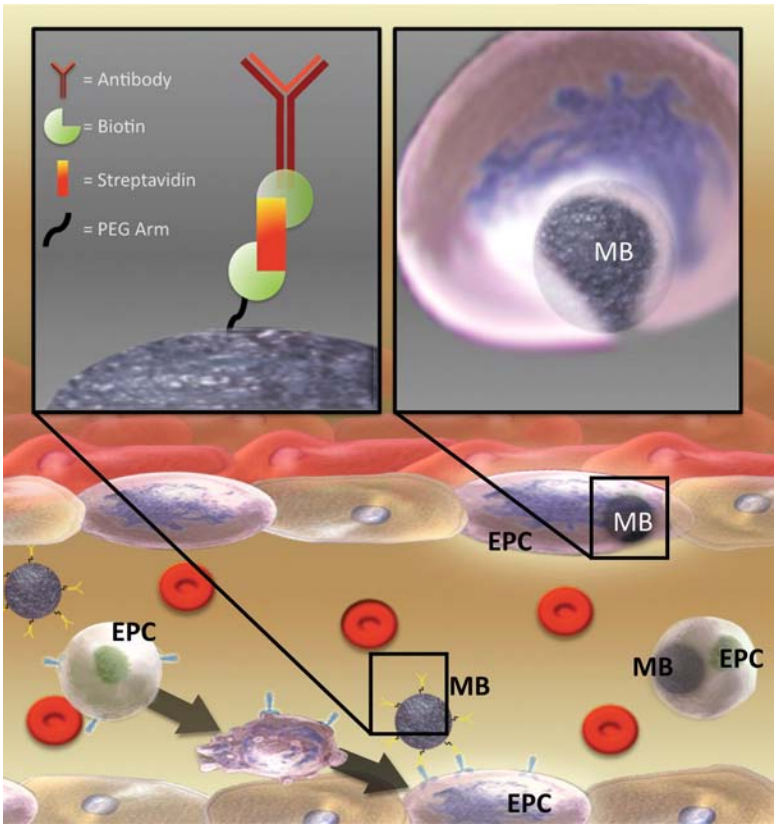

Figure 1.6. Schematic diagram of potential strategies for targeted imaging of Microbubbles (MB) targeted to engrafted EPCs could be constructed by the attachment of the ligand/antibody targeted against the marker protein on the microbubble surface (left aspect of diagram), which when administered intravenously could bind to EPCs that are engrafted within the vasculature, and be imaged by ultrasound. The other strategy involves manipulating EPCs to fully engulf MB, prior to delivery. Once delivered and engrafted, ultrasonic imaging could then detect MBs present within engrafted EPCs (right aspect of diagram) (Leong-Poi H, 2009).

1.10. Project goal

In the context of targeted imaging, the goal of this thesis is to optimize the excitation acoustic pulse used in detecting the UCA at high frequencies. Development of such a new technique for contrast imaging can solve the problem of detecting the attached UCA in targeted imaging. Before thinking about a way to selectively image the bound microbubbles, exciting the UCA at high frequencies in a way to get strong enough echo from them is challenging by itself. Targeted ultrasound imaging using the UCA in such high frequencies are hampered because of incomplete understanding of the UCA in those frequency range as well as being far from the resonance frequency of the normal sized

microbubble. The nonlinearity produced due to the nonlinear propagation of the acoustic wave in the tissue also makes the conventional contrast imaging methods not to be optimal. The key problem this work hopes to solve is to introduce a new method to be used as a nonlinear contrast mode in high frequency systems with acceptable factors such as high tissue cancelation and high contrast to noise ratio.

In chapter two of this thesis the experimental and theoretical setup developed to study the effect of the S-D signal on the SH emission from the UCA, is explained. Then the result of this part is used to implement a new nonlinear contrast imaging mode in chapter three together with showing in vitro and in vivo validation. In chapter four the possibilities and difficulties of using such a methods and the potential usage of this method in selectively imaging the attached microbubbles are discussed.

2 Optimization of excitation burst envelope for subharmonic enhancement

In this chapter we study the use of the S-D signal as a means of microbubble excitation at the SH frequency in order to enhance the SH emission of UCAs. SH emission from the UCA is of interest since this is produced only by the UCA and is free of artifacts produced in harmonic imaging modes. The S-D wave is a low-frequency signal produced by nonlinear propagation of an ultrasound wave in the medium and it can be approximated by the second time derivative of the squared envelope of the transmit pulse. A diluted population of Difinity UCA was insonified by a 10 MHz transducer focused at 76mm firing bursts with different envelopes, durations and peak pressure. The transmitted 10 MHz wave was multiplied with the envelope function: E(t) = exp[- (2t/T)^2M] where T is the nominal duration of the pulse and the integer M determines the rise and decay time of the envelope. The center frequency of the S-D signal is changing from low frequencies (around 0.5 MHz) towards the transmitted frequency (10 MHz) by modifying the envelope function from Gaussian (M=1) to rectangular (M=15). For both 6 and 20 transmitted cycles, the SH response is increased up to 20 dB because of the S-D stimulation when M is equal to 15 (rectangular envelope). The experimental results were confirmed by numerical simulation. The effects of the excitation pulse duration and pressure were also studied. This study suggests that a suitable design of the envelope of the transmit excitation to generate a S-D signal at the SH frequency can enhance the SH emission of UCA and the SH imaging is feasible with low cycle-number transmit burst and low acoustic pressure (~100 KPa).

2.1. Introduction

Angiogenesis, a process in which the formation of new blood vessels takes place, is known to be a key factor for the proliferation of disease processes such as atherosclerosis. Many of the cardiac failures and other events such as stroke have a root in atherosclerotic plaque rupture. This kind of plaques which have a high risk of rupture are called "vulnerable plaque" (Virmani *et al.*, 2000, Schaar *et al.*, 2004). Vasa vasorum which are networks of micro vessels taking the oxygen and nutrients to the arteries wall (Ritman *et al.*, 2007, Gossl *et al.*, 2003) seem to be essential in atherosclerotic plaque pathogenesis and stability (Zamir *et al.*, 1985, Barger *et al.*, 1984). Increase in the vasa vasorum branching in the plaque is suspected as a sign of plaque internal hemorrhage and growth (Mause *et al.*, 2009, Sluimer *et al.*, 2009). Using the noninvasive imaging modalities such as ultrasound for imaging blood flows in the microcirculation can be very important in detecting abnormalities in very early stages. A good example for such a process is measuring the carotid atherosclerosis for the diagnosis and monitoring of patients at risk of stroke (Foster *et al.*, 2000, Eliasziw *et al.*, 1995, Baldassarre *et al.*, 2000). Having the carotid artery not so deep in the body and easily accessible for non invasive ultrasound imaging as well as the new developed methods such as targeted and non targeted contrast enhanced ultrasound make it possible to characterize the carotid vasa vasorum and intra-plaque angiogenesis as signs of plaque vulnerability (Feinstein, 2006, Shah *et al.*, 2007,

Vicenzini *et al.*, 2007, Coli *et al.*, 2008, Staub *et al.*, 2010, Xiong *et al.*, 2009, Shalhoub *et al.*, 2010).

Ultrasound contrast agents, micron size gas bubbles encapsulated by a lipid shell or a polymer, are an effective tools for enhancing the contrast of blood using ultrasound. When expose to ultrasound, the microbubbles reveal resonance due to the compressible nature of the gas inside the bubble. Increasing the amplitude of the acoustic wave can lead in asymmetrical oscillation of the microbubble which in turn results in the leaking of energy to harmonic multiples of the transmit frequency *(f)*. In order to increase the contrast with respect to the tissue around the blood flow, different techniques such as harmonic imaging (Burns, 1996) and pulse inversion (Simpson *et al.*, 1999) was developed to extract the second harmonic (2*f*). The emission of energy at the SH (0.5 *f*o) and ultraharmonic (1.5 *f*o, 2.5 *f*o, etc) frequencies has also been detected (Shankar *et al.*, 1999, Forsberg *et al.*, 2000, Dayton *et al.*, 2002, Shi *et al.*, 2002).

When it comes to use the contrast agents in frequencies higher than conventional clinical rage (3-7 MHz) there are a number of difficulties due to the frequency dependence of tissue and microbubbles (Lockwood *et al.*, 1991). Second harmonic imaging techniques are hampered because of the increase in harmonics produced by the tissue as a result of nonlinear propagation of ultrasound in the medium. In such a situation focusing on the SH frequency may increase the contrast to the tissue ratio (CTR) since it is unique to microbubbles and not produced by the tissue and nonlinear propagation. It has been shown by Goertz et al that the SH imaging technique can give good results with in vivo models such as in mouse and rabbits (Goertz *et al.*, 2005).

The characterization of the SH signal at clinical frequencies has been studied quite well (Shi W T *et al.*, 1997, Krishna P D *et al.*, 1999, Chomas J *et al.*, 2002, de Jong N *et al.*, 2002). Unlike the second and the other higher harmonics that has a continuous quadratic relation with the pressure of the incident wave (Chang P H *et al.*, 1995, Leighton, 1994), the SH is expressing a threshold behavior. This threshold seems to be minimum when the excitation pulse has a frequency of twice the resonance frequency of microbubble and it is also bandwidth dependent (Eller A *et al.*, 1969, Plesset M et al., 1977, Shi W T *et al.*, 1999, Faez *et al.*, 2011). Increasing the pressure of the incident acoustic wave beyond the threshold results in the SH signal growth in strength until a saturation point (Forsberg et al., 2000).

Even though lots of studies have been done on the SH subject, there are only few of them which paid attention to the dependency of the SH emission from the microbubble on the excitation acoustic pulse shape (Zheng *et al.*, 2005, Biagi *et al.*, 2006, Masotti *et al.*, 2007, Zhang *et al.*, 2009). In 2005 Zheng et al. presented a use of multi-frequency excitation, where rectangular and triangular pulses with four harmonics were used to excite the UCA through a numerical modeling via a modified Rayleigh-Plesset equation. They showed that the rectangular wave is effective in improving the nonlinear signal scattered by microbubbles, with effective scattering cross-section area significantly higher (up to 35 times) than the widely-used Gaussian waveform(Zheng et al., 2005). Biagi et al. in 2006 examined ultrasound bursts with three different shapes in order to evaluate the SH response of the UCA, where they found a decrease up to 30 dB in the SH response to a Gaussian-shaped pulse and increase in the SH emission up to 21 dB for a composite pulse (two-tone burst), in respect with sinusoidal burst signals used as

reference pulses. Their experimental results confirmed that the transmitted pulse shape strongly affects the SH emission. Their hypothesis was that the smoothness of the beginning of the shaped pulses can inhibit the SH generation from the UCA (Biagi et al., 2006). In another study, Masotti et al. reported that the SH behavior of UCA is not only pressure and concentration dependant but also a phase dependant phenomenon (Masotti et al., 2007) . Zhang et al. in 2009 also compared a dual-frequency excitation technique with the conventional single frequency sinusoidal excitation technique for enhancing the SH emission from microbubbles and they showed with both simulation and in vitro experiment that a dual-frequency signal (2 and 4 MHz) is able to improve the amplitude of the subharmonic component up to 13 dB over the single frequency sinusoidal excitation technique (Zhang et al., 2009).

Among the studies which have been done on the effect of the pulse shape on the SH emission from the UCA non is explaining the exact reason behind the physical phenomena they see. In this paper, we investigate the effect of S-D signal on the SH response of a phospholipid-coated microbubble at 10 MHz which might be an answer to the question that why optimization the shape of the excitation pulse is important in SH imaging.

2.2. Methods

2.2.1. Sample preparation

Difinity microbubbles ((Bristol Myers Squibb, Boston, MA, USA) were reconstituted to manufacturer's specifications, then diluted 10000 times by volume with a distilled , degassed water. The microbubble solution was then poured into a 10 mm diameter thin shell cylindrical tube made of Polypropylene film backing coated with a water based acrylic adhesive (Tesa® 4024 PV 2) having a total thickness of $52\mu m$. Then the tube containing microbubbles was inserted into the water tank filled with distilled, degassed water. The microbubble consisted of a phospholipid monolayer shell with a perfluoropropane gas core with a peak volume weighted diameter of 6.8 µm. The concentrations used were low enough to enable the assumption of having individual microbubbles at the focus of the transducers to minimize the variability of the measurements.

2.2.2. Experimental setup

The sample was mounted in the center of a equilateral triangular water tank where two transducers were installed in the side walls with 120 degrees in respect to each other. The center of the tube containing the UCA was at the focus of the both transducers used for transmitting and receiving the signals. Magnetic steerer was used to stir the UCA in the tube gently in order to have a homogeneous solution (figure 2.1).

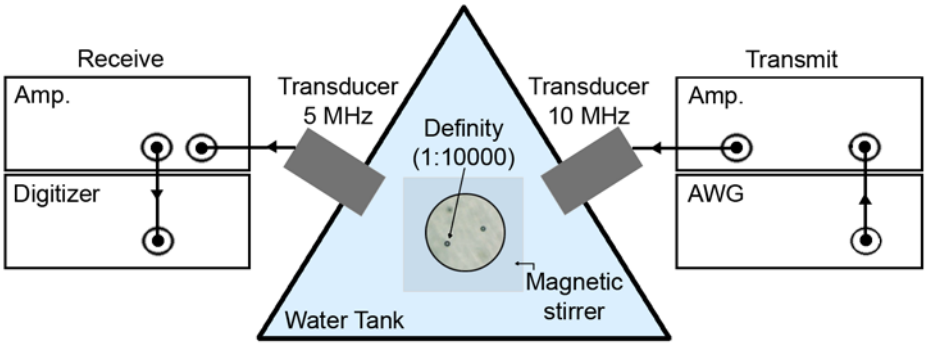

Figure 2.1. Schematic of experimental setup, aligned transducer and tube containing the UCA.

In the direction of wave propagation, the echo from the UCA and the walls of the containing tube was easily separable since the scattering from the walls were stable and not changing in time while the echoes from the UCA change in time because microbubbles are moving constantly. The separation ensured that received echoes were from the UCA and not the linear scattering from walls of the tube.

2.2.3. Acoustic measurements

A broadband 10 MHz centre frequency, 75 mm focal length, single-element, spherically focused transducer (Panametrics V311; 3-13 MHz) was driven at 10 MHz and low pressure of 50 kPa. Pressure values were calibrated using a 0.2 mm PVDF probe hydrophone (Precision Acoustics Ltd., Dorchester, UK). An envelope functions for the transmit bursts were defined by the following formula:

$$E(t) = e^{-(\frac{2t}{T})^{2M}} \qquad 2.1$$

where T is the nominal duration of the pulse and the integer M determines the rise and decay time of the envelope. The envelope of the transmit burst was varied from Gaussian to rectangular shape by changing the M from 1 to 15. Then the sinusoidal 20-cycle burst at 10 MHz were modulated by these three different envelopes having the M values of 1,3 and 15. The pulses were generated by an arbitrary wave generator (8026, Tabor Electronics Ltd., Tel Hanan, Israel) and amplified with a gated 60 dB pulse amplifier (Amplifier Research, 150A100B). The scattered pressure waves were received, amplified by 60 dB and digitized by an 12-bit ADC at a sampling frequency of 500 MHz. The receive acquisition settings were kept constant. At 5 MHz the one-way transducer frequency response was 5 dB lower than the maximum response at 10 MHz. One hundred sets of pulses were transmitted with peak negative pressures (PNP) of 50 kPa with a pulse repetition frequency of 1 kHz.

2.2.4. Simulation

In order to investigate the influence of the S-D signal and the driving frequency on the SH response of the UCA, we linked the KZK model (Hamilton et al., 1998) with the model of Marmottant (Marmottant et al., 2005). The KZK is used to simulated the propagation of the 20-cycle, 50 kPa acoustic burst with three different envelopes (M: 1, 3 and 15) in water and at the focus of a 10 MHz circular focused transducer with a diameter of *10 mm*. The focal length of the transducer was set the same as in experiment, *76 mm*. The Marmottant model simulate the bubble dynamics in response to the output of the KZK block (figure 2.2). Both the KZK and Marmottant models were discussed in more detailed in the chapter 1. We used exactly the same acoustic burst as we did for the experiment as an inputs for the KZK model. The bubble radius for the Marmottant model set to be 1μm.

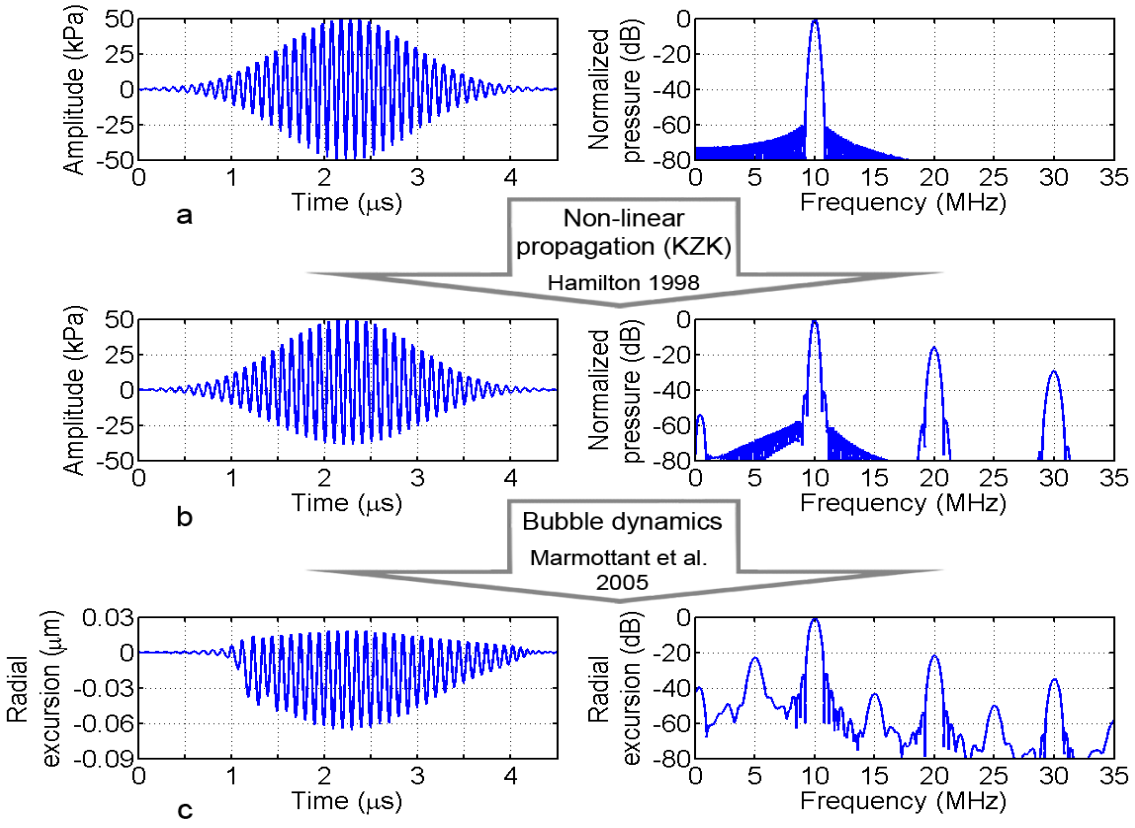

Figure 2.2. Schematic of the KZK and the Marmottant blocks used for the simulation. a: shows the input signal with a single peak at 10 MHz in the frequency domain. b: shows the signal after being propagated in water which contains higher harmonics as well as the low frequency S-D signal. c: shows the response of a single microbubble to the distorted acoustic wave.

According to the Marmottant model to get subharmonic oscillations a sharp change in the elasticity is required (Overvelde *et al.*, 2010) which means that in the elastic regime, where the elasticity doesn't change rapidly, not so much SH behavior can be expected. Since we are using a low acoustic pressure we do not expect to push the bubbles towards the rupture regime, therefore the only chance to get the maximum SH emission from the simulated microbubble is to set the surface tension in the buckling regime as it has been observed by (Sijl *et al.*, 2010). Therefore in the simulations we choose the initial surface tension to be very close to the buckling regime but not zero. Instead of taking the buckling radius (R_b) of the microbubble to be constant as it is in the original Marmottant model the following formula was used for R_b (Overvelde et al. 2010).

$$R_b = \frac{R_0}{\sqrt{\frac{\sigma(R_0)}{\chi}+1}} \qquad 2.2$$

Where χ *=2.50* N/m is the shell elasticity (Overvelde et al., 2010), $R_0 = 1 \ \mu m$ is the initial radius of the microbubble, and $\sigma(R_0) = 0.0991 \ N/m$ is the initial surface tension of the microbubble.

2.2.5. Data analysis

Recalling from chapter 1 the energy of the S-D signal is concentrated in the beginning and the end of the burst. Therefore in order to remove that part of the signal which corresponds to the linear scattering of the S-D signal, a Hanning time window was applied to discard 3 periods at 10 MHz from the beginning and the end of the received scattered signal. Sets of 100 pulses were averaged in the frequency domain in order to increase the signal to noise ratio and make the SH frequency peak more distinguishable. Since we study the differences in the SH emission from the UCA in response to pulses with different envelopes and not the absolute values of SH signal, the correction for attenuation or the transducer's frequency response is not done. The energy content of all the three different bursts used for transmission were set to be the same in such a way that the SH response of the UCA could directly be compared, however the comparison is done in between the ratio of the SH peak to the fundamental peak.

2.3. Results

Figures 2.3 to 2.5 show a representative series of measurements and simulations for 20-cycle pulses with three different envelopes having a pressure of 50 kPa. A 0.01% diluted population of Definity UCA was insonified by a 10 MHz transducer in the experiment and a single bubble with radius of $R_0 = 1\ \mu m$ was used for the similar situation in simulation. Using the KZK simulation three transmitted bursts with a PNP of ~50 kPa with three different envelopes at the surface of the transducer and at the focus and their corresponding Furious transform are shown in figure 2.3. In this figure the graphs in the frequency domain with dash lines correspond to the Fourier transform of the time signal at the surface and the solid lines represent the Fourier transform of the time signal at the focus of the transducer. The green ellipses indicates the S-D signal which are popping up for the burst at the focus. The received echo is shown in figure 2.4 representing a clear SH component at 5 MHz for all the three different bursts and finally figure 2.5 shows the result for the simulation using the linked KZK and Marmottant models.

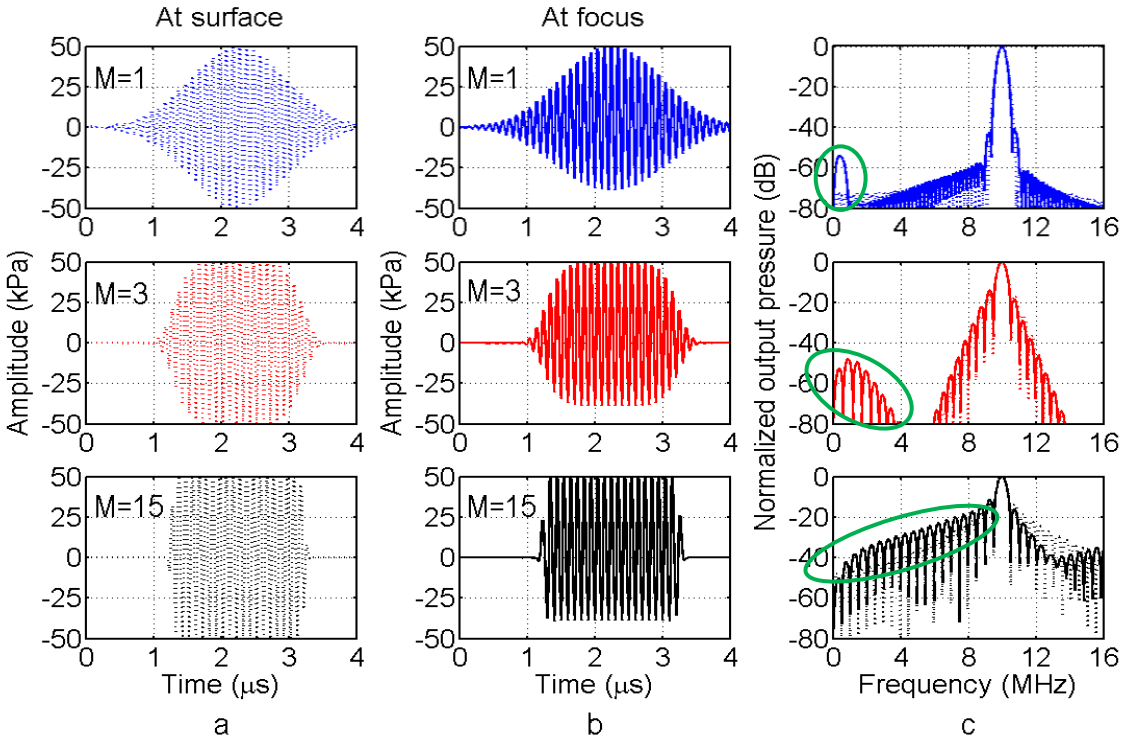

Figure 2.3. KZK simulation showing the 20-cycle, 50 kPa burst for three different envelopes (*M: 1, 3 and 15*) at the surface of the transducer (**a** column), at the focus (**b** column), and their corresponding frequency contents (**c** column) (green ellipses shows the position of the S-D signal).

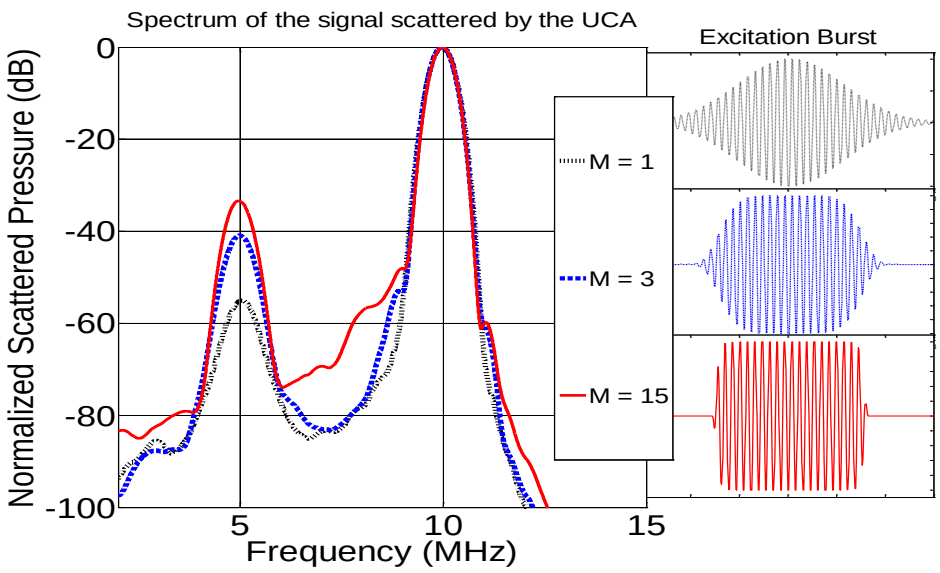

Figure 2.4. Experiment results showing the Fourier transform of the scattered signal from the UCA and three 20-cycle, 50 kPa pulses with three different envelopes used as excitation bursts.

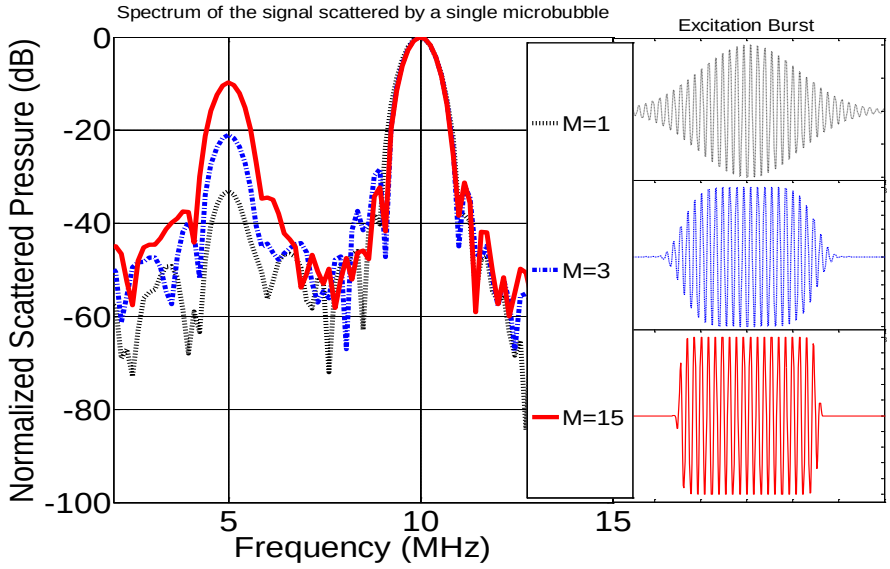

Figure 2.5. Simulation results showing the Fourier transform of the scattered signal from a single microbubble and 20-cycle, 50 kPa pulses with three different envelopes used as excitation bursts $(R = 1\mu m,\ \ \sigma = 0.0099(N/M))$.

To compare the SH signal, the received echoes were normalized to their maximum and then the ratio of the SH amplitude to the fundamental amplitude were used for

comparison. In this way, keeping in mind that the beginning and the end of the received signals have been windowed, we can be sure that the differences in the SH to fundamental ratio comes from a true enhancement in SH responses and not the linear scattering of S-D signal and leakage of energy have been minimized.

2.4. Discussion

Results of the KZK simulation in figure 2.3 shows the effect of the pulse shape on the S-D signal produced due to the nonlinear propagation. In section 1.4.2 we showed that the S-D signal is proportional to the second time derivative of the squared envelope of the carrier high frequency ultrasound burst. The three pulses with different envelopes tested here are made only by changing the M in equation 2.1 which means only the decay and raise time of pulses have been change. For M=1 we have a Gaussian-like envelope and the higher the M gets the more rectangular the shape of the pulse will be. The center frequency of the S-D signal is changing from low frequencies (around 1 MHz) towards the fundamental frequency (10 MHz) by changing the envelope of the 10 MHz transmit burst from Gaussian to rectangular (by changing the "M" from 1 to 15). The S-D signals for different transmit bursts are indicated by the green ellipses in the frequency domain in figure 2.3. We can see that the frequency content of the S-D signal for a rectangular envelope (M=15) is not a clear single peak as it is for a pulse with a Gaussian envelope (M=1) and it is more like elevation in a wide range of low frequencies (from 3 to 8 MHz) with a center close to 5 MHz. The reason is clear because the frequency content of the squared rectangular envelope is different compare to a Gaussian envelope. This is because to make the rectangular shape more frequencies are involved while a Gaussian shape can be produced by a single low frequency component.

Subharmonic energy at 5 MHz was observed for all transmitting bursts with different envelopes, having different S-D signals, with clear distinguishable peaks from the fundamental peaks at 10 MHz. By changing the envelope from a Gaussian shape to a more rectangular shape the energy of the SH responses produced by the UCA increases monotonically up to 20 dB (figure 2.4). This enhancement of the SH emission because of the shape of the pulse is in a agreement with the previous studies (Zheng et al., 2005, Biagi et al., 2006, Masotti et al., 2007, Zhang et al., 2009). It seems that having more energy of the S-D signal at the SH frequency can stimulate the microbubble to oscillate more asymmetrically and produce more SH signal. It was mentioned in (Biagi et al., 2006) that having a Gaussian shape prevent emission of the SH, however we think that having a rectangular shape stimulates the SH emission and there is no prevention effect involved with Gaussian shape. The reason for such a stimulation effect might be the more energy at the SH frequency due to the S-D signal in the acoustic burst with rectangular shape in respect to the one with Gaussian envelope.

Figure 2.5 shows the result from numerical simulation which is in a very good agreement with the results of experiment. Of course the initial values of the radius of the microbubble and the surface tension for the numerical simulation is very important. Both of these factors have direct influence on nonlinear emission from the UCA such as the

SH response in the model. The radius actually represents the resonance frequency characterization of the bubble and the initial surface tension has a great impact on SH response since it is indicates the position of the bubble in the three states: rupture, linear and buckling graph in Marmottant model (Marmottant et al., 2005, Overvelde et al., 2010). In order to find a right size for the bubble which results in maximum SH response for our simulation we swept a rage of different bubble radiuses for transmit frequency of 10 MHz. The maximum SH response for a 20-cycle 10 MHz Gaussian shaped burst was found to happen when $R = 1 \ \mu m$. Different values for initial surface tension was also tested by sweeping method and the most similar results to the experiment found when $\sigma = 0.0099 \ \ N/m$.

Since the maximum SH response takes place when the surface tension is in the bucking regime readers might indeed ask why not having the initial surface tension equal to zero instead of a value close to zero to have the maximum SH response. The answer for such a question is: since we want to see the effect the of the S-D signal on SH emission this effect is more clear if the microbubble has an initial surface tension a bit above zero. In this way we can see that the S-D signal can actually push the bubble towards the bucking regime and that is what we call the stimulation effect of the S-D on the SH emission. Having the minimum value for surface tension $\sigma = 0 \ \ N/m$ will not result in showing the enhancement of the SH response using the S-D signal because the bubble already is giving the maximum SH emission even using the Gaussian envelope. Therefore in such a position, the microbubble does not need to be stimulated by the S-D signal. However, being slightly above the buckling regime (e.g. $\sigma = 0.0099 \ \ N/m$) results in not having the maximum SH response for the Gaussian-shaped pulse but for the pulse which has slightly more energy at the resonance frequency of the bubble (half the transmitting frequency). As it was explained earlier this energy at the SH frequency coming from the S-D signal for the excitation pulse with a rectangular envelope. In this way the mechanism behind this stimulation effect of the S-D signal on the SH response of microbubbles can be predicted by the Marmottant model.

Readers should also recall that the amplitude of the S-D signal itself is very low and it is within a range of 50 to 30 dB below the amplitude at the fundamental frequency (Vos *et al.*, 2010). Comparing the frequency content of the rectangular-shaped pulse at the surface of the transducer and at the focus in figure 2.3 might be misleading since the amplitudes at the SH frequency (5 MHz) are only 15 to 10 dB below the amplitude at 10 MHz. The reason that we do not see the lower values which we expect is that the low frequency content of the envelope as well as the S-D signal are combined by the side lobes as the result of energy leakage of the fundamental due to windowing. This is not influence the effect we try to study in this work since we are more interested in differences between the amplitudes around the SH frequency for the burst at the surface (without the S-D signal) and the burst at the focus of the transducer (containing the S-D signal) which is about 10 dB. However still one might ask that the enhancement we see might be only because of the low frequency component in the envelope itself as a rectangular envelope contains several different low frequency components. One way to answer this question is to repeat the experiment with two burst with rectangular envelope but one with the S-D signal and the other one without. Unfortunately it is not possible to filter out the S-D signal in the experiment since it is a low frequency signal which is

spread all over from the fundamental frequency to the very low frequencies but it can numerically be simulated. For that we run the simulation for a bubble with a radius of $1\mu m$ and then sweep the initial surface tension from *0* to *0.1 N/m*. This time instead of using burst with different envelopes, two 20-cycle, 50 kPa rectangular envelope burst are examined. One is from the surface of the transducer where the S-D signal is not built yet and the other one is the wave after propagating 76 mm in water and contain the S-D signal (figure 2.5 third row). The differences in the amplitude of subharmonic emission from the microbubble in response to these two different bursts for different initial surface tension is shown in figure 2.6 with the blue curve.

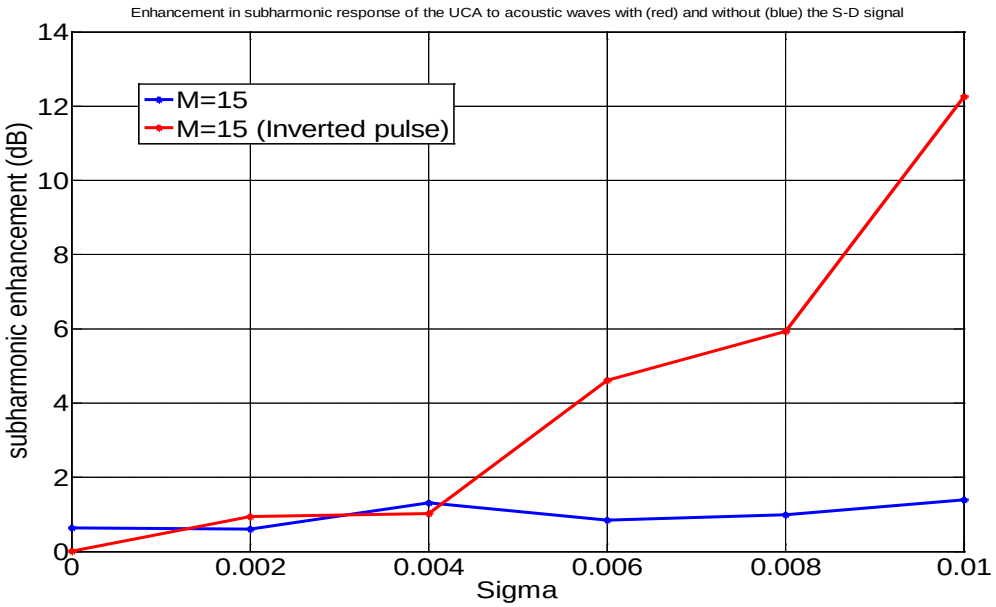

Figure 2.6. Simulation results showing the enhancement of the subharmonic response of a single microbubble to a 20-cycle, 50 kPa rectangular envelope acoustic burst at the surface of the transducer and at the focus of the transducer (blue) and the inverted pulses (red) $(R = 1 \ \mu m)$

Looking at the blue curve in figure 2.6 one can see there is almost no differences between using the burst with rectangular envelope at the focus of the transducer containing the S-D signal and the other one at the surface of the transducer without the S-D signal. if we look at these two acoustic bursts and their frequency content filtered by a low pass filter with a cutoff frequency of 6 MHz (figure2.7 first row) we can see that the low frequency content of the envelope itself (dotted red curve) is in phase with the low frequency so called the S-D signal. It means that both of them have a positive pressure phase at the beginning of the burst which can probably push the bubbles towards the buckling regime. This similarity in the amplitude of the SH emission using these two bursts can be explained in this way. However, if we just invert the transmit burst and keep the rest of

the settings as before, since the S-D signal is related to the second time derivative of the squared envelope, it stays the same while the low frequency component of the envelope itself will be converted which means a negative pressure instead of a positive pressure at the beginning of the burst (figure 2.7 second row). The simulation results for this situation is the red curve in figure 2.6 which clearly shows the enhancement of the SH emission for the acoustic burst containing the S-D signal compare to the one without the S-D signal and having the same rectangular envelope.

According to the formulation for the S-D signal inverting the high frequency carrier wave should not change the S-D signal at all. The dissimilarities that we see in figure 2.7 between the blue and black curves, which suppose to show the S-D signal for the pulse and the inverted one, is because of the low frequency component of the envelope itself which has not been filtered out from the S-D signal. These components will be inverted by inverting the transmitting burst. Therefore some distortion in the S-D signal is presented. Regardless of this change in the shape of the S-D signal for the inverted burst, having a positive pressure at the beginning of the pulse is more important since it is responsible for pushing the bubbles towards the buckling regime.

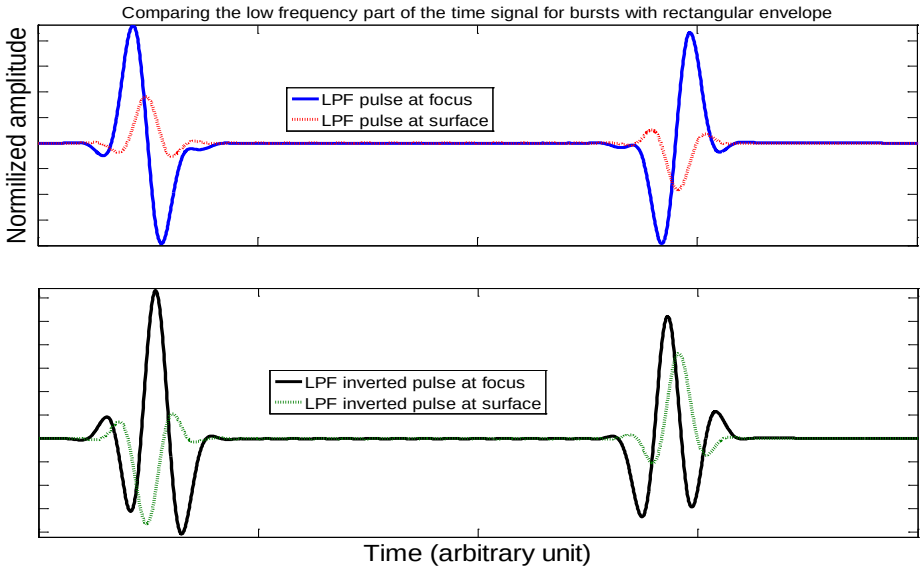

Figure 2.7. Simulation results showing the low pass filtered (LPF) pulses at surface and focus of the transducer (cutoff frequency of the LPF: 6 MHz).

The result of these simulation confirms our explanation that: The S-D signal which starts with a positive pressure at the beginning of the transmitting burst can push the microbubble towards the buckling regime where oscillation in response to the rest of the burst gives a higher SH emission.

One of the problems that we might face when using such a technique in imaging applications is the poor axial resolution due to the long length of the transmitting burst. The experiment are done with a 20-cycle burst because it is easier to distinguish the S-D component in the transmitting pulses as well as the SH component in the scattering signal from the UCA. According to the physical background and numerical simulations our hypothesis to explain the stimulating effect of the S-D signal on the SH emission is not dependent on the pulse length at all. To prove that exactly the same experiment was repeated but this time with a 6-cycle burst instead of 20-cycle. Figure 2.8 shows the results of this experiment.

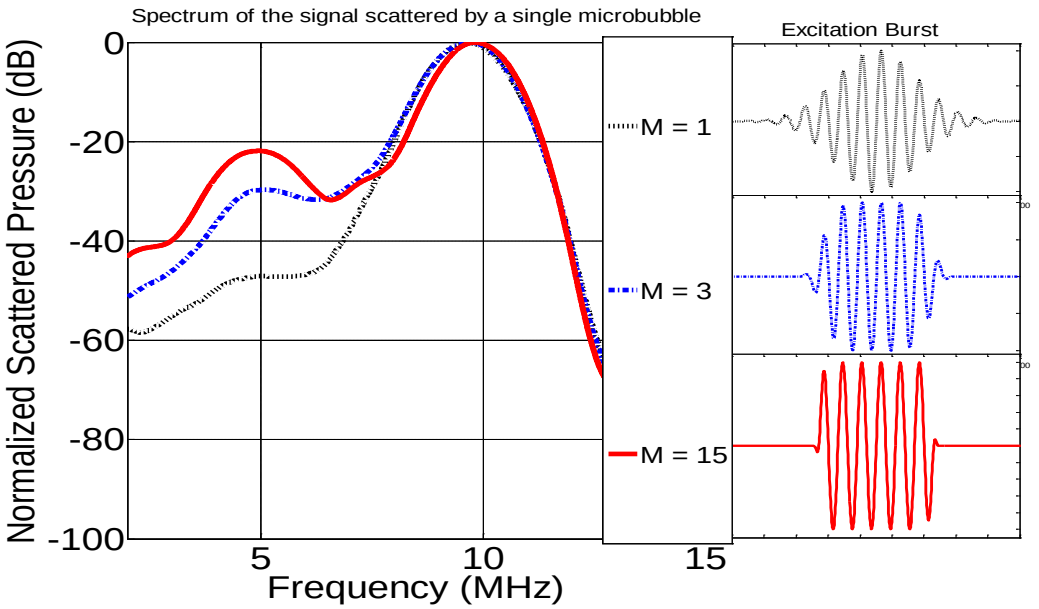

Figure 2.8. Experiment results showing the Fourier transform of the scattered signal from the UCA and 6-cycle, 50 kPa pulses with three different envelopes used as excitation bursts.

Figure 2.8 shows that unsurprisingly the same results as for 20-cycle bursts are presented except that the SH peaks are more clear and apart from the fundamental peak in the experiment with 20-cycle pulses. The almost 20 dB enhancement in the SH response of the UCA due to the S-D signal around the SH frequency in a rectangular envelope can be appreciated in figure 2.8 even for a ultrasound burst with a lower number of cycles.

For using such a technique in a imaging modality, the linear scattering of the S-D signal itself should also be considered carefully. Although the S-D signal is a very week signal it can be scattered by not only the UCA but also by the tissue which results in decreasing the CTR. On the other hand, the enhancement in the SH response (20 dB) of the UCA due to the S-D signal is much higher than the level of the S-D signal itself. Therefore optimizing the shape of the excitation pulse in a way to have the maximum energy of the S-D will always be beneficial in increasing the CTR and the nonlinear response of the

microbubbles. The other solution might be to use other fraction of the SH response such as ultraharmonic to minimize the effect of the linear scattering of the S-D signal while keeping the enhancement in the ultraharmonic emission.

2.5. Conclusions

Even though the low amplitude self-demodulated pulse alone may not be able to excite microbubbles efficiently, our result shows it can effectively stimulate the SH response of the UCA. Our hypothesis for such a phenomena is that the microbubbles are pushed towards the buckling regime by the positive pressure of the S-D signal at the beginning of the transmitted burst which results in presenting the maximum SH emission in response to the rest of the burst. This hypothesis are confirmed by the numerical simulation using the linked KZK and Marmattant model. Besides the limitations in optimization the excitation pulse as well as in SH response of the UCA this study suggests the SH imaging is feasible, thanks to the S-D signal, with low acoustic pressure (~100KPa) and low cycle-number transmit burst (6 cycles), hence providing a good compromise contrast/spatial resolution.

3 High frequency nonlinear contrast imaging

Results of the single element study in the previous chapter suggested that optimizing the envelope of the excitation burst can enhance the SH response of the UCA up to 20 dB. In this chapter such an optimized enveloped in combination with conventional contrast detection methods (AM and PI) are used for nonlinear contrast imaging at high frequencies. Such a new method was implemented in a commercial ultrasound scanner and different phantom studies were done The results were then validated in vivo using a chicken embryo model.

3.1. Introduction

Current progress in high frequency ultrasound imaging technology have pushed traditional frequencies into the higher range of 10–70 MHz using linear array transducers (Ritter *et al.*, 2002, Lukacs *et al.*, 2006, Brown *et al.*, 2007). Improved depth of field and overall image quality and more flexibility in pulsing schemes for imaging are the key advantages of such a new technology compared to the old single-element transducers used in previous generation of micro-ultrasound systems. In the contrast mode imaging techniques using post-processing subtraction algorithms the echoes from UCA can, in certain conditions, be visualized above the tissue echoes (background). However, in lots of clinical applications such as for tissue perfusion conditions due to the low concentration of the UCA used in small capillaries the backscattered signal from the microbubbles are below tissue levels, making the selectively imaging of the UCA difficult (if not impossible) by subtracting images or signals after rf demodulation (Needles *et al.*, 2010). Other difficulties in image subtraction methods are the motion artifacts due to breathing and cardiac-induced motions. In order to gain high sensitivity in contrast imaging, tissue backscatter signals must somehow be taken away from the received echoes, while keeping signals produced by UCA. This can preferably be done by new imaging strategies where multi-pulse schemes are used instead of single transmission pulse. In these methods each line of sight is imaged by sequences of transmit pulses, with rf-echo processing designed to remove the tissue backscattered signal (linear echo components). In addition to enhance the sensitivity in such an approach, the detection and visualization of UCA will be done in real time. In the ultrasound systems with array transducers it is easily possible to electronically control desired transmit and receive beam patterns and the latter focused can be dynamically set for all depth samples in the image (Needles et al., 2010) providing a significant and valuable improvement in depth of field and, therefore, an overall enhancement in UCA detection over image depth.

3.1.1 Nonlinear contrast agent detection

It has been shown that ultrasonic nonlinear imaging provides higher image quality and a better contrast compared to conventional linear imaging techniques, making it become an important valuable diagnostic tool in many clinical and biomedical applications (Gramiak *et al.*, 1969, Ophir *et al.*, 1989, Tranquart *et al.*, 1999, Desser *et al.*, 2001) and many techniques have been proposed for nonlinear imaging of UCA (Burns, 1996, Chang P H et al., 1995, Simpson et al., 1999, de Jong *et al.*, 2000, Phillips, 2001, Deng *et al.*, 2002). Two different sources generate the nonlinear echoes in clinical applications: the tissue and the UCA which are usually introduced into the vascular beds via intravenous administration. Nonlinearity generated by the tissue is due to the nonlinear propagation which was explained in section 1.3 in more details. This nonlinearity can be mainly characterized by the generation of harmonic signals whose frequencies are at multiples of the fundamental (F) transmit frequency as well as the S-D signal (see section 1.4.2). The acoustic waveforms before and after nonlinear propagation and their corresponding spectra are shown in Figure 4-1.

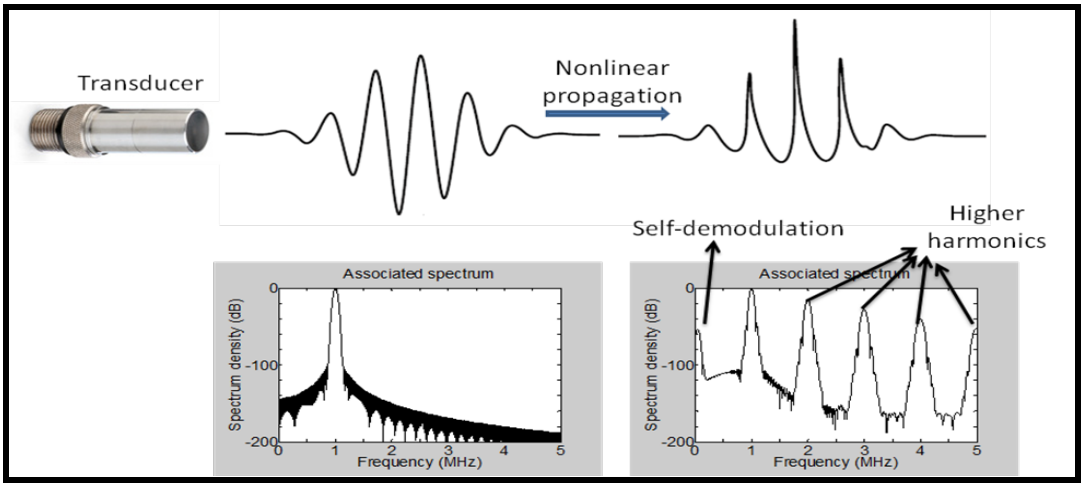

Figure 3.1. Transmit ultrasound wave, a nonlinearly deformed wave and their associated spectra.

Since the tissue harmonic and the S-D signals are generated gradually throughout the propagation path, these nonlinear terms are weak in the near field. Though the reverberations from imaged targets in the near-field are reduced in nonlinear imaging. For UCA, the generation mechanism of nonlinearity is different than nonlinear propagation. Due to the acoustic impedance mismatch between blood and the gas core of UCA, microbubbles produce strong backscattered signals (Goldberg *et al.*, 1994). Therefore, using UCA can enhance both grayscale images and Doppler signals. Furthermore, microbubbles exhibit strong nonlinear oscillations especially if excited near their resonance frequencies (Chang P H et al., 1995). Nonlinearities generated by UCA include not only the harmonic but also the SH frequencies (de Jong, 1996, Shi *et al.*,

2000). In conventional F imaging, the dominating echoes from both microbubbles and tissue are the linear components, and often on a similar order of magnitude for high transmit frequency, making the separation of microbubble echo from tissue signal difficult. The main challenge in contrast imaging, therefore, is to design particular pulse sequences and signal processing which provides maximum UCA detection efficiency while removing signals originated by tissue. Using properties of the microbubble nonlinear oscillations, nonlinear imaging using the UCA is improved compared to its linear counterpart, however the performance of nonlinear imaging is still limited. For instance, the nonlinearity which is produced in an imaging system itself can degrade the image contrast (Che-Chou *et al.*, 2001). Also the signal to noise ratio and contrast to tissue ratio (CTR) in tissue harmonic imaging, which are also important factors for imaging, are sometimes insufficient, especially in the near-field area (Li *et al.*, 1999).

Conventionally, nonlinear components such as harmonic signals are extracted from the received echo by applying a filter at the desired frequency (Averkiou *et al.*, 1997, Christopher, 1997, Ward *et al.*, 1997). Although filtering can be implemented efficiently, spectral leakage can result in potential contrast degradation. Therefore other development of other signal processing techniques free from this leakage problem seem to be necessary. Among all the different methods which have been developed for medical applications the pulse inversion (PI) and amplitude modulation (AM) techniques are the most promising methods for improving the performance of nonlinear imaging. These methods offer enhanced image quality and improved diagnostic abilities by reducing potential interference from the linear part of the propagated acoustic wave.

3.1.2 Conventional contrast imaging

Instead of filtering, the PI method can be used to extract the nonlinear signals emitting from the UCA. PI was for the first time introduced by (Simpson et al., 1999) and uses two transmit ultrasound waves that are sent one after the other into the medium, with the second pulse being an identical but inverted copy of the first. According to the characteristics of linear systems, adding up the echo signals resulting from the two transmit pulses ends up in removal of all linear echo components of the tissue, and preserving the nonlinear signals from UCA. PI keeps even-order harmonics such as second harmonic as well as the SH, and removes odd-order harmonics. It has been shown that, at low transmit frequency, PI improves CTR relative to F imaging (Eckersley *et al.*, 2005) (i.e., 14 dB enhancement in CTR at a transmit frequency of 2 MHz). At higher frequencies, Goertz et al (Goertz D E *et al.*, 2006) investigated PI with a 30 MHz intravascular ultrasound transducer for both SH and second harmonic imaging. This study showed an improvement in CTR ranging between 10–20 dB (second harmonic) and 5–15 dB (SH) for transmit peak negative pressure range of 0.1 to 2 MPa. They also reported that at such high frequencies, the enhancement in CTR using the PI method decreases dramatically as imaging depth and transmit pressure are increased, especially for second harmonic imaging. A schematic diagram of the PI method is demonstrated in Figure 3.2.

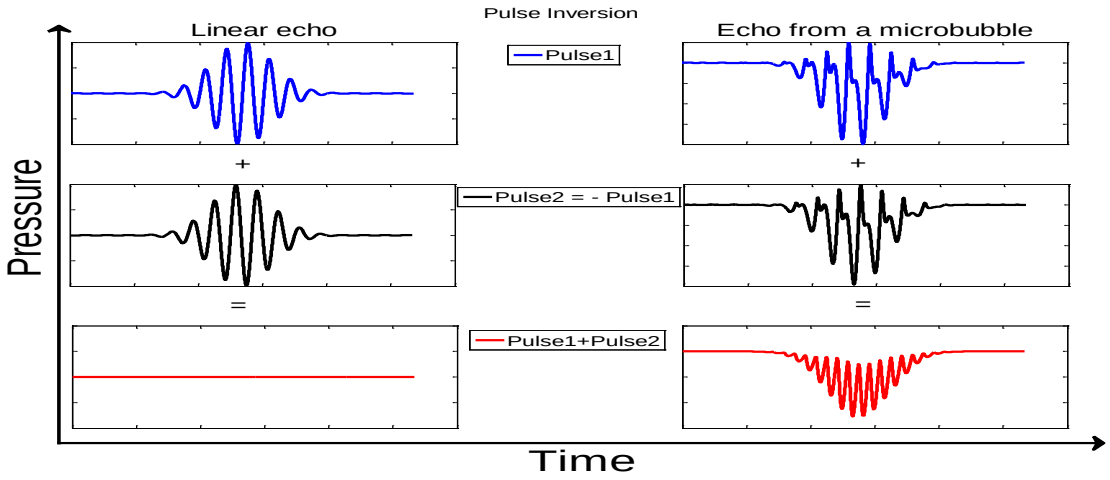

Figure 3.2. Schematic diagram of the PI technique for extracting the nonlinear terms of the UCA oscillations.

In AM technique (also known as power modulation) two ultrasound pulses are sent consecutively into the tissue, with the first pulse scaled by a factor *A* relative to the second pulse (Brock-Fisher G *et al.*, 1996, Phillips, 2001, Eckersley et al., 2005). The backscattered echoes, after scaling the signal in response to the second pulse by the same factor *A*, are subtracted from each other. Based on the properties of linear systems the linear component in the echo is canceled, while retaining components resulting from the imperfect cancellation of nonlinear UCA echo signals (Figure 3.3). It can be shown that AM keeps nonlinear energy at the F frequency, in addition to even-order harmonics such as the SH frequency (Eckersley et al., 2005).

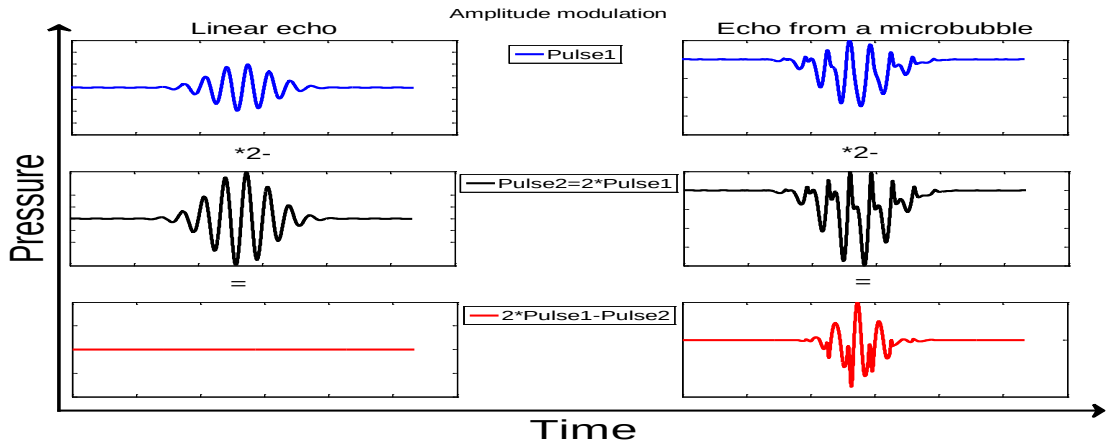

Figure 3.3. Schematic diagram of amplitude modulation technique with a scaling factor *A=2* for extracting the nonlinear terms of the UCA oscillations.

As shown in figures 3.2 and 3.3 both PI and AM methods can extract the nonlinear component of the backscattered signal without interference from any linear terms of the signal. In other words, potential spectral leakage in ultrasonic nonlinear imaging which was the main problem in conventional filtering method can be avoided with the PI and AM techniques.

In most of the conventional ultrasound frequency the nonlinear imaging methods are used to extract the energy at the second harmonic. However such approach is less effective at higher frequencies for two main reasons (Needles et al., 2010): First, the level of second harmonic produced by the tissue due to the non linear propagation is high even at low transmit pressures (Goertz et al., 2005). This reflects the frequency dependence of nonlinear propagation in tissue, especially as the transmit pressure is increased for increasing imaging depth. Second, due to the frequency dependence of ultrasound attenuation in most soft tissues, the level of energy at second harmonic for high transmit frequencies suffers from higher attenuation compare to at lower transmit frequencies. Therefore commonly used contrast imaging techniques such as PI and AM performing very well at low frequencies suffer from poor tissue cancelation at higher frequencies. In addition, the limitation in the bandwidth of the most of high frequency probes makes it imposable to look at the second and higher harmonics. The goal of this chapter is to determine the optimal imaging strategy for a real-time nonlinear contrast mode, using a high frequency ultrasound system with the array-based transducer and validate such an optimal method both in vitro and in vivo. In the following section based on the method we developed in chapter 2, a practical approach is proposed.

3.1.3 Novel contrast imaging method

Since the S-D signal is proportional to the second time derivative of the squared envelope of the transmitting ultrasound burst ($p_{sd} \propto \partial^2 E^2(t)/\partial t^2$) (Averkiou et al., 1993), by inverting the transmit pulse, the S-D signal stays the same because the squared envelope is unchanged. Therefore adding the two pulses in the PI method will double the S-D signal in amplitude. On the other hand, in the AM technique (with $A=2$) the S-D signal in the pulse with double amplitude is four times higher than in the other pulse, because in the weakly nonlinear regime there is a quadratic relation between the amplitude of the transmitting envelope and the S-D signal (Vos et al., 2010). Hence, doubling the echo from the pulse with half amplitude and subtracting it from the other pulse, the S-D signal will be enhanced by a factor of two. In the other hand in chapter 2 we showed that optimizing the shape of the transmit pulse in such a way that the S-D will be around the SH frequency, can enhance the SH emission from the UCA up to 20 dB. Therefore applying the PI or AM techniques together with an optimization of the pulse envelope and imaging at the SH frequency might provide a contrast imaging mode with a better tissue cancelation and consequently higher CTR.

3.2. Methods

The MicroMarker (VisualSonics Inc., Toronto, Canada) UCA was used in this study. These microbubbles consist of phospholipid shell encapsulating a C4F10/N2 gas core. These are obtained after reconstitution of a lyophilisate cake with 0.7 mL of 0.9% saline, resulting in a concentration of approximately 2.10^9 bubbles/mL, with a mean bubble diameter of 1.2 μm (Needles et al., 2010).

A high frequency pre-clinical ultrasound scanner (Vevo 2100, VisualSonics Inc., Toronto, ON, Canada) was operated at 18 MHz, with a 256-element linear array transducer (model MS-200). The frequency response of the transducer measured in the pulse echo experiment with a flat Steel plate is presented in figure 3.4. An in-phase quadrature (I/Q) sampling method (Powers et al. 1980) was implemented in the system and the sampling rates is set to be double the transmit frequency(2*18=36 MHz in our case) in this way the sampling process allowed non-aliased quadrature sampling of signals having a spectrum in the range zero to transmit frequency, therefore the SH, and wideband F signals from microbubbles and tissue are properly sampled while unwanted second harmonic sampled signals is not fold back into the frequency range of interest through aliasing (Needles et al., 2010). Through measurement, the focus of transmit ultrasound beam was set at the far end of the region of interest so that a more uniform transmit pressure (200 to 400 kPa) could be maintained over depth in tissue. This guaranteed that all of the echoes form the UCA and the tissue in the region of interest were in a more uniform fashion, thus maximizing sensitivity over a wider depth.

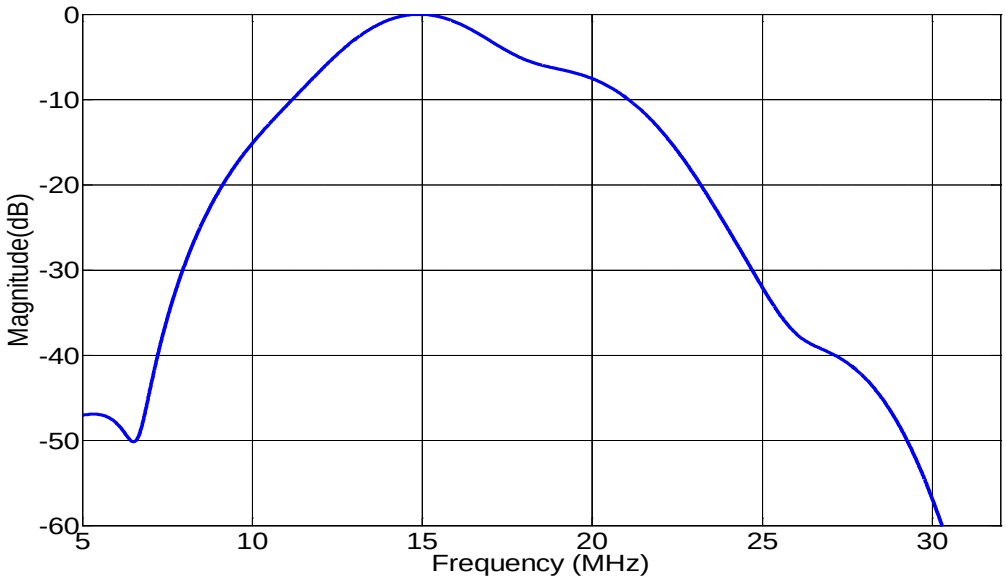

Figure 3.4. Frequency response of the linear array transducer measured with a flat steel plate.

In order to see the effect of the PI and the AM techniques on the S-D signal an experiment with a micron size wire phantom was implemented. The S-D signal enhanced by both PI and the AM modes was used for the SH imaging in a tissue mimicking phantom and a chicken embryo as an animal model. A scheme of the experimental setup depicted in figure 3.5.

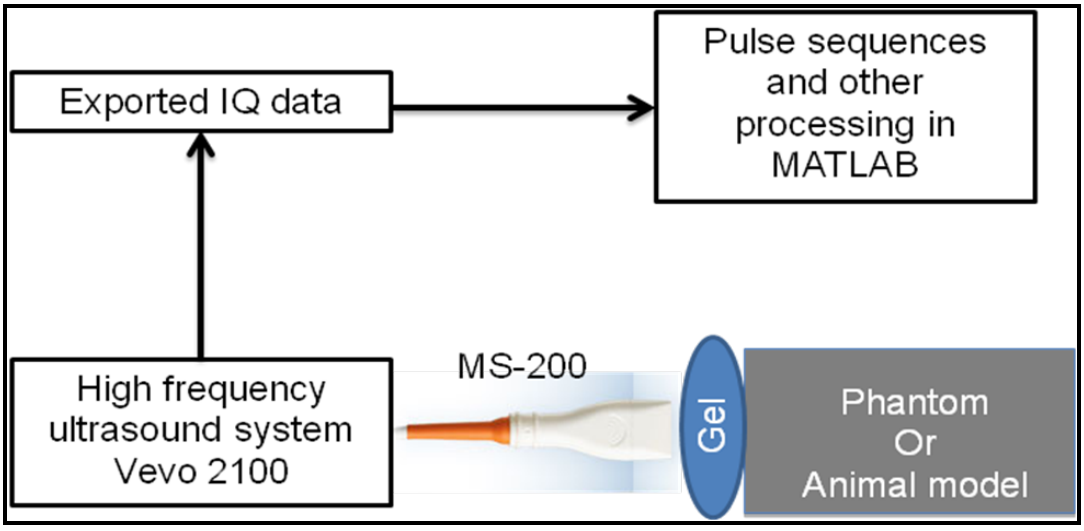

Figure 3.5. Summary of the experimental setup. Echoes are detected with the MS-200 array transducer and the I/Q sampled signals were exported from the Vevo 2100 and processed with MATLAB.

3.2.1. Wire phantom

In order to look at the propagated wave in different depths a wire phantom was made consisted of five tungsten wires with the diameter of 30 μm mounted in different depths (figure 3.6).

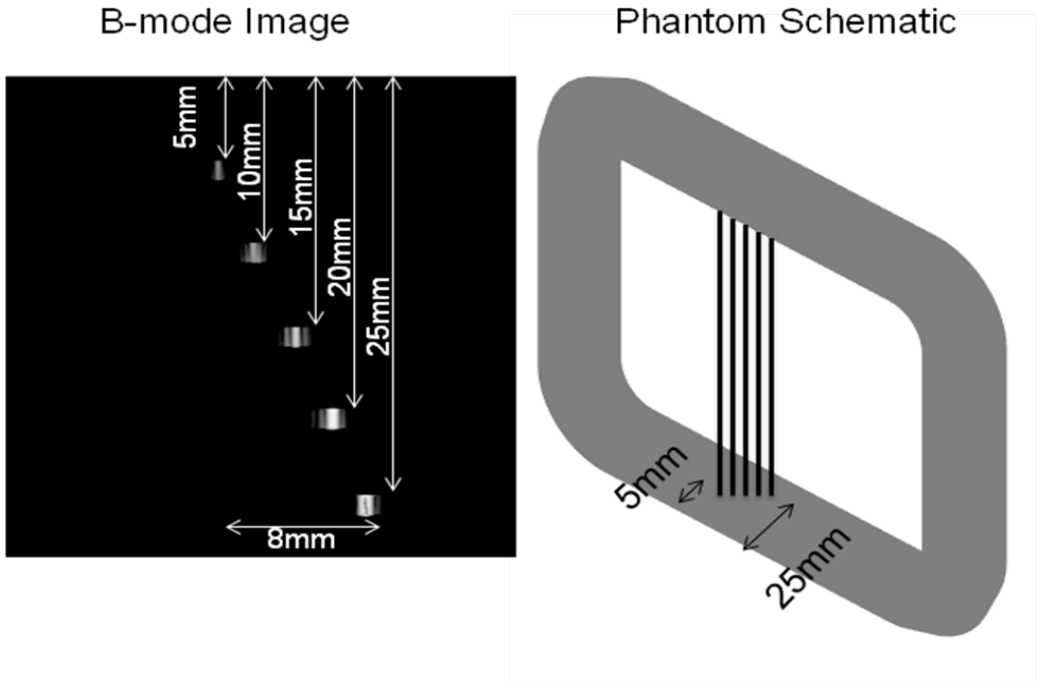

Figure 3.6. Wire phantom consist of five tungsten wires with 30 micrometer diameter in different depths: 5, 10, 15, 20 and 25 mm. Left images shows a gray scale image taken by the high frequency system (Vevo 2100) with a 20-cycle transmit pulse at 18 MHz. The right panel shows a schematic diagram of the phantom.

The reflected wave from the wires in different depths were recorded as it is summarized in figure 3.5.

3.2.2. In vitro experiment

A tissue mimicking phantom prepared (Teirlinck *et al.*, 1998). During the formation of the phantom a steel rod was placed in the phantom to make a cylindrical wall-less whole with a diameter of 10 mm in the phantom. A suspension of Micro-Marker was prepared as a 1:1000 dilution in saline after agent reconstitution. The microbubble solution was then poured into the wall-less whole inside the phantom. For making a homogeneous distribution of the UCA a magnetic steerer was used to mix the bubble solution gently. For each pulse sequence 15 image frames of the phantom in cross-section were acquired. I/Q data from low-amplitude (~300 kPa) narrowband 20-cycle transmit pulses with rectangular envelope were collected with the following pulse sequences: B-mode, PI and AM. The coupling between the probe and the phantom was done by an ultrasound gel. All measurements were made very quickly (5 minutes) and an appropriate receive processing for each of the pulse sequences was done in MATLAB. The regions of analysis were positioned within the UCA and tissue mimicking phantom, at the same image depth (figure 4.10). Fast Fourier transforms (FFTs) were applied to compare the levels of nonlinearity at the F and the SH frequencies as well as residual tissue signals. Guided by the FFT spectra, I/Q signals were digitally filtered around either the SH or the

F frequency bands using a band-pass Butterworth type 5 filter designed in MATLAB. The –40 dB stop-band ripple frequency cut-offs for the F and SH images 13 to 23 MHz and 4 to 14 MHz respectively. Next the CTR was determined for each image. For both the FFT and I/Q analysis, the results reflect an average of all 15 image frames collected. Six different images were compared in total; the SH and F images for the B-mode, PI-mode and AM-mode. Since a rectangular envelope was used for transmit pulse the S-D signal is supposed to be present in all the three different modes. The brightness in the gray scale images were normalized to one maximum value and the dynamic range of 30 was used for displaying the images. Dynamic range in ultrasound images refers to the range of echoes displayed by the ultrasound system, from strongest to weakest and it determines how many shades of gray are demonstrated in one image.

3.2.3. In vivo experiment

All animal work was performed in accordance with local ethical guidelines and approved animal care procedures. Fertilized eggs from White Leghorn chickens were obtained from a local hatchery (Drost Loosdrecht B.V., the Netherlands), and incubated at 37.8 C and 85% humidity in a brooder (Ehret, Emmendingen, Germany). The development of the chicken embryo takes 21 days and heart formation is complete after 14 days. Chick embryos were used for catheterization in vivo after 6 days of incubation (E6). The shell of the egg was broken in a water bath to prevent damaging the embryo and breaking the vessels. The embryo on the top of the egg yolk was kept in a water tank covering the whole egg. The microbubble injection was performed using a microinjection system (the Vevo Imaging Station, VisualSonics Inc., Toronto, Ontario, Canada). Bolus injections of $10\,\mu l$ of native MicroMarker contrast agent was administrated intra-venously. For visualization of the microbubbles, the MS200 transducer with a transmit frequency of 15 MHz was then mounted with a 30 degrees angle above the object. Having the heart and big vessels in the field of view was confirmed by means of a Doppler technique and the injection was conducted under guidance of a microscope.

3.3. Results

Figure 3.7 shows the echoes of a rectangular envelope 20-cycle transmit burst from the wires in different depths for three different modalities: B-mode, PI-mode and AM-mode. As it was explained earlier the B-mode single RF line consists of a single echo line while in the PI and AM mode it is made by 2 lines. In the PI-mode the second pulse is inverted and the echoes are then summed up and in the AM-mode the second pulse is twice the first one in amplitude then the first echo is multiplied by two and subtracted from the second echo.

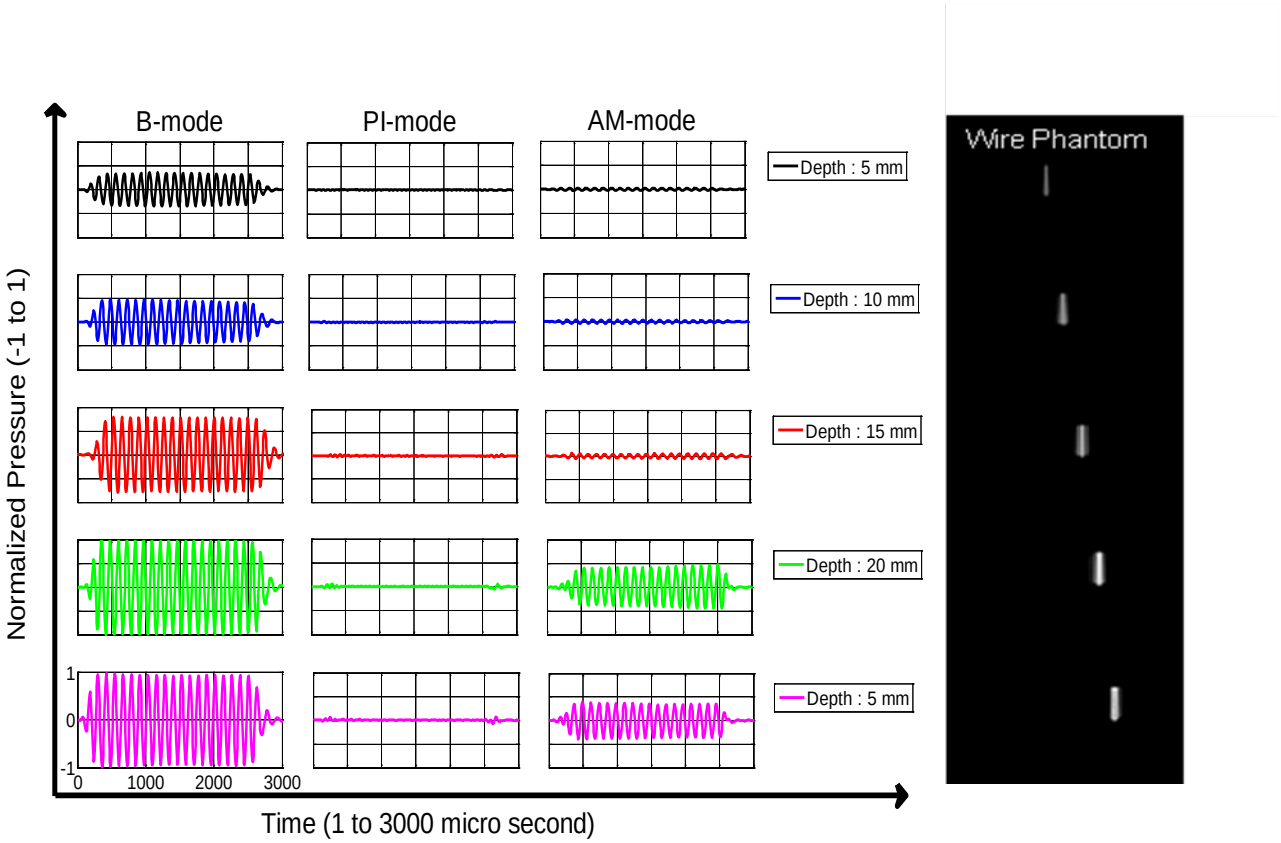

Figure 3.7. Single echo lines (RF signal) from 30 μm diameter wires in different depths and the gray scale image of the phantom.

Figure 3.8 shows the frequency spectra of the received echoes from the tissue-mimicking phantom (dashed) and UCA (solid) for the three different pulse sequences at 18 MHz. Figure 3.8 demonstrates how PI (blue) and AM(black) retain and even enhance the SH from the UCA, compared with the SH for the B-mode (red). Moreover tissue suppression and SH enhancement in general are more effective with PI.

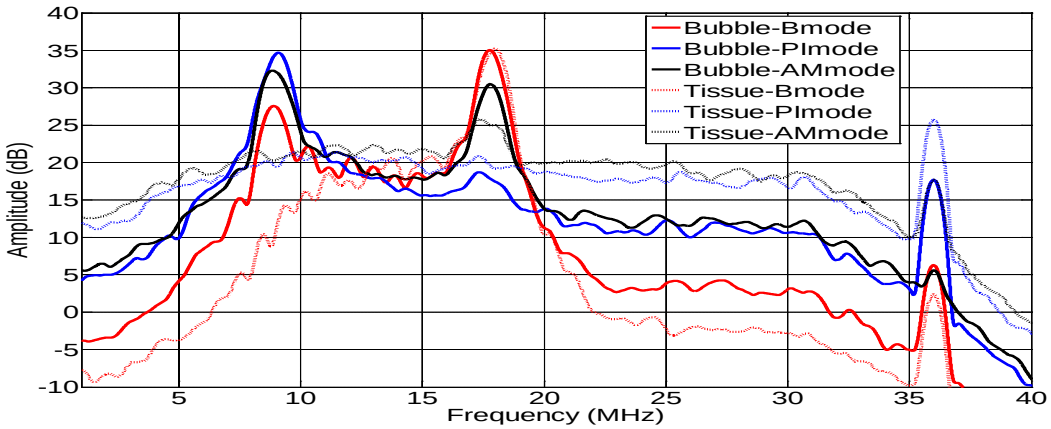

Figure 3.8. Frequency spectra of microbubble UCA (solid) and tissue-mimicking material (dashed) for the different pulse sequences. PI (blue), AM (black). The transmit frequency was 18 MHz.

The results of the in vitro study are presented in figure 3.10. The dynamic range for displaying all the images was set to 30 dB. Identical rectangular region of interest in the same depth, one in the tissue and one in the bubbles, were selected for CTR calculations. Figure 3.9 summarizes the in vitro results of CTR for all pulse sequences. The CTR enhancements at 18 MHz were 28 and 26 dB for the PI and the AM respectively.

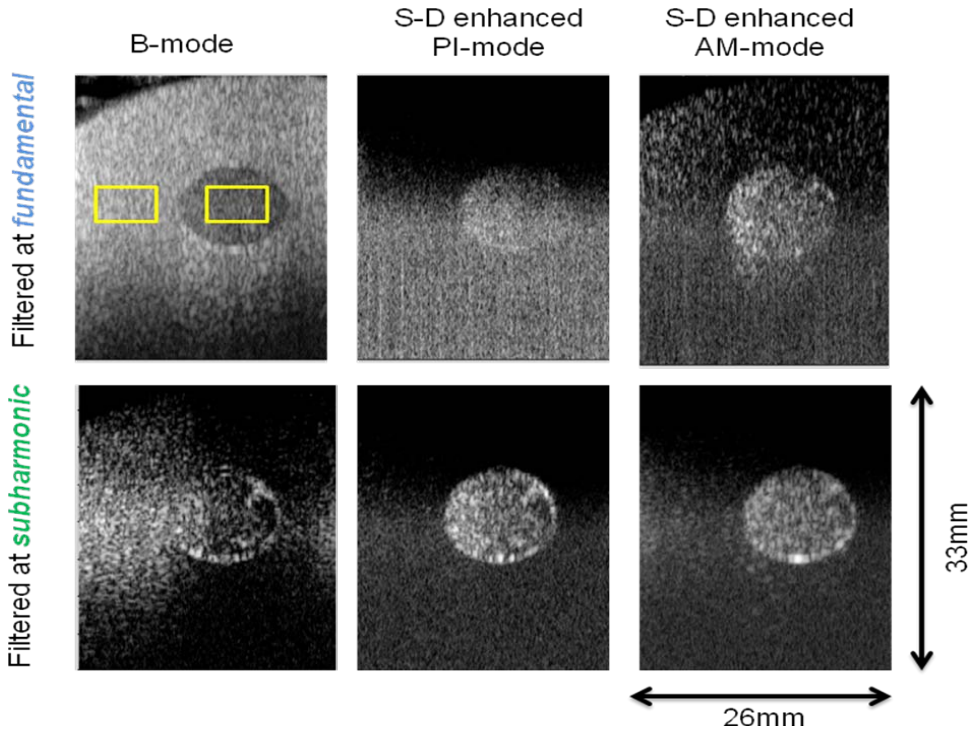

Figure 3.10. In vitro comparison between the F and the SH imaging in three different modalities: B-mode, PI-mode and Am-mode.

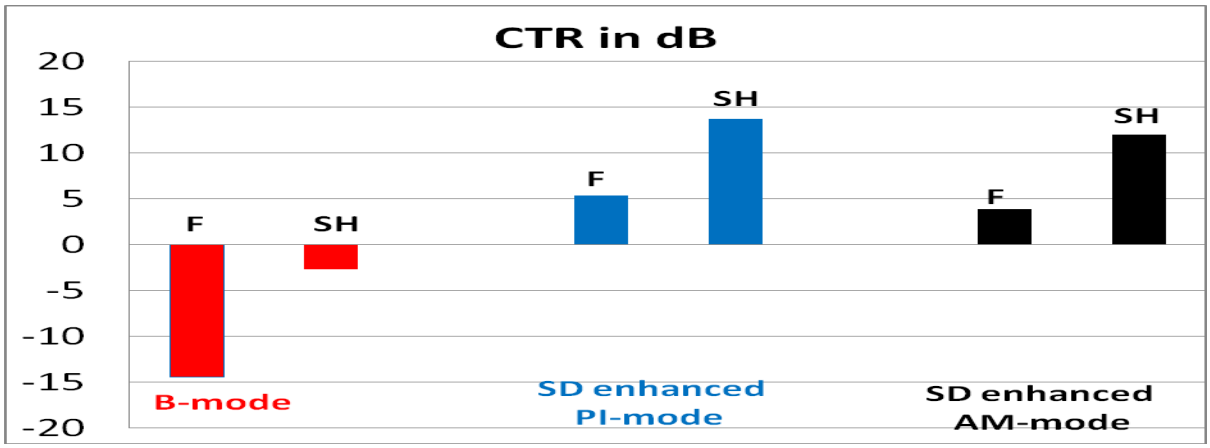

Figure 3.9. Summary of the in vitro results for F and SH imaging and different pulse sequences (B-mode, blue; PI, red; AM, black). The largest improvements in the CTR in regard to the F B-mode image were observed for SH bandpass filter with PI (28 dB) and AM (26dB).

Since the PI technique turned out to give the maximum enhancement in the CTR, only the result of this pulse sequence on the chicken embryo model is demonstrated in figure 3.11.

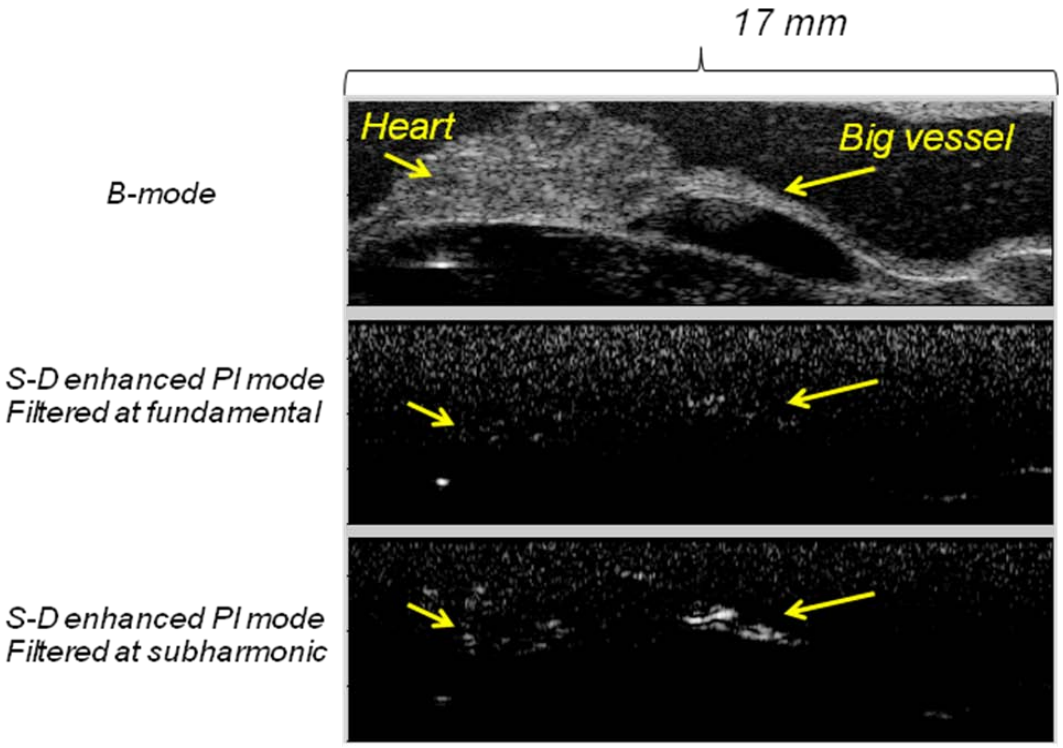

Figure 3.11. In vivo comparison between the F and the SH imaging in the PI-mode

3.4. Discussion

3.4.1 Self-demodulation enhancement

In most of the high frequency systems such a quadratic relations between the S-D signal and the transmit signal is not exactly correct because of the high transmit pressures used in order to increase the penetration depths. In such cases the PI could be a better option for doubling the S-D signal compared to AM method since both of the transmit pulses have the same amplitude but different phases in the PI mode. As it was shown in figure 3.7 the echoes from the wires close to the transducers in both AM and PI mode are similar and both of these methods could reduce the linear F echoes from the wire. Close to the transducer the S-D signal is not developed yet and it is not present in the echo signals. However looking at the echoes from the deeper wires at the focus of the transducer shows that when the transmit pressure is high the AM method reaches a saturation level where its performance in reducing the linear part of the signal degrades compared to the PI. The reason is that in such a high transmit pressure doubling transmit pressure does not result in doubling the actual pressure at the focus of the transducer and the pressure saturates. Therefore doubling the first echo and subtracting it from the

second one keeps part of the linear F echo. On the other hand in PI method the same pressures are transmitted and the second pulse is only inverted. The S-D signal can be clearly seen in the echoes from the deeper wires in the PI-mode while it is lost in the residual of the F signal in the AM mode (note that the amplitude of the S-D signal is 60 dB lower than the amplitude at F). According to the result of the single element study in chapter 2 such a low amplitude SD signal can enhance the SH emission from the UCA.

3.4.2 Scattering from UCA

Figure 3.8 compares the spectrum of the backscattered signal from tissue and the UCA for different modalities used in this study: B-mode, PI-mode and AM-mode. As we expect from the wire phantom the PI technique seems to be more successful in reducing the linear F echo both from the tissue and the UCA while keeping the nonlinear terms (The SH and second harmonic signals) in comparison to the AM technique. The other interesting point in this figure is the level of the SH signal for different modalities. All the three methods can provide a distinguishable peak at the SH in the spectrum. However the PI and AM method give the most enhancement in the SH emission from the UCA respectively compared to the SH signal in the B-mode. Such a behavior can be explained by the effect of the SD signal on the SH emission from UCA (chapter 2). Since in such a the PI and AM techniques have higher SD signal they can stimulate the SH emission of the UCA more efficiently than in the B-mode.

3.4.3 Imaging validation

Both the in vitro and in vivo results (figures 3.9, 3.10 and 3.11) confirm that the SH imaging using the stimulation effect of the SD signal can increase the CTR compared to the contrast F imaging. Figure 3.9 shows that the SH imaging in all the three different modalities can enhance the CTR. Looking at the CTR for each modality separately, the highest increase in CTR takes place for the B-mode since the F imaging in the B-mode contains lots of strong backscatter echoes from the tissue while they are cancelled to a large extend in both PI and AM methods. The SH imaging in the PI and AM modes results in higher CTR than in the B-mode. That is mostly because of the doubling effect of the SD signals in those modalities since the tissue does not produce any signals at the SH frequency. In total the maximum improvement in the CTR compared to the B-mode images happens in the PI-mode and AM-mode having the values of 28 and 26 dB respectivly. Based on the phantom characterization the gray scale images are all normalized to one maximum value and then presented using the dynamic range of 30 dB. This way the brightness can be directly compared between the different images. In figure 3.10 we can see that the B-mode image filtered at the F frequency contains both the nonlinear echoes from the UCA and the linear echoes from the tissue mimicking phantom while in both the PI-mode and AM-mode these linear echoes have been cancelled. Due to relatively low transmit pressure in the region of interest both the PI and AM methods very well remove the linear echoes from the tissue mimicking phantom.

Second row of the figure 3.10 shows the filtered images at the SH frequency for B-mode, PI-mode and AM-mode. The CTR in the B-mode images is lower than both in the PI and

AM modes since the SD signals are doubled using the PI and AM method. Therefore SH emission is stimulated more effectively. Finally since the region of interest is out of the focal area, there is no significant difference in CTR between the PI-mode and AM-mode. This result is in agreement with the pulse echo measurement using the wire phantom (figure 3.7).

Results of the in vitro study suggest that the SD enhanced PI mode is the best candidate with the maximum improvement in the CTR for contrast imaging. Therefore only this method was tested in vivo. Figure 3.11 shows that the signals from the UCA are so weak in the B-mode image and almost lost in the tissue signal. On the other hand the F image in the PI-mode reduces the signals from the tissue but also does not provide enough CTR. However the SH image clearly shows a better image with higher CTR. The UCA circulating in the heart and the big vessel are nicely visualized while the linear echoes from the tissue and the body of the embryo are canceled. These differences in the F and SH images in vivo might be due to the different experimental environment. The amount of microbubbles in the field of view is much less in vivo compared to in vitro situation. Also the hydrostatic pressure which seems to have an impact on the SH emission is different in these two experiments.

One of the problems of using the SD enhanced PI method for SH imaging is the linear backscatter of the SD signal itself by the tissue since its frequency content is close to the SH frequency for transmit pulse with rectangular envelope. However, the very low amplitude of the SD signal in the low transmit pressures (40 dB below the amplitude at the F frequency at its maximum) can guarantee that the linear backscatter of such a weak signal does not have a big impact on the final CTR in the images. It might also be possible to apply some signal processing techniques or even using a new pulse sequences to reduce the linear back scatter of the SD signal for higher transmit pressures. For instance subtracting the two transmit pulse in the PI mode instead of the summation, results in cancelation of the SD signal while part of the SH can still be kept due to the phase dependency nature of SH emission. Also other harmonics of the SH signal such as ultraharmonic can be used for imaging.

3.5. Conclusion

After analyzing the effect of the SD signal on the SH stimulation in chapter 2, a real time nonlinear contrast imaging with an array based high frequency ultrasound system was demonstrated in this chapter. Such a new nonlinear contrast detection method offers improved performance over a larger depth and a better CTR at high frequencies compared to with the conventional linear and nonlinear contrast methods.

4 Conclusion and future work

In this chapter a summary of this thesis, a trend for further investigations in future, some limitations of the newly developed technique, introduced in this work, as well as potential solutions for those limitations, are presented. Similar to the SH emission the ultraharmonic response of the microbubbles as an another unique behavior of the UCA is introduced. The primary numerical simulation results presenting in this chapter, suggest another promising method for improving the contrast detection techniques. How our new contrast detection method based on the SH signal can help in the field of targeted imaging is the subject of the last part of this chapter.

4.1. Summary

A description of sound propagation through a fluid medium was derived considering a set of assumptions. The nonlinear behavior of the traveling sound beam was briefly reviewed and the KZK model was introduced as a model equation capable of predicting nonlinear phenomenon such as the S-D signal. The numerical solution was driven for the S-D signal according to the KZK model. In the next step the response of a ultrasound pulse to a sphere object within the fluid medium was considered. The scattered pressure wave was illustrated by the object's time-varying volume. Limiting the radial oscillation to small-amplitudes, the microbubble was presented as a forced, damped oscillator characterised by damping constants and a resonance frequency. The SH signal, unique to microbubbles, was explained to be preferentially produced for excitations at twice the microbubbles resonance frequency. As the shell changes the behavior of the microbubble, two different mathematical models by de Jong (de Jong N et al., 1994) and Marmottant (Marmottant et al., 2005) for the microbubble including the shell properties was introduced, and references were suggested for the other models.

Developing a new method for detecting the UCA at high frequency while reducing the backscattered signal from the soft tissue as a pre-requirement of targeted imaging was the overarching goal of this thesis. To that end, the subharmonic response of the microbubbles was enhanced by mean of the S-D signal. Based on the single element investigation, optimizing the shape of the transmit pulse (having a rectangular shape rather than Gaussian) can place the frequency content of the S-D signal closer to the SH frequency which in turn increases this nonlinear oscillation of the UCA up to 20 dB (figure2.4). These results were supported by results of numerical simulations.

The new contrast detection method developed in chapter 2 was then implemented in a pre-clinical high frequency ultrasound system (Vevo 2100, VisualSonics Inc., Toronto, ON, Canada) to be examined in real life situation. A wire phantom was used to see the propagated wave in different depth in water for three different modes: B-mode, PI-mode and AM-mode (figure3.6). A region of interest was placed in the UCA area and tissue area in the same depths for CTR calculation. Both the SH images with PI and AM techniques resulted in large CTR improvements (28 and 26 dB respectively) compare to

the F B-mode image. The PI method was the best candidate for the nonlinear imaging at high frequencies with high transmit pressures providing the maximum CTR in the SH imaging. And finally this technique was tested in a chicken embryo as a animal model.

4.2. Future work

Although this work suggested a new method for detecting the UCA at high frequency ultrasound using the enhanced SH oscillations of microbubbles by optimizing the shape of the excitation pulse, there are still some limitations in such a techniques. On the other hand this new technique was developed as a pre-requirement tool for going into a more sophisticated world which is targeted imaging using the targeted microbubbles. Therefore improvement and solving the limitation of the newly developed nonlinear imaging method and applying it to the targeted imaging applications will be the headlines of the future work.

4.2.1 Limitations and solutions

One of the main limitations of the technique we discussed during this work is the linear backscatter echo of the S-D signal itself from the tissue. Even though the amplitude of the S-D wave is very lower than the amplitude of the signal at the F frequency (about 60 dB) it might still reduce the CTR in deeper region of interest at high transmit pressures and high frequencies due to the week SH signal. One solution for such a problem might to process the echo signals in the PI method differently. Since the stimulation effect of the S-D signal is a phase dependent phenomenon inverting the transmit pulse cause phase shifting in the SH stimulation and therefore SH emission form the microbubble. Therefore subtracting the received echo in the PI mode instead of the summation (let's call it subtracted PI) can keep the SH oscillation. Obviously such a method cannot remove the linear fundamental part of the backscatter signal, since this part is independent of the stimulation effect of the S-D wave, but this method can still be used for SH imaging since the F content of the echoes are filtered out for SH imaging. In order to briefly study such a hypothesis a simulation using the linked KZK and Marmattant model similar to the one in chapter two was implemented to predict the reaction of a single bubble having a radius of $R_0 = 1 \quad \mu m$ and $\sigma = 0.0099 \quad N/M$ to 10 MHz 20-cycle pulses at the focus of the single element transducer with a rectangular envelope and a pressure of 50 kPa. Figure 4.1 shows the spectra of the scattered signal from the microbubble in response to two different methods: the PI method and the method which we call subtracted PI. Even though the F component in the subtracted PI method is not cancelled as it is in the conventional PI mode the level of the SH component seems to stay similar which is a good news for SH imaging using the subtracted PI method to minimize the linear backscatter of the S-D signal and increase the CTR. Further investigations and carefully designed experiments are needed to confirm this simulation result and to develop a practical approach for imaging.

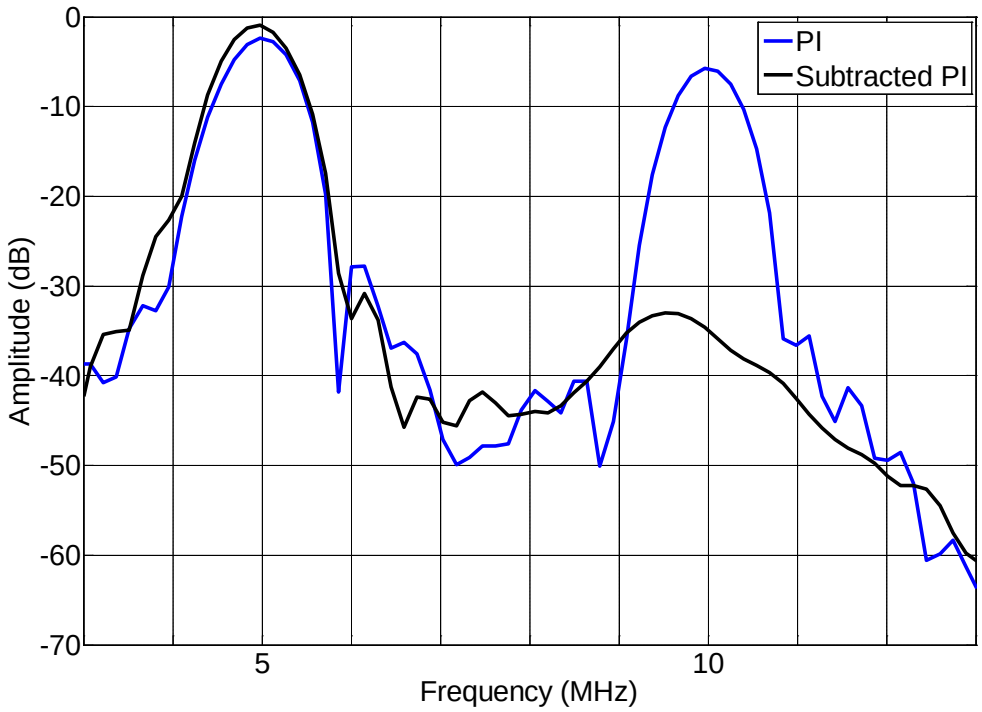

Figure 2.5. Simulation results showing the Fourier transform of the scattered signal from a single microbubble and 20-cycle, 50 kPa pulses in two different methods: PI and subtracted PI ($R = 1 \quad \mu m, \quad \sigma = 0.0099 \quad N / M$).

Another solution which does not change the signal processing part of the imaging is to look at the ultraharmonic (UH) emission of the UCA instead of the SH response. According to the simulation result in (figure 4.2) the stimulation effect of the S-D wave on the UH emission of the microbubble is as effective as for the SH emission. In the other word the same 20 dB enhancement in the UH response of the microbubble can be achieved by the mean of the S-D signal as it was for the SH response. Using the UH harmonic imaging instead of the SH imaging has the advantage of lower direct reflection of the S-D signal itself, however such a method has its own limitations and problems which needs more and accurate investigations.

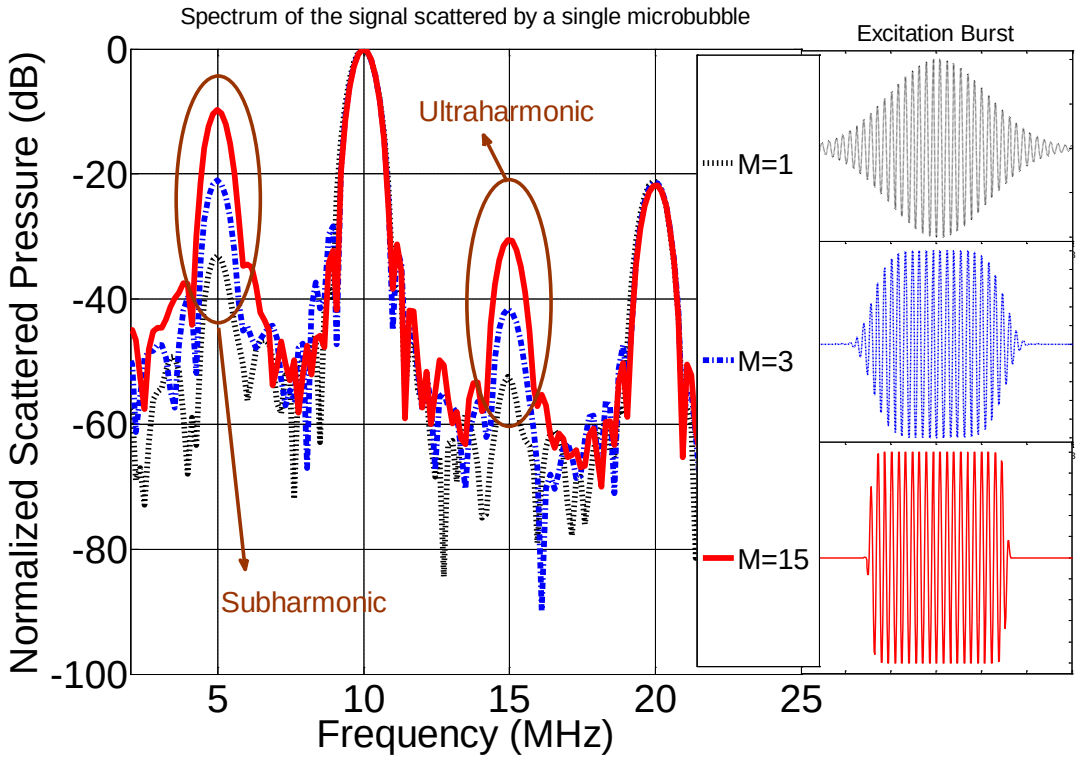

Figure 2.5. Simulation results showing the Fourier transform of the scattered signal from a single microbubble and 20-cycle, 50 kPa pulses with three different envelopes used as excitation bursts. We can see the same enhancement for the UH response and SH due to the stimulation effect of the S-D signal ($R = 1 \quad \mu m, \quad \sigma = 0.0099 \quad N/M$).

Both of the solution suggested here seem to improve the method, however further investigation and experiments are needed to confirm these simulation results.

4.2.2 Targeted imaging

The attachment of targeting ligands to the microbubble shell enables an accumulation of the UCA at the target site selectively. However, to the best of our knowledge, there is still no optimized method to distinguish between the attached bubbles from the free moving ones by using the differences in their nonlinear signals. The method which is normally used for targeted image is to wait for the free bubbles to be washed out of the region of interest and then image only the remaining bubbles which supposed to be the targeted UCA. Such a method, despite of being very time consuming, is hampered by artifacts such as motion and the uncertainty of the ultrasound echoes in each frames. Recently, Brandon et al reported that there is a significant differences in the SH response of a bound microbubble and a free moving one (Brandon Helfield *et al.*, 2010). They studied a size-per-size comparison of the acoustic nonlinear response of individual streptavidin-coated MicroMarker microbubbles bound to a compliant agarose-biotin gel

surface. The size of bubbles were optically measured and then insonified at 25 MHz over a range of pressures. Such a difference in the SH emission can be used together with the method we explained in this work to develop a real time imaging technique for targeted microbubbles by using the differences in the SH response of bound and unbound bubbles.

References

ALLEN, J. S. & RASHID, M. M. 2004. Dynamics of a Hyperelastic Gas-Filled Spherical Shell in a Viscous Fluid. *Journal of Applied Mechanics,* 71**,** 195-200.

AVERKIOU, M. A., LEE, Y.-S. & HAMILTON, M. F. 1993. Self-demodulation of amplitude- and frequency-modulated pulses in a thermoviscous fluid. *The Journal of the Acoustical Society of America,* 94**,** 2876-2883.

AVERKIOU, M. A., ROUNDHILL, D. N. & POWERS, J. E. A new imaging technique based on the nonlinear properties of tissues. IEEE Ultrasonics Symposium, 5-8 Oct 1997 1997. 1561-1566 vol.2.

BAILEY, M. R., COURET, L. N., SAPOZHNIKOV, O. A., KHOKHLOVA, V. A., TER HAAR, G., VAEZY, S., SHI, X., MARTIN, R. & CRUM, L. A. 2001. Use of overpressure to assess the role of bubbles in focused ultrasound lesion shape in vitro. *Ultrasound in medicine & biology,* 27**,** 695-708.

BALDASSARRE, D., AMATO, M., BONDIOLI, A., SIRTORI, C. R. & TREMOLI, E. 2000. Carotid artery intima-media thickness measured by ultrasonography in normal clinical practice correlates well with atherosclerosis risk factors. *Stroke; a journal of cerebral circulation,* 31**,** 2426-30.

BARGER, A. C., BEEUWKES, R., 3RD, LAINEY, L. L. & SILVERMAN, K. J. 1984. Hypothesis: vasa vasorum and neovascularization of human coronary arteries. A possible role in the pathophysiology of atherosclerosis. *The New England journal of medicine,* 310**,** 175-7.

BARNETT STANLEY B, TER HAAR GAIL R, ZISKIN MARVIN C, ROTT HANS-DIETER, DUCK FRANCIS A & KAZUO., M. 2000. International recommendations and guidelines for the safe use of diagnostic ultrasound in medicine. *Ultrasound in medicine & biology,* 26**,** 355-366.

BERKTAY, H. O. 1965. Possible exploitation of non-linear acoustics in underwater transmitting applications. *Journal of Sound and Vibration,* 2**,** 435-461.

BIAGI, E., BRESCHI, L., VANNACCI, E. & MASOTTI, L. 2006. Subharmonic emissions from microbubbles: effect of the driving pulse shape. *IEEE transactions on ultrasonics, ferroelectrics, and frequency control,* 53**,** 2174-82.

BLOCH SH, DAYTON PA & KW., F. 2004. Targeted imaging using ultrasound contrast agents: progress and opportunities for clinical and research applications. *IEEE Eng Med Bio Mag 2004:18-29.*

BLOMLEY, M., CLAUDON, M. & COSGROVE, D. 2007. WFUMB Safety Symposium on Ultrasound Contrast Agents: clinical applications and safety concerns. *Ultrasound in medicine & biology,* 33**,** 180-6.

BOUAKAZ, A. & DE JONG, N. 2007. WFUMB Safety Symposium on Echo-Contrast Agents: nature and types of ultrasound contrast agents. *Ultrasound in medicine & biology,* 33**,** 187-96.

BRANDON HELFIELD, EMMANUEL CHERIN & GOERTZ, A. D. 2010. Subharmonic behavior of targeted and untargeted lipid encapsulated microbubbles at high ultrasound frequencies. *Journal of the Acoustical Society of America,* 128.

BROCK-FISHER G, POLAND M & RAFTER P 1996. Means for increasing sensitivity in nonlinear ultrasound imaging systems. *US Patent No. 5,577,505*.

BROWN, J. A., FOSTER, F. S., NEEDLES, A., CHERIN, E. & LOCKWOOD, G. R. 2007. Fabrication and Performance of a 40-MHz Linear Array Based on a 1-3 Composite with Geometric Elevation Focusing. *Ultrasonics, Ferroelectrics and Frequency Control, IEEE Transactions on,* 54**,** 1888-1894.

BURNS, P. N. 1996. Harmonic imaging with ultrasound contrast agents. *Clinical radiology,* 51 Suppl 1**,** 50-5.

CARDIOVASCULAR SALES 2011. *http://www.cvsales.com/cvs/PartsProbes/AcusonProbes.aspx*.

CHANG P H, S. K. K., WU S & B, L. H. 1995. Second harmonic imaging and harmonic Doppler measurements with Albunex. *IEEE Trans. Ultrason. Ferroelectr. Freq. Control,* 42**,** 1020.

CHATTERJEE, D. & SARKAR, K. 2003. A Newtonian rheological model for the interface of microbubble contrast agents. *Ultrasound in medicine & biology,* 29**,** 1749-57.

CHAUSSY, C., SCHMIEDT, E., JOCHAM, D., BRENDEL, W., FORSSMANN, B. & WALTHER, V. 2002. First clinical experience with extracorporeally induced destruction of kidney stones by shock waves. 1981. *The Journal of urology,* 167**,** 1957-60.

CHE-CHOU, S. & PAI-CHI, L. 2001. Harmonic leakage and image quality degradation in tissue harmonic imaging. *Ultrasonics, Ferroelectrics and Frequency Control, IEEE Transactions on,* 48**,** 728-736.

CHOMAS J, D. P., MAY D & K, F. 2002. Nondestructive subharmonic imaging. *IEEE Trans. Ultrason. Ferroelectr. Freq. Control,* 49**,** 883.

CHRISTOPHER, T. 1997. Finite amplitude distortion-based inhomogeneous pulse echo ultrasonic imaging. *Ultrasonics, Ferroelectrics and Frequency Control, IEEE Transactions on,* 44**,** 125-139.

CHURCH, C. C. 1995. The effects of an elastic solid surface layer on the radial pulsations of gas bubbles. *The Journal of the Acoustical Society of America,* 97**,** 1510-1521.

COLI, S., MAGNONI, M., SANGIORGI, G., MARROCCO-TRISCHITTA, M. M., MELISURGO, G., MAURIELLO, A., SPAGNOLI, L., CHIESA, R., CIANFLONE, D. & MASERI, A. 2008. Contrast-enhanced ultrasound imaging of intraplaque neovascularization in carotid arteries: correlation with histology and plaque echogenicity. *Journal of the American College of Cardiology,* 52**,** 223-30.

COSGROVE, D. 2006. Ultrasound contrast agents: an overview. *European journal of radiology,* 60**,** 324-30.

DAYTON, P. A. & FERRARA, K. W. 2002. Targeted imaging using ultrasound. *Journal of magnetic resonance imaging : JMRI,* 16**,** 362-77.

DE JONG, N. 1996. Improvements in ultrasound contrast agents. *Engineering in Medicine and Biology Magazine, IEEE,* 15**,** 72-82.

DE JONG N, CORNET R & T., L. C. 1994. Higher harmonics of vibrating gas-filled microspheres. Part one: simulations. *Ultrasonics,* 32**,** 447-453.

DE JONG N, B. A. & P, F. 2002. Basic acoustic properties of microbubbles. *Echocardiography,* 19**,** 229.

DE JONG, N., FRINKING, P. J., BOUAKAZ, A. & TEN CATE, F. J. 2000. Detection procedures of ultrasound contrast agents. *Ultrasonics,* 38**,** 87-92.

DE JONG, N. & HOFF, L. 1993. Ultrasound scattering properties of Albunex microspheres. *Ultrasonics,* 31**,** 175-181.

DEN DEKKER, A. J. & VAN DEN BOS, A. 1997. Resolution: a survey. *J. Opt. Soc. Am. A,* 14**,** 547-557.

DENG, C. X. & LIZZI, F. L. 2002. A review of physical phenomena associated with ultrasonic contrast agents and illustrative clinical applications. *Ultrasound in medicine & biology,* 28**,** 277-86.

DESSER, T. S. & JEFFREY, R. B. 2001. Tissue harmonic imaging techniques: physical principles and clinical applications. *Seminars in ultrasound, CT, and MR,* 22**,** 1-10.

DOINIKOV, A. A. & DAYTON, P. A. 2007. Maxwell rheological model for lipid-shelled ultrasound microbubble contrast agents. *The Journal of the Acoustical Society of America,* 121**,** 3331-40.

DOLAN, M. S., GALA, S. S., DODLA, S., ABDELMONEIM, S. S., XIE, F., CLOUTIER, D., BIERIG, M., MULVAGH, S. L., PORTER, T. R. & LABOVITZ, A. J. 2009. Safety and efficacy of commercially available ultrasound contrast agents for rest and stress echocardiography a multicenter experience. *Journal of the American College of Cardiology,* 53**,** 32-8.

DUCK F A, BAKER A C & STARRITT H C 1998. Ultrasound in medicine. . *Institute of Physics Publishing, Bristol, Philadelphia, PA.*

EATOCK, B. C., NISHI, R. Y. & JOHNSTON, G. W. 1985. Numerical studies of the spectrum of low-intensity ultrasound scattered by bubbles. *The Journal of the Acoustical Society of America,* 77**,** 1692-1701.

ECKERSLEY, R. J., CHIN, C. T. & BURNS, P. N. 2005. Optimising phase and amplitude modulation schemes for imaging microbubble contrast agents at low acoustic power. *Ultrasound in medicine & biology,* 31**,** 213-9.

ELIASZIW, M., RANKIN, R. N., FOX, A. J., HAYNES, R. B. & BARNETT, H. J. 1995. Accuracy and prognostic consequences of ultrasonography in identifying severe carotid artery stenosis. North American Symptomatic Carotid Endarterectomy Trial (NASCET) Group. *Stroke; a journal of cerebral circulation,* 26**,** 1747-52.

ELLER A & FLYNN H 1969. Generation of subharmonics of order one-half by bubbles in a sound field. *J. Acoust. Soc. Am.,* 46**,** 722.

EMMER, M. 2009. *The onset of bubble vibration.* PhD, Erasmus medical center.

FAEZ, T., EMMER, M., DOCTER, M., SIJL, J., VERSLUIS, M. & DE JONG, N. 2011. Characterizing the subharmonic response of phospholipid-coated microbubbles for carotid imaging. *Ultrasound in medicine & biology,* 37**,** 958-70.

FEINSTEIN, S. B. 2006. Contrast ultrasound imaging of the carotid artery vasa vasorum and atherosclerotic plaque neovascularization. *Journal of the American College of Cardiology,* 48**,** 236-43.

FERRARA, N. & KERBEL, R. S. 2005. Angiogenesis as a therapeutic target. *Nature,* 438**,** 967-974.

FORSBERG, F., SHI, W. T. & GOLDBERG, B. B. 2000. Subharmonic imaging of contrast agents. *Ultrasonics,* 38**,** 93-8.

FOSTER, F. S., BURNS, P. N., SIMPSON, D. H., WILSON, S. R., CHRISTOPHER, D. A. & GOERTZ, D. E. 2000. Ultrasound for the visualization and quantification of tumor microcirculation. *Cancer metastasis reviews,* 19**,** 131-8.

FRIGG R P, H. S. 2006. Models in science. . *Stanford Encyclopedia of Philosophy, http://plato.stanford.edu/entries/models-science/.* .

FROYSA, K. E., TJOTTA, J. N. & TJOTTA, S. 1993. Linear propagation of a pulsed sound beam from a plane or focusing source. *The Journal of the Acoustical Society of America ISSN 0001-4966 CODEN JASMAN,* 93**,** 80-92.

GOERTZ D E, F. M. E., DE JONG N & F, V. D. S. A. 2006. Nonlinear intravascular ultrasound contrast imaging. *Ultrasound Med. Biol.,* 32**,** 491.

GOERTZ DE, DE JONG N & AFW., V. D. S. 2007. Modeling high frequency nonlinear scattering from lipid encapsulated microbubble contrast agents.

. *Proc IEEE Ultrason Symp* .

GOERTZ DE & WONG SWS 2001. Nonlinear scattering properties of microbubble contrast agents at high frequencies. *Proc IEEE Ultrason Symp***,** 4.

GOERTZ, D. E., CHERIN, E., NEEDLES, A., KARSHAFIAN, R., BROWN, A. S., BURNS, P. N. & FOSTER, F. S. 2005. High frequency nonlinear B-scan imaging of microbubble contrast agents. *IEEE transactions on ultrasonics, ferroelectrics, and frequency control,* 52**,** 65-79.

GOLDBERG B B, RAICHLEN J S & FORSBERG F 2001. Ultrasound Contrast Agents, Basic principles and clinical applications, 2nd edition. . *Martin Dunitz, London.*

GOLDBERG, B. B., LIU, J. B. & FORSBERG, F. 1994. Ultrasound contrast agents: a review. *Ultrasound in medicine & biology,* 20**,** 319-33.

GOSSL, M., ROSOL, M., MALYAR, N. M., FITZPATRICK, L. A., BEIGHLEY, P. E., ZAMIR, M. & RITMAN, E. L. 2003. Functional anatomy and hemodynamic characteristics of vasa vasorum in the walls of porcine coronary arteries. *The anatomical record. Part A, Discoveries in molecular, cellular, and evolutionary biology,* 272**,** 526-37.

GRAMIAK, R. & SHAH, P. M. 1968. Echocardiography of the aortic root. *Investigative radiology,* 3**,** 356-66.

GRAMIAK, R., SHAH, P. M. & KRAMER, D. H. 1969. Ultrasound cardiography: contrast studies in anatomy and function. *Radiology,* 92**,** 939-48.

HAMILTON, F. & BLACKSTOCK, D. T. 1998. *Nonlinear acoustics*.

HOFF, L., SONTUM, P. C. & HOVEM, J. M. 2000. Oscillations of polymeric microbubbles: effect of the encapsulating shell. *The Journal of the Acoustical Society of America,* 107**,** 2272-80.

HOSOKAWA A & OTANI T 1997. Ultrasonic wave propagation in bovine trabecular bone. *J. Acoust. Soc. Am. 101, 558–562.*

HUGHES, E. R., LEIGHTON, T. G., PETLEY, G. W. & WHITE, P. R. 1999. Ultrasonic propagation in cancellous bone: a new stratified model. *Ultrasound in medicine & biology,* 25**,** 811-21.

HUGHES, E. R., LEIGHTON, T. G., PETLEY, G. W., WHITE, P. R. & CHIVERS, R. C. 2003. Estimation of critical and viscous frequencies for Biot theory in cancellous bone. *Ultrasonics,* 41**,** 365-8.

KAUL, S. 2008. Myocardial contrast echocardiography: a 25-year retrospective. *Circulation,* 118**,** 291-308.

KHISMATULLIN, D. B. 2004. Resonance frequency of microbubbles: effect of viscosity. *The Journal of the Acoustical Society of America,* 116**,** 1463-73.

KHISMATULLIN, D. B. & NADIM, A. 2002. Radial oscillations of encapsulated microbubbles in viscoelastic liquids. *Physics of Fluids,* 14**,** 3534-3557.

KLIBANOV, A. L. 2005. Ligand-carrying gas-filled microbubbles: ultrasound contrast agents for targeted molecular imaging. *Bioconjugate chemistry,* 16**,** 9-17.

KLIBANOV, A. L. 2007. Ultrasound molecular imaging with targeted microbubble contrast agents. *Journal of nuclear cardiology : official publication of the American Society of Nuclear Cardiology,* 14**,** 876-84.

KRISHNA P D, S. P. M. & L, N. V. 1999. Subharmonic generation from ultrasonic contrast agents. *Phys. Med. Biol.,* 44**,** 681.

KUZNETSOV V P 1971. Equation of nonlinear acoustics *Sov. Phys. Acoust.,* 16**,** 467-470.

LANDAU LD & LIFSCHITZ EM 1987. Fluid Mechanics. *Trans. Sykes JB, Reid WH. Oxford: Pergamon.*

LANGTON C M, PALMER S B & PORTER R W 1984. The measurement of broadband ultrasonic attenuation in trabecular bone. . *Eng. Med. 13 (2), 89–91.*

LEE, K. I., ROH, H. S. & YOON, S. W. 2003. Acoustic wave propagation in bovine cancellous bone: application of the Modified Biot-Attenborough model. *The Journal of the Acoustical Society of America,* 114**,** 2284-93.

LEIGHTON, T. G. 1994. *The acoustic bubble.Academic Press Limited, London.*

LEONG-POI H 2009. Molecular imaging using contrast-enhanced ultrasound: evaluation of angiogenesis and cell therapy. *Cardiovasc Res. 2009 Nov 1;84(2):190-200. Epub 2009 Jul 22.*

LI, P. C. & SHEN, C. C. 1999. Effects of transmit focusing on finite amplitude distortion based second harmonic generation. *Ultrasonic imaging,* 21**,** 243-58.

LIN, W., QIN, Y. X. & RUBIN, C. 2001. Ultrasonic wave propagation in trabecular bone predicted by the stratified model. *Annals of biomedical engineering,* 29**,** 781-90.

LINDNER, J. R., SONG, J., JAYAWEERA, A. R., SKLENAR, J. & KAUL, S. 2002. Microvascular rheology of Definity microbubbles after intra-arterial and intravenous administration. *Journal of the American Society of Echocardiography : official publication of the American Society of Echocardiography,* 15**,** 396-403.

LOCKWOOD, G. R., RYAN, L. K., HUNT, J. W. & FOSTER, F. S. 1991. Measurement of the ultrasonic properties of vascular tissues and blood from 35-65 MHz. *Ultrasound in Medicine & Biology,* 17**,** 653-66.

LOFSTEDT, R., BARBER, B. P. & PUTTERMAN, S. J. 1993. Toward a hydrodynamic theory of sonoluminescence. *Physics of Fluids A: Fluid Dynamics,* 5**,** 2911-2928.

LUKACS, M., JIANLMA, Y., GUOFENG, P., GARCIA, R. C., CHERIN, E., WILLIAMS, R., MEHI, J. & FOSTER, F. S. 2006. Performance and Characterization of New Micromachined High-Frequency Linear Arrays. *Ultrasonics, Ferroelectrics and Frequency Control, IEEE Transactions on,* 53**,** 1719-1729.

MARMOTTANT, P., MEER, S. V. D., EMMER, M., VERSLUIS, M., JONG, N. D., HILGENFELDT, S. & LOHSE, D. 2005. A model for large amplitude oscillations of coated bubbles accounting for buckling and rupture *Journal of the Acoustical Society of America,* 118**,** 7.

MASON T J, LORIMER J P & BATES D M 1992. Quantifying sonochemistry: Casting some light on a [`]black art'. *Ultrasonics,* 30**,** 40-42.

MASOTTI, L., BIAGI, E., BRESCHI, L. & VANNACCI, E. 2007. Study and Characterization of Subharmonic Emissions by Using Shaped Ultrasonic Driving Pulse. *In:* ANDRÉ, M. P., AKIYAMA, I., ANDRE, M., ARNOLD, W., BAMBER, J., BUROV, V., CHUBACHI, N., ERIKSON, K., ERMERT, H., FINK, M., GAN, W. S., GRANZ, B., GREENLEAF, J., HU, J., JONES, J. P., KHURI-YAKUB, P., LAUGIER, P., LEE, H., LEES, S., LEVIN, V. M., MAEV, R., MASOTTI, L., NOWICKI, A., O'BRIEN, W., PRASAD, M., RAFTER, P., ROUSEFF, D., THIJSSEN, J., TITTMANN, B., TORTOLI, P., STEEN, A., WAAG, R. & WELLS, P. (eds.) *Acoustical Imaging.* Springer Netherlands.

MAUSE, S. F. & WEBER, C. 2009. Intrusion Through the Fragile Back Door: Immature Plaque Microvessels as Entry Portals for Leukocytes and Erythrocytes in Atherosclerosis. *J Am Coll Cardiol,* 53**,** 1528-1531.

MEDWIN H 1977. Counting bubbles acoustically: a review. *Ultrasonics,* 15**,** 7-13.

MOFFETT, M. B., WESTERVELT, P. J. & BEYER, R. T. 1971. Large-Amplitude Pulse Propagation---A Transient Effect. II. *The Journal of the Acoustical Society of America,* 49**,** 339-343.

MORGAN, K. E., ALLEN, J. S., DAYTON, P. A., CHOMAS, J. E., KLIBAOV, A. L. & FERRARA, K. W. 2000. Experimental and theoretical evaluation of microbubble behavior: effect of transmitted phase and bubble size. *IEEE transactions on ultrasonics, ferroelectrics, and frequency control,* 47**,** 1494-509.

NEEDLES, A., ARDITI, M., ROGNIN, N. G., MEHI, J., COULTHARD, T., BILAN-TRACEY, C., GAUD, E., FRINKING, P., HIRSON, D. & FOSTER, F. S. 2010. Nonlinear contrast imaging with an array-based micro-ultrasound system. *Ultrasound in medicine & biology,* 36**,** 2097-106.

NEPPIRAS E 1980. Acoustic cavitation. *Phys. Rep.,* 61**,** 159.

NJEH, C. F., BOIVIN, C. M., GOUGH, A., HANS, D., SRIVASTAV, S. K., BULMER, N., DEVLIN, J. & EMERY, P. 1999. Evaluation of finger ultrasound in the assessment of bone status with application of rheumatoid arthritis. *Osteoporosis international : a journal established as result of cooperation between the European Foundation for Osteoporosis and the National Osteoporosis Foundation of the USA,* 9**,** 82-90.

OPHIR, J. & PARKER, K. J. 1989. Contrast agents in diagnostic ultrasound. *Ultrasound in medicine & biology,* 15**,** 319-33.

OVERVELDE M, GARBIN V, DOLLET B, DE JONG N, LOHSE D & VERSLUIS, M. 2008. Nonlinear shell dynamics near the resonance frequency of ultrasound contrast agents. *IEEE Ultrasonics Symposium.*

OVERVELDE, M., GARBIN, V., SIJL, J., DOLLET, B., DE JONG, N., LOHSE, D. & VERSLUIS, M. 2010. Nonlinear shell behavior of phospholipid-coated microbubbles. *Ultrasound in medicine & biology,* 36**,** 2080-92.

PACE, N. G., COWLEY, A. & CAMPBELL, A. M. 1997. Short pulse acoustic excitation of microbubbles. *The Journal of the Acoustical Society of America,* 102**,** 1474-1479.

PARLITZ, U., ENGLISCH, V., SCHEFFCZYK, C. & LAUTERBORN, W. 1990. Bifurcation structure of bubble oscillators. *The Journal of the Acoustical Society of America,* 88**,** 1061-1077.

PHILLIPS, P. J. Contrast pulse sequences (CPS): imaging nonlinear microbubbles. Ultrasonics Symposium, 2001 IEEE, 2001 2001. 1739-1745 vol.2.

PLESSET M & PROSPERETTI A 1977. Bubble dynamics and cavitation. *Annu. Rev. Fluid Mech.,* 9**,** 145.

QUAIA, E. 2007. Microbubble ultrasound contrast agents: an update. *European radiology,* 17**,** 1995-2008.

RATAIN, M. J. & GLASSMAN, R. H. 2007. Biomarkers in phase I oncology trials: signal, noise, or expensive distraction? *Clinical cancer research : an official journal of the American Association for Cancer Research,* 13**,** 6545-8.

RITMAN, E. L. & LERMAN, A. 2007. The dynamic vasa vasorum. *Cardiovascular research,* 75**,** 649-58.

RITTER, T. A., SHROUT, T. R., TUTWILER, R. & SHUNG, K. K. 2002. A 30-MHz piezo-composite ultrasound array for medical imaging applications. *Ultrasonics, Ferroelectrics and Frequency Control, IEEE Transactions on,* 49**,** 217-230.

SARKAR K, S. W. T., CHATTERJEE D & F, F. 2005. Characterization of ultrasound contrast microbubbles using in vitro experiments and viscous and viscoelastic interface models for encapsulation. *J. Acoust. Soc. Am.,* 107**,** 539.

SASS, W., BRAUNLICH, M., DREYER, H. P., MATURA, E., FOLBERTH, W., PREISMEYER, H. G. & SEIFERT, J. 1991. The mechanisms of stone disintegration by shock waves. *Ultrasound in medicine & biology,* 17**,** 239-43.

SCHAAR, J. A., MULLER, J. E., FALK, E., VIRMANI, R., FUSTER, V., SERRUYS, P. W., COLOMBO, A., STEFANADIS, C., WARD CASSCELLS, S., MORENO, P. R., MASERI, A. & VAN DER STEEN, A. F. 2004. Terminology for high-risk and vulnerable coronary artery plaques. Report of a meeting on the vulnerable plaque, June 17 and 18, 2003, Santorini, Greece. *European heart journal,* 25**,** 1077-82.

SHAH, F., BALAN, P., WEINBERG, M., REDDY, V., NEEMS, R., FEINSTEIN, M., DAINAUSKAS, J., MEYER, P., GOLDIN, M. & FEINSTEIN, S. B. 2007. Contrast-enhanced ultrasound imaging of atherosclerotic carotid plaque neovascularization: a new surrogate marker of atherosclerosis? *Vascular medicine,* 12**,** 291-7.

SHALHOUB, J., OWEN, D. R., GAUTHIER, T., MONACO, C., LEEN, E. L. & DAVIES, A. H. 2010. The use of contrast enhanced ultrasound in carotid arterial disease. *European journal of vascular and endovascular surgery : the official journal of the European Society for Vascular Surgery,* 39**,** 381-7.

SHANKAR, P. M., KRISHNA, P. D. & NEWHOUSE, V. L. 1999. Subharmonic backscattering from ultrasound contrast agents. *The Journal of the Acoustical Society of America,* 106**,** 2104-10.

SHI W T, F. F. & B, G. B. 1997. Subharmonic imaging with gas-filled microbubbles. *J. Acoust. Soc. Am.,* 101**,** 3139.

SHI W T, F. F., RAICHLEN J, NEEDLEMAN L & B, G. B. 1999. Pressure dependence of subharmonic signals from contrast microbubbles. *Ultrasound Med. Bio.,* 25**,** 275.

SHI, W. T. & FORSBERG, F. 2000. Ultrasonic characterization of the nonlinear properties of contrast microbubbles. *Ultrasound in medicine & biology,* 26**,** 93-104.

SHI, W. T., HOFF, L. & FORSBERG, F. Subharmonic performance of contrast microbubbles: an experimental and numerical investigation. Ultrasonics Symposium, 2002. Proceedings. 2002 IEEE, 8-11 Oct. 2002 2002. 1957-1960 vol.2.

SHUNG, K. K. 2006. Diagnostic Ultrasound: Imaging and Blood Flow Measurements *CRC Press. Boca Raton, FL 33487-2742*.

SIJL, J., DOLLET, B., OVERVELDE, M., GARBIN, V., ROZENDAL, T., DE JONG, N., LOHSE, D. & VERSLUIS, M. 2010. Subharmonic behavior of phospholipid-coated ultrasound contrast agent microbubbles. *The Journal of the Acoustical Society of America,* 128**,** 3239-52.

SILVERT W 2000. Modelling as a discipline. *Int J General Systems, pages 1–22.* .

SIMPSON, D. H., CHIN, C. T. & BURNS, P. N. 1999. Pulse inversion Doppler: a new method for detecting nonlinear echoes from microbubble contrast agents. *IEEE transactions on ultrasonics, ferroelectrics, and frequency control,* 46**,** 372-82.

SLUIMER, J. C. & DAEMEN, M. J. 2009. Novel concepts in atherogenesis: angiogenesis and hypoxia in atherosclerosis. *The Journal of pathology,* 218**,** 7-29.

STAUB, D., PATEL, M. B., TIBREWALA, A., LUDDEN, D., JOHNSON, M., ESPINOSA, P., COLL, B., JAEGER, K. A. & FEINSTEIN, S. B. 2010. Vasa vasorum and plaque neovascularization on contrast-enhanced carotid ultrasound imaging correlates with cardiovascular disease and past cardiovascular events. *Stroke; a journal of cerebral circulation,* 41**,** 41-7.

STRAUER, B. E. & KORNOWSKI, R. 2003. Stem cell therapy in perspective. *Circulation,* 107**,** 929-34.

STRELITZKI, R., NICHOLSON, P. H. & PAECH, V. 1998. A model for ultrasonic scattering in cancellous bone based on velocity fluctuations in a binary mixture. *Physiological measurement,* 19**,** 189-96.

STRIDE, E. 2008. The influence of surface adsorption on microbubble dynamics. *Philosophical transactions. Series A, Mathematical, physical, and engineering sciences,* 366**,** 2103-15.

SZABO T L 2004. Diagnostic ultrasound imaging: inside out. . *Elsevier Science, Boston.*

TEIRLINCK, C. J., BEZEMER, R. A., KOLLMANN, C., LUBBERS, J., HOSKINS, P. R., RAMNARINE, K. V., FISH, P., FREDELDT, K. E. & SCHAARSCHMIDT, U. G. 1998. Development of an example flow test object and comparison of five of these test objects, constructed in various laboratories. *Ultrasonics,* 36**,** 653-60.

THOMPSON JMT & STEWART HB 2002. Nonlinear Dynamics and Chaos. *New Jersey: John Wiley, 2002*.

TINKER, A. V., BOUSSIOUTAS, A. & BOWTELL, D. D. 2006. The challenges of gene expression microarrays for the study of human cancer. *Cancer cell,* 9**,** 333-9.

TJOTTA, J. N. & TJOTTA, S. 1980. An analytical model for the nearfield of a baffled piston transducer. *The Journal of the Acoustical Society of America,* 68**,** 334-339.

TRANQUART, F., GRENIER, N., EDER, V. & POURCELOT, L. 1999. Clinical use of ultrasound tissue harmonic imaging. *Ultrasound in medicine & biology,* 25**,** 889-894.

TSIGLIFIS, K. & PELEKASIS, N. A. 2008. Nonlinear radial oscillations of encapsulated microbubbles subject to ultrasound: the effect of membrane constitutive law. *The Journal of the Acoustical Society of America,* 123**,** 4059-70.

VAN DER MEER, S. M., DOLLET, B., VOORMOLEN, M. M., CHIN, C. T., BOUAKAZ, A., DE JONG, N., VERSLUIS, M. & LOHSE, D. 2007. Microbubble spectroscopy of ultrasound contrast agents. *The Journal of the Acoustical Society of America,* 121**,** 648-56.

VICENZINI, E., GIANNONI, M. F., PUCCINELLI, F., RICCIARDI, M. C., ALTIERI, M., DI PIERO, V., GOSSETTI, B., VALENTINI, F. B. & LENZI, G. L. 2007. Detection of carotid adventitial vasa vasorum and plaque vascularization with ultrasound cadence contrast pulse sequencing technique and echo-contrast agent. *Stroke; a journal of cerebral circulation,* 38**,** 2841-3.

VIRMANI, R., KOLODGIE, F. D., BURKE, A. P., FARB, A. & SCHWARTZ, S. M. 2000. Lessons from sudden coronary death: a comprehensive morphological classification scheme for atherosclerotic lesions. *Arteriosclerosis, thrombosis, and vascular biology,* 20**,** 1262-75.

VOS, H. J., GOERTZ, D. E. & DE JONG, N. 2010. Self-demodulation of high-frequency ultrasound. *The Journal of the Acoustical Society of America,* 127**,** 1208-17.

WARD, B., BAKER, A. C. & HUMPHREY, V. F. 1997. Nonlinear propagation applied to the improvement of resolution in diagnostic medical ultrasound. *The Journal of the Acoustical Society of America,* 101**,** 143-54.

WEAR, K. A. 2005. The dependencies of phase velocity and dispersion on trabecular thickness and spacing in trabecular bone-mimicking phantoms. *The Journal of the Acoustical Society of America,* 118**,** 1186-92.

XIONG, L., DENG, Y. B., ZHU, Y., LIU, Y. N. & BI, X. J. 2009. Correlation of carotid plaque neovascularization detected by using contrast-enhanced US with clinical symptoms. *Radiology,* 251**,** 583-9.

YANAGISAWA, K., MORIYASU, F., MIYAHARA, T., YUKI, M. & IIJIMA, H. 2007. Phagocytosis of ultrasound contrast agent microbubbles by Kupffer cells. *Ultrasound in medicine & biology,* 33**,** 318-25.

ZABOLOTSKAYA E A & KHOKHLOV R V 1969. Quasi-plane waves in the nonlinear acoustics of confined beams. *Sov. Phys. Acoust.,* 15**,** 35-40.

ZAMIR, M. & SILVER, M. D. 1985. Vasculature in the walls of human coronary arteries. *Archives of pathology & laboratory medicine,* 109**,** 659-62.

ZHANG, D., XI, X., ZHANG, Z., GONG, X., CHEN, G. & WU, J. 2009. A dual-frequency excitation technique for enhancing the sub-harmonic emission from encapsulated microbubbles. *Physics in medicine and biology,* 54**,** 4257-72.

ZHENG, H., MUKDADI, O., KIM, H., HERTZBERG, J. R. & SHANDAS, R. 2005. Advantages in using multifrequency excitation of contrast microbubbles for enhancing echo particle image velocimetry techniques: Initial numerical studies using rectangular and triangular waves. *Ultrasound in Medicine & Biology,* 31**,** 99-108.